Imaging Elastographic Contrast in Optical Coherence Tomography for Applications in Dermatology and Oncology

Alex Grimwood

Davy Faraday Research Laboratory
The Royal Institution of Great Britain
&
Department of Physics & Astronomy
UCL

Supervisors:

Prof. Q. A. Pankhurst
Director of Research, DFRL

J. Holmes
CEO, Michelson Diagnostics Ltd.

Thesis submitted for the degree of
Doctor of Philosophy (Ph.D.)
January 22, 2012

I, Alex Grimwood confirm that the work presented in this thesis is my own. Where information has been derived from other sources, I confirm that this has been indicated in the thesis.

signed:

To my loving and patient family, past and present.

Acknowledgements

Thanks to Quentin and Jon, my PhD supervisors, for giving me this opportunity. A huge debt of gratitude to Jeff Bamber for getting me out of a tight spot and to Pete Tomlins for giving me a running start. Also to Leo, you're a great soundboard, cheers.

Alastair (look, I spelt your name right!), Hemant, Matt S. and Matt W., thank you for the innumerable coffees and company. There are few greater comforts in moments of adversity than having good friends and you are they.

The same can be said for Mar and Alex, who went their separate ways a little sooner than the rest of us, but were missed and never forgotten.

Finally, to the people I love, especially Gen for having to experience second hand all the ups and downs a PhD brings. Well done! And to my mum and brother, without whom I would be lost.

Abstract

Skin cancer diagnosis often requires invasive biopsies. These can be time-consuming and cause discomfort to the patient. Optical coherence tomography is a non-invasive tool capable of imaging skin on the micron scale. However, the modality's contrast sensitivity limits its ability to distinguish between healthy and diseased tissue in some non-melanoma skin cancers. In this thesis, optical coherence elastography is explored as a means of contrast enhancement through the analysis of a sample's mechanical, rather than optical, properties.

An analysis of OCT imaging performance is used to design a suitable elastography phantom. Experimental measurements are also used to optimise the image tracking software. A well-defined, controlled actuation is applied to a tissue phantom and imaged using optical coherence elastography. A stiff inclusion is subsequently discerned from the surrounding material, even though conventional image contrast is low. Elastographic detail is also depicted in tissue. Finally, enhancements in axial displacement sensitivity are acquired through the acquisition of phase data and alternative actuation techniques are explored.

The optical coherence elastography technique was sensitive to a Young's modulus ratio of 7 from a 56 μm actuation. The possibility of detecting smaller changes in mechanical properties was also investigated. Axial phase displacement sensitivity was 50 nm, with an order of magnitude increase in strain sensitivity. This demonstrates the technique's potential usefulness in discriminating between cancerous and healthy tissues.

Contents

Chapter 1

Introduction

1.1 Overview

The PhD project was an EPSRC industrial CASE studentship conducted in partnership between UCL and Michelson Diagnostics Ltd. (MDL), manufacturer of the imaging systems used for this research. The goal was to investigate a potential method of aiding diagnosis and therapy of skin cancer in a clinical dermatology environment using optical coherence elastography (OCE). Optical coherence tomography (OCT), a non-invasive imaging modality, is combined with elastography to enhance contrast between tissues that might otherwise be difficult to distinguish. Commercial motivation stems from MDL's drive to enhance diagnostic potential in the clinical setting, whilst capitalising on OCT's non-invasive and fast image acquisition capabilities.

A thorough characterisation of OCT system performance and elastographic image processing was undertaken, followed by controlled, repeatable elastographic experiments. Finally, research addressing improvements and variations of the method were investigated. The OCE technique demonstrated here produces a well-defined actuation in a magnetisable implant using an external magnet. This enabled full characterisation of the forces, strains and deformations experienced by the specimen. These results provide a strong grounding for future research into the mechanical properties of skin cancers and their imaging using elastographic techniques.

1.1.1 Thesis Structure

- **Chapter 1** is an introduction, detailing the scope and ambition of the research. Context is provided through general descriptions of: skin cancer; diagnostic techniques and therapies and the justification behind the elastographic technique developed in this thesis. A broad technical background is provided for the principles of elastography and OCT.

- **Chapter 2** focuses on the MDL OCT system and forms an appraisal of its imaging performance. Specific attention is given to measuring its spatial resolution and contrast characteristics. Both influence imaging and elastographic sensitivity. The work associated with this chapter was conducted during a secondment with the National Physical Laboratory (NPL). Additional research into phantom development for the project was directly applicable to constructing elastography experiments later on in the thesis.

- **Chapter 3** is an appraisal of the image tracking technique used to form elastograms from OCT data. Image properties affecting tracking performance are characterised. Tracking performance is optimised using data and techniques discussed in this chapter. Imaging artefacts in the tracking data are identified and mitigation procedures described. Elastogram construction from displacement data is also detailed.

- **Chapter 4** implements the image tracking technique detailed in Chapter 3 to derive elastographic contrast from phantoms and tissue using the remote magnetic actuation method. Results and performance are discussed.

- **Chapter 5** is an investigation into the use of phase measurements from the OCT system's complex signal as a means for improving elastographic sensitivity. The potential of dynamic measurements is also explored.

- **Chapter 6** summarises the experimental work conducted within the thesis. Further work and the potential of elastography in dermatology are discussed.

1.2 Introduction

Michelson Diagnostics Ltd. (MDL) produces a micron resolution clinical imaging system with a pixel size of 4 μm, and an enhanced imaging depth of $2mm$ in air. The company's ambition is to deploy OCT as a time-saving alternative to histopathology, with the advantage over conventional biopsy methods that it can sample multiple sites quickly and non-invasively [1, 2]. Under an EPSRC Industrial CASE Grant, The Davy Faraday Research Laboratory (DFRL) investigated how to help MDL achieve this goal using OCE.

Previous studies of skin imaging using OCT have shown promise, with the modality being used to identify tumour thickness in basal cell carcinoma (BCC) and propagation below the skin's surface, as well as to track tissue response during therapeutic interventions such as laser ablation and topical treatments [3, 4, 5]. Comparative studies have also been made between histopathology and OCT images [6]. As a result of these initial results, a number of clinical studies are currently underway to assess the modality's usefulness in enhancing microscopic skin surgery (Mohs surgery) and cancer detection [7, 8].

1.2.1 Elastographic Contrast Enhancement

As a modality, OCT generates high resolution, video-rate images over a region approximately 1.5 mm deep in skin and up to 1 cm across. This is useful for detecting small, millimetre-scale lesions. However, previous literature has criticised OCT's poor contrast sensitivity, lack of depth penetration and resolution when compared to histopathology slides imaged via conventional microscopy [9, 10, 11]. The development of optical coherence microscopy (OCM) systems has given rise to systems with a resolution closer to a typical light microscope, however these systems are not easily adapted to patient imaging [12]. MDL has addressed the latter two issues by using multi-channel OCT to enhance the depth penetration and lateral resolution of their systems relative to other OCT products [13].

MDL are now investigating contrast enhancement in OCT to help distinguish skin cancers from healthy tissue, specifically using elastographic methods. Elastography was deemed promising, because the technique is easily combined with MDL imaging systems. Moreover, it is a widely-published cancer research and diagnostic tool [14] and a number of commercial systems now incorporate an elastography imaging mode. Other contrast enhancement techniques have been described in OCT. These include the topical application of clearing agents (such as glycerol), nanoparticle contrast agents, the use of speckle reduction techniques and adjunct imaging methods such as: birefringence, spectroscopic and Doppler imaging [15, 16, 17].

Elastography's suitability within dermatology is still being established. Researchers at Hitachi Medical Systems have demonstrated initial results where malignancy is associated with elastographic features for a range of non-melanoma skin cancers (NMSCs) in high frequency ultrasound [18]. Furthermore, a clinical study is presently being conducted [19]. The intended application of OCE techniques investigated in this thesis would be on early diagnosis of small neoplasms and tumours, especially in BCC and other cancers which are sometimes hard to identify in OCT images. The specific elastographic response of NMSCs remains a subject for investigation. Visual observations and histopathology indicate their structural dissimilarity to surrounding tissue and this variation is associated with changes in mechanical properties between diseased and healthy tissue in other cancers.

1.3 Skin Cancer

1.3.1 The Importance of Cancer Diagnosis

Since the "War on Cancer" declared by U.S. President Nixon along with the allocation of \$100 million and the passing of the National Cancer Act in 1971, global investment in treatment and understanding of the diseases collectively known as cancer have shown a huge increase. Even so, the best efforts of scientists and policymakers have failed to reduce the number of cases recorded each year. In fact the World Health Organisation projects a 45% increase in cancer deaths between 2007 and 2030, or an estimated 12 million deaths worldwide [20]. In England, figures suggest one third of all people will develop cancer, which equated to an annual cost of £4.35 billion to the NHS in 2006/07 alone [21]. Cancer is increasingly common in modern ageing populations as the risk from communicable diseases has declined, and this shifting pattern places it as the number two killer in developed nations - second only to cardiovascular disease [22]. Yet despite these grim statistics, diagnosis, therapy, and palliative care are more effective four decades on than they were in Nixon's time. Cancer research now spans disciplines across the scientific community, spurred on by lucrative investment and political will. In this environment, M-OCE has an opportunity to contribute both to treatment and research. OCT is a relatively new imaging modality, and people are currently working towards emergent applications which could see next generation systems complement or even challenge today's gold standards [23, 24, 25]. This PhD project is a small part of that drive to bring OCT into mainstream use.

1.3.2 Cancer Formation and Metastasis

One of the most commonly overlooked aspects of cancer is the fact that it is not a single disease, but rather a classification given to a category of illnesses. Cancer is caused when cells in the body are no longer regulated by the usual homeostatic mechanisms - such as controlled cell death (apoptosis). They may form immortal/clone cell lines, and tumours which compete with conventional cells [26]. This type of growth is a form of neoplasia, and is only classified as cancer when there are signs of malignancy. Usually cancer is the result of damage to DNA, which leads to mutation, often via exogenous factors like viral infection, or over-exposure to radiation, or specific chemicals in food and the environment. However, cancer may have endogenous causes such as inherited genetic mutations, the action of free radicals, chronic inflammation, and prolonged hormone imbalances [27]. No matter what the underlying cause, cancer formation (carcinogenesis) will only occur when a number of mechanisms fail within the cell, propelling it out of its regular life-cycle. Carcinogenesis is a multi-stage process, which can lead to cancer *in-situ*, as well as the invasion of surrounding tissue, and potential metastases [28, 29, 27]. The scale of malignancy is defined by how developed each of these stages is. Metastases occur when the primary cancer sheds cells, spreading the disease to other organs of the body. This occurs only if the primary cancer has stimulated angiogenesis and invaded surrounding tissue. The migratory cells can be motile, forming pseudopodia, and may travel in response to external stimuli. Usually they disseminate in an embolism via the lymphatic system or circulatory vasculature, affecting major organs such as the brain, lungs, and bone. Current techniques struggle to identify if a primary cancer will metastasise, and the size of the emboli make screening difficult until the metastasis has become established as a secondary tumour. [30, 31]

1.3.3 Staging

Staging describes the anatomic extent of a patient's cancer based on specific criteria. The most common staging device is the TNM system, which classifies the size of the untreated primary cancer (T), the extent of regional lymph node involvement (N), and the presence of distant metastases (M). A number is then assigned to each letter, which reflects the severity of that aspect of the disease. Usually a clinical prognosis is formed from examining a patient before surgery, and is classified as cTNM. Any further information gained from surgically removed tissues is used to form a pathologic classification, or pTNM. This staging device can guide the clinician's prognosis and choice of adjuvant therapy; but it acts only as a complement to cTNM results. For most cancers, the TNM system leads to them being assigned one of five overall stages (I, II, III, IV, or V), indicating the overall severity and spread of the disease. The criteria for TNM grading and final staging of the cancer will vary depending on its location and type, but should always relate to its natural progression; however, some types of cancer cannot be classified using this system including: cancers of the brain, female reproductive system, and spinal cord, along with lymphoma and leukaemia[32, 33, 34, 35].

1.3.4 Skin Cancer

The skin incorporates a wide variety of cell types and skin cancers are defined according to their assumed cell of origin. The three most common forms of skin cancer are: melanoma, squamous cell carcinoma (SCC) and basal cell carcinoma (BCC).

Melanoma

Melanoma is usually identified using the ABCDE criteria (asymmetry, border irregularity, colour variegation, diameter and evolving) and often identified as a pigmented tumour, with only 2% being amelanotic. A definitive diagnosis is only possible with excision and histology. Tumours can penetrate up to 4 mm into the skin and a large margin between 1cm – 3cm is required for definitive treatmet. OCT is not considered to be an effective clinical diagnostic tool here where comparatively large (cm-size) margins are required and tumour penetration depth exceeds the system's imaging depth.

Nonmelanoma Skin Cancers

Unlike malignant melanomas, nonmelanoma skin cancers (NMSC) are often removed without a final diagnosis [36]. As a result, published incidence rates are likely to be under-represented. A 2007 study proposed about 1 in 5 seventy year olds had NMSC at some point; stating a total figure of 13 million white non-Hispanics in the USA compared with official NHIS estimates of only 5 million [37].

BCC

BCC is the most common form of skin cancer in people from temperate climates and white ethnic background, accounting for 80% of NMSCs [38]. An increase in incidence rates is associated with exposure to UV radiation. Risk factors tend to be an individual's susceptibility to burn and prior genetic disposition, as well as the presence of atypical nevi.

Superficial and early nodular BCCs are situated close to the skin surface and are within the imaging depth of OCT, making it potentially useful as a diagnostic aid for early detection. Biopsy is sometimes required to distinguish superficial BCC from other pathologies (such as actinic keratosis or Bowen's disease).

Treatments include surgery, phototherapy and topical applications and radiotherapy [38]. The use of OCT with Mohs surgery may improve treatment efficiency. Furthermore the protracted nature of other therapies means OCT imaging could offer an opportunity to non-invasively monitor disease progression.

SCC

SCC, the second most common skin cancer, is directly related to prolonged exposure to sun (or UV radiation), combined with risk factors, such as fair skin, burn susceptibility and photodamage. Multiple localised foci, ulcers, plaques and keratoses are commonly seen. Suspect lesions are often observed over extended periods for signs of nodular growth, which then require biopsy [39]. Standard excision with a wide margin or Mohs surgery for more cosmetically sensitive areas such as the face are treatment options. Treatments such as cryotherapy may also be performed on lesions < 6 mm.

Pre-cancerous Lesions

Three main categories of pre-cancerous lesions exist: actinic keratosis (AK), Bowen's disease (BD) and lentigo maligna. The first two are precursors to SCC. Actinic keratosis originates from the basement membrane of the epidermis and has a texture distinct from healthy tissue [38]. Invasiveness or fully developed SCC is categorised where the affected area appears below the basement membrane. However, this may require a biopsy.

1.3.5 OCE for Skin Cancer

Specific applications for OCE can be envisioned despite the preliminary nature of the technique. For example, biopsies are taken to distinguish between AK, BD and superficial BD. OCE might, in future, be capable of providing such a distinction non-invasively. Malignancy in pre-cancerous lesions must also be ascertained and, again, OCE might have potential in imaging the extent to which the basal membrane has been compromised. Disease progression over a treatment course such as cryotherapy or phototherapy may be imageable with OCE. Finally, OCE may aid in identification of tumour margins during Mohs surgery .

1.4 Optical Coherence Tomography

OCT is a low coherence interferometry technique that produces an intensity profile relating a specimen's structure along a single axial scan (A-scan). By combining a series of laterally-spaced A-scans, an OCT system can be used to construct a full 2D image (B-scan). Often, a series of laterally-spaced B-scans is used to form a 3D image volume of the specimen. Figure 1.1 is a representation of a typical OCT imaging scheme.

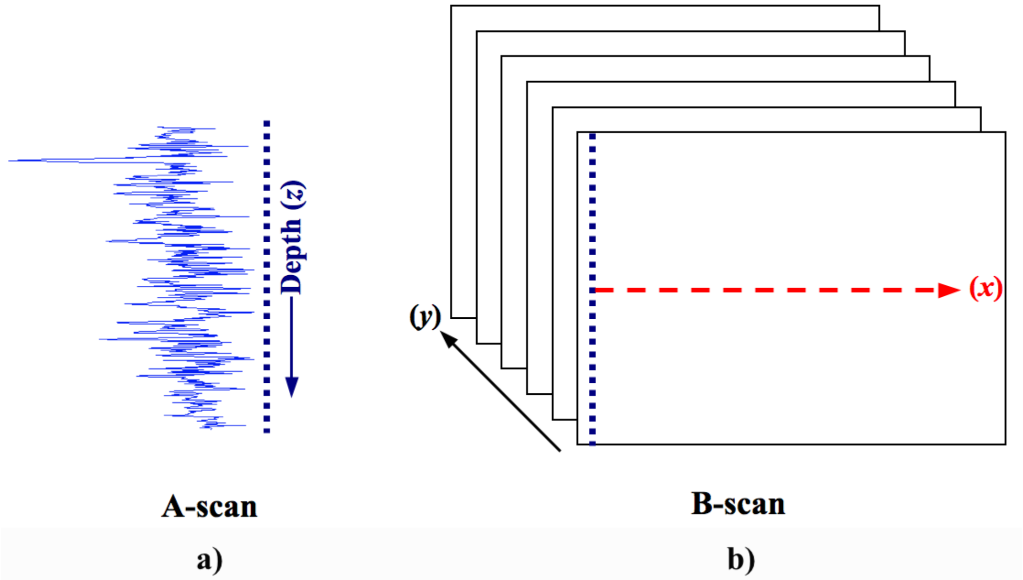

Figure 1.1: A Typical OCT imaging sequence, showing the intensity profile of a single A-scan in a), where depth is represented by the z-axis (blue dotted line). The formation of a 2D image (B-scan) from multiple, laterally spaced A-lines is shown in b), where the red dashed x-axis denotes this lateral dimension. By acquiring a series of B-scans along the z-axis, a 3D image volume is constructed.

1.4.1 Swept Source OCT (SS-OCT)

Each A-scan is produced from the interference signal at a photodetector between light backscattered off a sample with that sent along a reference arm. In the case of MDL OCT systems, the light is provided by a narrow band tunable laser source. Here, an interference profile is formed by sequentially measuring the intensity of interference at a number of wavelengths (figure 1.2). The photodetector current can be expressed as [40]:

$$I(t) = \frac{\eta q}{hv}\left(P_r + P_0\int r^2(z)dz + 2\sqrt{P_r P_0}\int r(z)\Gamma(z)cos\left(2k(t)z + \phi(z)\right)dz\right) \quad (1.1)$$

where η is the detector sensitivity, $q = 1.6 \times 10^{-19}$ C, hv is photon energy, P_r is optical power over the detector's entire surface from the reference arm, P_0 optical power to the sample, z axial position from zero optical path length, $r(z)$ the sample's reflectance profile and ϕ its phase, $\Gamma(z)$ is the source coherence function and $k(t)$ the wavenumber, which relates source wavelength at time t ($k(t) = 2\pi/\lambda(t)$). This interference signal is digitised and undergoes a discrete Fourier transform (DFT), its resulting magnitude being the depth-encoded A-line.

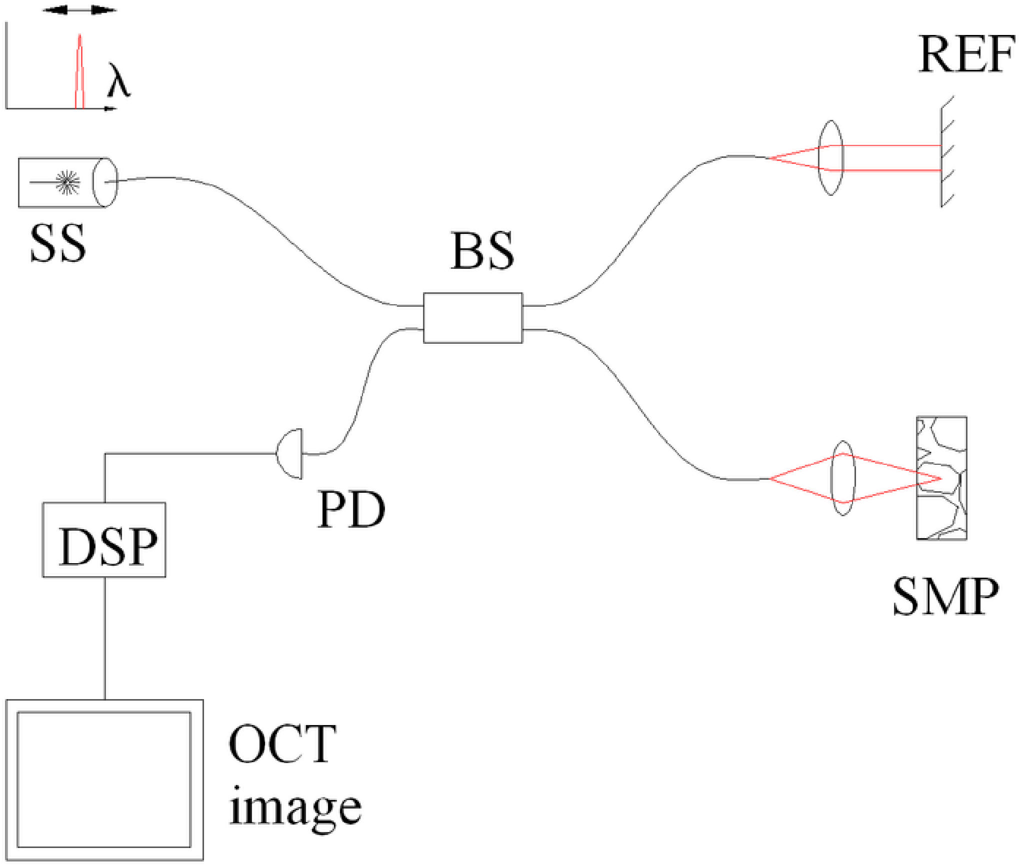

Figure 1.2: Schematic of a typical SS-OCT system, where SS is the tunable source, BS the beamsplitter, REF & SMP are the reference and sample arms of the interferometer respectively, PD is the photodetector and DSP the digital signal processor. Image sourced from Wikipedia [41].

When imaging scattering media, a speckle pattern is produced in the B-scans. The speckle characteristics are a function of the system's optics (numerical aperture and coherence length) and are also sensitive to the scattering properties of the sample. This sensitivity to sample structure provides contrast in OCT images. These aspects of OCT imaging are described in greater detail in Chapters 2 & 3.

1.4.2 Michelson Diagnostics Ltd. OCT Systems

Two systems are currently manufactured by MDL, the EX1301 bench-top model and VivoSight hand held platform. both utilise the same fundamental technologies and were used in conjunction with the same software suite throughout the PhD. As such, they can ostensibly be thought of as interchangeable within the context of this thesis. However, there are practical differences between the two. For example: the sample beam exits from a hand-portable probe on the VivoSight, making it more versatile, but less stable (a custom mounting was thus used to anchor the probe for experimental purposes). Both models incorporate a 1350 nm swept source with a 150 nm bandwidth. Light is sampled at discrete wavelengths over the laser's bandwidth, the timings of which are linearised produce a stable interferogram across the entire source spectrum. Known distortion features associated with swept source OCT systems like MDL's include periodic lateral motion between B-scans of a few pixels. This arises when the scanning mirror responsible for sweeping the imaging beam over an imaged object is not completely synchronised with the image acquisition timings. Additionally, imaging a highly reflective surface can result in signal saturation at the detector, leading to complex conjugate ambiguity (creating image echoes of the surface) [42].

Michelson's approach to OCT is underpinned by a technology that enhances lateral resolution through combining the signal from four tightly focused beams. By staggering the depth of field from each beam, their signals can be combined into a composite image. This image exhibits a higher lateral resolution (obtained by focusing each channel over a small region) for a comparable depth of field obtained using a single beam (figure 1.3). This is achieved by splitting a single source beam via a rattle plate. Each of these four virtual sources then travels along its own separate channel through the interferometer. At the sample arm, each channel is aligned along the imaging plane and proceeds one after the other as the group is swept across the sample. Staggering the foci is made possible by physically offsetting the ends of each channel's fibre optic, so that the objective lens focuses each beam differently. It is then possible to extract the in-focus portion from each channel and stitch them together into a single image. The technique requires the four channels to have the same path lengths, originate from a single source and scan the same region of the imaged sample. In some images composite images, discontinuities at the boundary between channels is observable as a result of differences between each channel's focal depth and variation in the relative intensities of light travelling from the source through a particular channel.

Some post-processing is made possible through MDL's proprietary software and still more was undertaken by accessing the raw files output when an image is acquired. The software is capable of applying speckle smoothing and channel blending effects. It can also combine a number of adjacent A-scans into a single, averaged A-line to further reduce speckle noise. These settings were not used during experiments unless otherwise stated because it was found that they could interfere with the image tracking process. Access to the raw data files facilitated the extraction and reconstruction of image data from individual channels, which further enhanced the image tracking process and enabled sampling of phase information (as demonstrated in Chapters 3, 4 and 5).

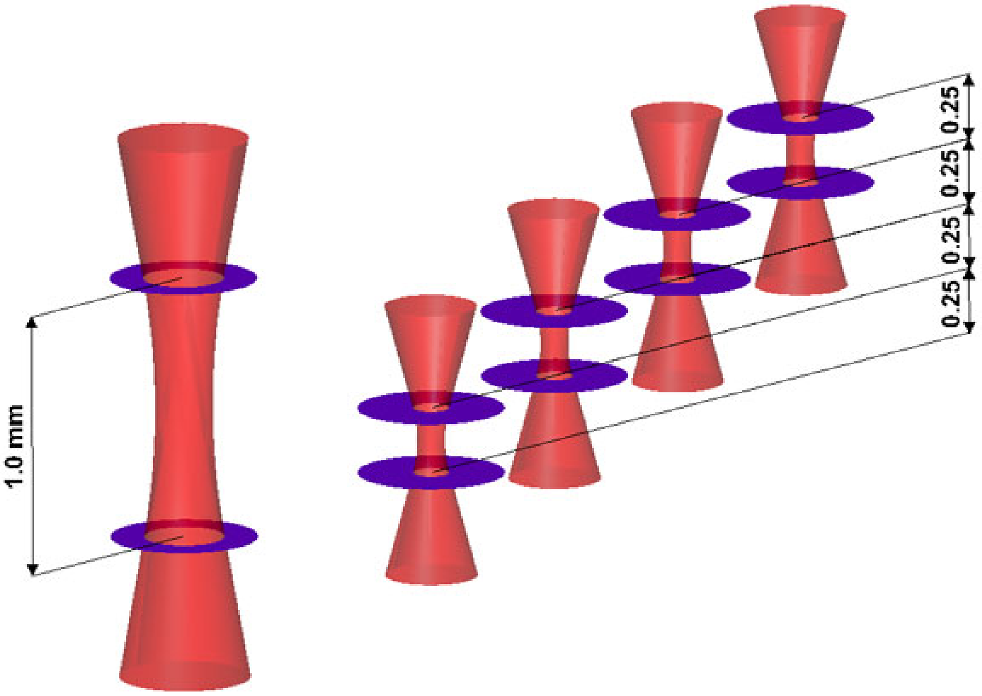

Figure 1.3: Illustration displaying the depth of field of a single beam over a comparable depth of field obtained using four channels in the staggered focus configuration.

1.4.3 Other Competing Methodologies

A number of competing methodologies exist within OCT. Most notably time domain OCT (TD-OCT) and Fourier domain OCT (FD-OCT). Both FD-OCT and SS-OCT are capable of higher imaging sensitivities and frame rates compared to TD-OCT [43]. However, FD-OCT and SS-OCT are also prone to imaging artefacts as a result of relying on Fourier domain image processing [44].

For in vivo applications, such as patient imaging, OCT must demonstrate advantages over high frequency ultrasound (HFUS). HFUS cannot attain the same levels of lateral spatial resolution as OCT, but is capable of imaging larger regions [45]. Furthermore, ultrasound imaging requires a good acoustic interface between probe and tissue, whereas OCT is a non-contact modality.

Other diagnostic modalities such as confocal microscopy and histopathology directly compete with OCT in dermatology. Here, SS-OCT cannot compete on contrast sensitivity and the sub-micron spatial resolution of confocal microscopy. However, its relative strength lies in not having to remove tissue prior to imaging. This is necessary for the other modalities because their penetration depth is limited and exogenous contrast agents are also required. In OCT, little sample preparation is needed. As a result, OCT is comparably efficient, quick and painless.

Photoacoustic imaging is an experimental modality currently under development with poorer resolution than OCT, but improved depth penetration. It is capable of producing endogenous contrast in tissue, enabling the imaging of blood microvasculature and other structures, including melanoma [46]. However, it is not as mature technologically as OCT and its performance within a clinical dermatology setting remains undefined.

1.5 Elastography

Elastography is a method of deriving information about the mechanical properties of a sample, such as Young's modulus, Poisson's ratio, viscoelasticity or strain resulting from an applied stress. Strain estimation is a common technique, often facilitated by tissue displacement tracking algorithms. These have become established practice within the ultrasound community, and are the most prevalent methods used for measuring displacement and particle velocity, which is then used to estimate strain [47, 48, 49, 50, 51].

The underlying principles governing tissue displacement include an assumption of tissue as a continuum, where linear momentum is conserved and force, acceleration and deformation are incorporated [14]:

$$\frac{d}{dt}\int\int_{V}\int \rho\dot{\mathbf{u}}\mathbf{dV} = \int_{\mathbf{S}}\int \mathbf{T^{(n)}}\mathbf{dS} + \int\int_{\mathbf{V}}\int \rho\mathbf{b}\mathbf{dV} \tag{1.2}$$

Here, the rate of change in momentum is equal to the forces experienced by the designated volume. In the above equation, ρ is density, $\dot{\mathbf{u}}$ is the displacement vector in time (velocity), $\mathbf{b}$ is the force vector per unit mass and $\mathbf{T^{(n)}}$ is the traction vector (equivalent to stress) at the surface S of volume V.

Providing all strains are small, the infinitesimal strain tensor applies, where all strain components, ε_{ij}, are represented as:

$$\varepsilon_{ij} = \frac{1}{2}\left(\frac{\partial u_i}{\partial x_j} + \frac{\partial u_j}{\partial x_i}\right) \tag{1.3}$$

The stress strain relation for a linear elastic solid can thus be expressed as [14]:

$$\sigma_{ij} = (2\mu\varepsilon_{ij} + \lambda\varepsilon_{kk}\delta_{ij}) = \frac{E}{(1+v)}\left(\varepsilon_{ij} + \frac{v}{1-2v}\varepsilon_{kk}\delta_{ij}\right) \tag{1.4}$$

where λ and μ are Lamé constants, μ also being shear modulus, E is Young's modulus, v is Poisson's ratio and δ_{ij} is the Kronecker delta (valued at 0 unless $i = j$, when it is equal to 1).

1.6 Thesis Goals

Broadly, the goal of this PhD was to investigate OCT contrast enhancement in dermatology (specifically regarding skin cancer) through the application of elastography. Particular emphasis was placed on assessing the potential of magnetic actuation as a method of generating a contrast signal. Further primary goals were to assess OCT system performance, set out how the contrast enhancement techniques developed could improve it and what costs may be incurred to other performance parameters. A secondary goal was to minimise any degradation in system performance, whilst also developing further the elastographic techniques explored. It was also necessary to address potential commercial prospects of the OCE techniques and manage research objectives accordingly. However, emphasis was placed on fulfilling goals related to fundamental system characterisation and initial demonstration of the OCE technique, because such a body of work would best inform any future development and potential commercialisation.

Chapter 2

OCT System Characterisation

This chapter is a summary of work carried out with the Biophotonics Group at NPL during 2008 whilst on secondment there. The aim was to develop an understanding of OCT system performance (related specifically to the Michelson Diagnostics EX1301). This provided a foundation upon which further contrast enhancement techniques were developed. The author's work concentrated on the initial development and measurement of system characterisation phantoms, focusing on system spatial resolution and contrast. The two attributes are relevant to this thesis, as they influence the parameters of displacement tracking techniques described in later chapters. Furthermore, the fabrication techniques acquired at NPL were adapted to produce elastography phantoms with controllable, consistent mechanical and optical properties. This was essential to the elastography experiment in Chapter 4.

The author's contribution to the project specifically comprised: Research and selection of suitable phantom materials (including both scatterer and bulk), formulation and optimisation of the manufacturing process and production of an array of custom phantoms covering a range of scatter coefficients (μ_s), which incorporated bi-layer specimens. Further contributions included the production point spread function phantoms, initial research into machining techniques and finally, OCT image measurements of both bi-layer contrast phantoms and the initial point spread function phantoms. Image post-processing, deconvolution and all work regarding sensitivity phantoms were conducted by other group members, including Pete Tomlins and Peter Woolliams, as well as Christian Hart and Matthew Tedaldi.

Research into the fabrication and measurement of system resolution was the predominant activity, resulting in a demonstration of point spread function deconvolution. Previous methods for measuring system resolution and deconvolution methods have been described, but not implemented with a standardised and robust test phantom [52, 53, 54]. This chapter extends such work by detailing the fabrication of an OCT calibration phantom specifically designed to be compatible with a range of systems and its use to measure changes in 2D Point spread function (PSF) across an imaged region. Finally, the deconvolution method has also shown notional improvements to resolution in both lateral and axial dimensions.

The culmination of the Biophotonics Group's research is described below. It was their aim to produce gold standard test objects for OCT system characterisation and work towards system imaging performance enhancement [55]. Progress from this initial research was still being made at the time of writing by further quantifying the OCT signal attenuation profile as a means to extract diagnostically useful information [56]. Additionally, other research groups have corroborated the PSF measurement results and offered descriptions of an alternative calibration phantom. Descriptions of how PSF changes with system source bandwidth and compares with the edge spread function have now also been published [57].

2.1 Introduction

In OCT some performance attributes are easily discerned and often provided by manufacturers – such as A-line acquisition rates and imaging area dimensions. However, no industry standard has been developed. As a result, manufacturers tend to quote their own defined performance figures, hindering the consumer's ability to relate and compare systems. Additionally, figures on some imaging characteristics appear to be lacking across the board (such as signal to noise ratio and contrast).

Imaging performance for modalities such as OCT, ultrasound, MRI and CT is often measured with respect to three specific attributes: contrast, sensitivity and resolution. The ability to measure these from a set of predefined test objects enables the user to directly relate an individual system's performance to known physical properties. This allows comparisons to be made between different systems and their relative performance. The current lack of standardisation among OCT manufacturers is indicated by the table in Appendix A, which compares performance figures quoted by manufacturers.

Testing regimes may also be conducted on a system over the course of its working life for quality assessment and control. Furthermore, the adoption of a standardised testing apparatus enhances the reproducibility of all results regardless of manufacturer, configuration or user variability.

This standardisation proves useful in the context of the thesis as it attempts to set bench-mark figures by which any new imaging technique can be compared. This is particularly true for system resolution, because elastographic techniques such as cross-correlation, create displacement and strain maps with a reduced spatial resolution compared to the original OCT images. Contrast is also a key metric for elastography, because it must be able to clearly show useful information not easily distinguished in standard images. The implication for an elastographic contrast technique is that an elastogram is only useful when the contrast between structural elements is greater than that in the original OCT image. This is demonstrated in Chapter 4, where a stiff inclusion is identified via elastograms despite being almost indistinguishable from its surroundings in standard OCT scans.

First, the concepts of contrast and sensitivity are briefly introduced and the Biophotonics Group's research on developing test phantoms for measuring these attributes is outlined. Resolution is explored in greater detail, reflecting the proportion of work conducted. The manufacturing process and implementation of a resolution phantom is also described. It was used to measure the point-spread function across the imaging region of a Michelson Diagnostics EX1301 system. This information was then used to apply a position-dependent deconvolution function, which produced an apparent improvement in image resolution.

2.2 Contrast

The two imaging attributes of contrast and sensitivity were researched independently by group members. For my contribution to the following section, I was involved with the design, fabrication and initial imaging of contrast phantoms, which shared much in common with the resolution test objects.

Experimental measurements of the OCT A-line signal through a contrast test object are presented and compared with two theoretical models: a relatively simple light attenuation model, and a modified Radiative Transfer Equation model. A simulation of the light attenuation model is used to highlight differences between it and the experimental data.

2.2.1 Introduction

OCT contrast performance can be determined by the difference in image signal intensity between two distinct regions. If the contrast sensitivity of a system is high, then a detectable change in signal intensity will be apparent between two regions with only marginally different light-scattering properties. A contrast phantom was made by fabricating an object with two such regions and comparing signal intensities.

With a range of phantoms in which the two regions vary by different amounts, it is possible to investigate the entire contrast range of a system.

Owing to the speckle nature of OCT images, an average signal intensity for a given area is usually recorded. The image intensity is dictated by factors, such as refractive index change at an object's surface (the air-surface interface), the concentration and physical properties of scatterers within the imaged sample, and the imaging depth at which an intensity measurement is taken. For example, an idealised OCT system produces a detector photocurrent signal profile, i_{det} [25].

$$i_{det} = \frac{\eta e}{h\bar{v}} \sqrt{P_r} \cdot \sqrt{P_s} \tag{2.1}$$

where η is the CCD's quantum efficiency, e is electronic charge, h Planck's constant, $\bar{v}$ mean optical frequency of the incident radiation, P_r light power in the reference arm and P_s light power in the sample arm.

For a uniform material, in which scatterers produce a fully developed speckle pattern, this system results in an image depth signal intensity I which can loosely be described by the exponential decay of the transmission signal through an object [58]:

$$I(z) = I_0 \exp\{-2\mu_s z\} \tag{2.2}$$

such that μ_S is scattering coefficient, I_0 is the intensity at the phantom surface and absorption is negligible such that the coefficient of absorption (μ_a) does not contribute to attenuation.

Variations in scattering coefficient μ_s will result in changes to the signal intensity, providing a means for making the first, basic contrast measurements. For example, an object comprising two layers with distinct values, μ_{s1} and μ_{s2}, will exhibit an Intensity profile $I(z_{tot})$ which changes suddenly at the layer boundary. The intensity can be expressed as:

$$I(z_{tot}) = I_0 \exp\{-2(\mu_{s1} z_1 + \mu_{s2} z_2)\} \tag{2.3}$$

By constructing a series of double-layer test objects with decreasing $\Delta\mu_s$, it is possible to derive a ratio of the log attenuation profile for the two layers.

Although the simple light attenuation model's prediction of signal behaviour is accurate at shallow imaging depths, it inadequately accounts for contributions to the OCT signal from other factors such as: multiple scatters, backscatter at refractive index discontinuities, and diffusion processes at greater depths [59, 60]. Other numerical methods describing the depth-dependent OCT signal in terms of light propagation exist [61, 62, 63] and the Radiative Transfer Equation (RTE) for small angles is one such example [64, 65]. The model is usually applied to an homogenous medium comprising randomly distributed scatterers with a known scattering coefficient μ_s, negligible absorption coefficient μ_a, and anisotropy factor g (the mean cosine of scattering angle). However, the introduction of a stratified geometry where each layer has its own individual properties cannot be adequately addressed without modification. Turchin [59] describes an enhanced version of the RTE, which also incorporates the incident beam's dimensions and depth of focus. It has been applied to the inverse problem of determining the optical properties of layered samples from OCT images. A solution to the standard problem, where all initial parameters are known, is still mathematically complex even for two layers when compared to the simple attenuation approximation. Appendix B summarises the mathematical derivation described by Turchin. Its solution for a stratified object with two differently scattering layers requires four parameters per layer: μ_s, probability of backscatter p_b, variance of the scattering phase function $\langle\gamma^2\rangle$, as well as the layer boundary position.

To experimentally verify the RTE method would have required further characterisation of these properties in the contrast test objects, which was not possible owing to time constraints. However, a comparison can still be made between the simple attenuation model and experimentally measured OCT signal. This highlights specific features in the data which are only adequately accounted for in the RTE model.

2.2.2 Method

Bi-layer phantoms produced a step-change in μ_s from one layer to the next. A series of phantoms was produced in which the change $\Delta\mu_s$ became gradually less pronounced. By measuring the change in the OCT signal, it was notionally possible to characterise the system's contrast performance. However, owing to time constraints, it was only possible to obtain experimental measurements from a single test object. This was a result of the difficulties in fabricating uniform phantoms with consistently sized layers hundreds of microns thick.

The phantom design consisted of Araldite DBF epoxy resin and HY951 hardener (Aeropia Resins, UK) containing concentrations of mono-disperse glass microspheres (Whitehouse Scientific Inc, USA), as can be seen in figure 2.1. Challenges arose, such as how to create a uniform distribution of scatterers, how to remove air bubbles from the resin, how to prepare the resin's surface so that a clean interface and imaging plane could be established.

Figure 2.1: A series of phantoms with increasing scatterer concentrations (from left to right)

The fabrication procedure finally established was to use monodisperse particles of 2 μm. These were added to the resin before stirring and sonicating for two hours (typical concentrations would be around 0.5 mg per 100 g DBF). The mixture was left to cool for twenty minutes before stirring in the HY951, because heat generated from mixing would accelerate the curing process and lead to an uneven set. Then the resin was cast into moulds, which were placed in a degasser, where pressure was slowly reduced to 0.15 bar below atmospheric. This was maintained for about twenty minutes before gradual recompression, after which the moulds were left to set in an oven at 80 °C for eight hours. Having allowed the phantoms to cure, the imaging surface was polished smooth. Next, the phantom was placed back into its original mould and another layer cast on top of the first. Other than using a different scatterer concentration, the upper layer was manufactured in much the same way.

Challenges emerged including air escaping from the mould into the resin and control over layer thicknesses. To address these issues, reusable silicone moulds were employed. The volume of epoxy used for each layer was measured precisely and its dimensions after polishing recorded, so that base layers could be manufactured consistently. Polishing produced a smooth interface between layers and a uniformly flat surface. When casting the top layer, a silicone rubber collar was applied atop the base surface to prevent the liquid epoxy running off into the gap between the base layer's edge and mould wall. After curing, the collar was removed and the top layer polished down to a thickness of only 900 μm.

Once complete, a B-scan of the phantom was recorded. The phantom was tilted at a 5° angle to reduce signal saturation at the phantom's surface. The OCT A-line signal was then averaged to produce an intensity-depth profile. The signal gradient through both layers was estimated and qualitatively compared with theoretical models.

2.2.3 Results and Discussion

A plot of OCT signal intensity through a notional bi-layer phantom complying to the simple exponential light attenuation model was produced (figure 2.2). The signal profile $ln(I(z_{tot}))$ was calculated for three phantoms, where μ_s varied for the base layers. From these results it can be shown that:

$$\frac{\partial}{\partial z} \ln(I(z_{tot})) \propto \mu_{sn} \tag{2.4}$$

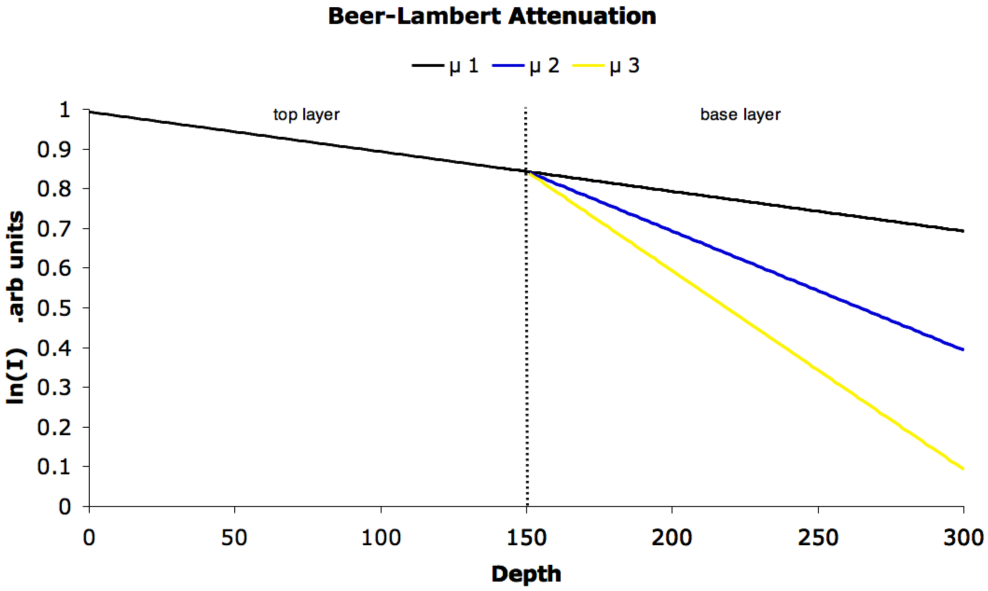

Figure 2.2: OCT signal through a bi-layer phantom according to the simple exponential attenuation model, with signal intensity and depth in arbitrary units. The coefficients are: $\mu_1 = 0.5 \times 10^{-3}$, $\mu_2 = 1.5 \times 10^{-3}$, $\mu_3 = 2.5 \times 10^{-3}$. Their respective gradients are: 1×10^{-3}, 3×10^{-3}, 5×10^{-3}.

This gradient change concurs with experimental observations from an actual bi-layer phantom. However, there are additional features that demand a more detailed explanation. The averaged A-line OCT signal from a B-scan through the phantom can be seen in figure 2.3. Apart from the surface reflection artefact (a well-known feature caused by complex conjugate ambiguity from the Fourier transformed OCT signal) significant peaks are present at both this surface and also at the layer interface [42]. Additionally, there is a step change in signal at the layer interface that is linked to an increase in signal intensity through this layer - despite its higher scattering coefficient μ_s. Such an increase in signal contradicts the simple exponential attenuation model and is apparently counter-intuitive.

The RTE model described by Turchin does account for a step-change increase at the layer boundary, although it requires prior knowledge of the boundary location. It is based upon the assumption of tissue as a layered, randomly scattering media, defined by the probability of back-scatter with depth, total scattering coefficient and variance of small-angle scattering phase function. [59]. These physical mechanisms, most notably back scatter, contribute to a sample's bulk refractive index [66]. Such a discontinuity in refractive index would result in increased reflections at the surface and layer boundary, thus generating a strong OCT signal. The RTE model employs a genetic algorithm to fit these parameters to an experimentally obtained OCT signal from a bi-layered sample similar to the contrast phantoms studied here.

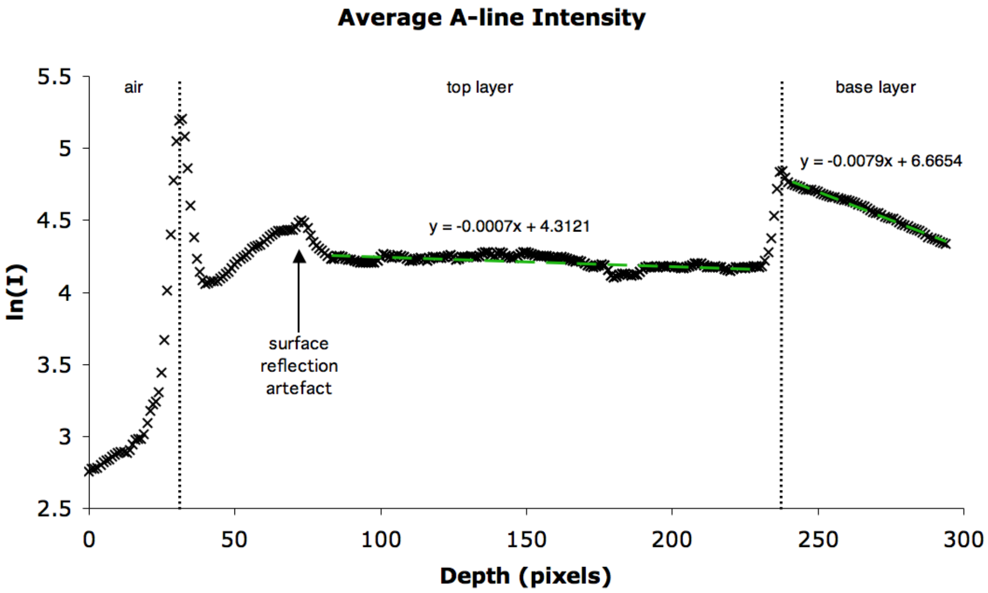

Figure 2.3: Average A-line signal through a bi-layer phantom as measured experimentally from an OCT B-scan. The base layer had a higher scattering coefficient, corresponding to the increased rate of signal attenuation. The signal peaks and step changes are unaccounted for in the simple attenuation model.

2.3 Sensitivity

Research into sensitivity was conducted primarily by Peter Woolliams. A description of the basic theory is described here, illustrated by an initial design concept for a sensitivity phantom. However, no experimental results were acquired over the course of my secondment.

The sensitivity phantom was markedly different from the contrast test object. Instead of producing a uniformly scattering medium, the goal was to manufacture a clear medium containing a row of parallel lines. The refractive index mismatch between the medium and lines decreases consecutively along the row. By imaging across the row, so that the lines were orthogonal to the imaging plane, a B-scan containing a series of gradually fading dots was produced. The OCT system's relative sensitivity could thus be measured by counting the number of distinguishable points. Laser-etching was used to produce the lines through a clear resin and a sample B-scan can be seen in figure 2.4.

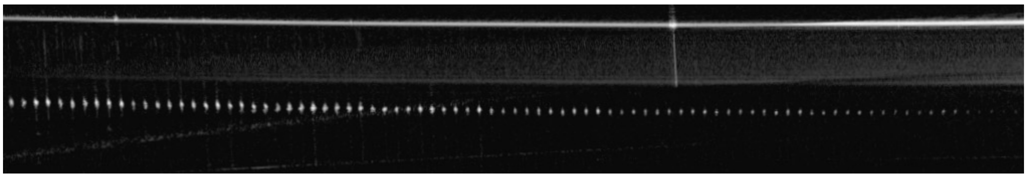

Figure 2.4: OCT B-scan of the NPL sensitivity phantom.

2.3.1 Theory

A system's sensitivity is characterised by the signal to noise ratio (SNR), where the signal is generated by a known source. Calculating an individual OCT system's SNR is relatively straightforward (as can be seen in equation 2.5 if a number of measurements have been made, namely: the detector's responsivity ρ, the imaged sample's reflectivity R_s, The system's source spectral density S_{src} and its noise equivalent bandwidth B [44]. However, measuring every attribute may not be possible for each system, or the values may not be made available by the manufacturer.

$$SNR = \frac{\rho R_s S_{src}}{4eB} \tag{2.5}$$

Instead, sensitivity can be experimentally quantified by measuring image SNR from scans of a test object like the one described. In this instance there are only two variables and these are easily measured from image data. Measurements are made of the standard deviation in background signal σ_{bg} and average peak signal $\bar{I_{pk}}$ generated by each of the row elements. The ratio is a measure of SNR at that element, which can be compared with values across the row and from other systems.

$$SNR = \frac{\bar{I_{pk}}}{\sigma_{bg}} \tag{2.6}$$

2.4 Resolution

The main goal during my secondment to NPL was to develop a resolution test object. The object comprised low density concentrations of particles small enough to act as point scatterers, enabling measurements of the point spread function (PSF) throughout the OCT imaging volume. This section recounts the fabrication process and its refinements, as well as measurements taken (primarily by Pete Tomlins and Peter Woolliams) to characterise the EX1301 system's resolution. A potential application for improving its performance was also demonstrated by applying a PSF deconvolution to standard B-scans, increasing spatial resolution. The phantom's requirement was met, additionally its use enabled development towards image enhancement. Although the latter is not directly relevant to the thesis, deconvolution could be used in future to enhance contrast between tissue structures in dermatological imaging and to improve the performance of digital image tracking.

The research undertaken on this particular project culminated in a peer-reviewed paper and in depth technical report published by NPL [55, 67], the content of which is summarised below. As is the case with the other two test objects, the resolution phantom's primary design goal was to make cross platform comparisons, allowing the relative strengths of different systems to be gauged. However, the results also enabled me to better define parameters associated with correlation-based image tracking (Chapter 3), such as reference kernel size. Additionally, it provided a spatial limit below which, sub-resolution tracking techniques would be required.

2.4.1 Introduction

The resolution of an OCT system is dictated by separate optical mechanisms governing its axial and lateral components. Even though the underlying processes differ, both components are characterised in the same way through analysing image signal PSF from an effective point source. In the axial dimension, coherence length of the optical source dictates the resolution limit [68], whilst the lateral dimension is limited by diffraction. Further limitations are imposed when imaging through turbid media, such as tissue. Here, a fully developed speckle pattern often emerges where speckle size is determined by the system optics [69], this in turn influences the effective resolution. Evaluation of a baseline system PSF is conducted in a low-scatter regime, so that a fundamental measure of resolution can be obtained. By applying a deconvolution to the measured PSF, further resolution enhancements can be obtained. In future, deconvolution may be used as a quantitative imaging technique [55].

Deconvolution methods have already been described for OCT as a means of improving depth resolution [70, 71]. Although deconvolution of the 2D PSF has been explored previously, its variation with respect to depth and lateral position was not taken into account [52]. These was addressed using measurements from a PSF test object notionally similar to the contrast phantom previously described in this chapter, with the exception of a much lower scatterer concentration. A different epoxy resin was chosen for its improved curing properties and scatterers with a higher reflectivity were also employed.

2.4.2 Theory

Axial and Lateral Resolution

For an OCT system with a source spectral intensity $S(\omega)$, and a uniform 100% reflective mirror in the reference arm; the OCT signal may be represented as the integral of the product of the source spectrum $\xi(x)$ (such that $\xi_r(x) = \xi_s(x) = \xi(x)$)and object function $\Pi(\omega, x - x_0)$, where x is the lateral position of the sample beam offset from the sample's centre (x_0) as seen in equation 2.7 [67].

$$I(\omega) \approx 2S(\omega)\Re\left[\int_{-\infty}^{\infty} \Pi(\omega, x - x_0)\xi(x)^2 dx\right] \tag{2.7}$$

Multiplication of two functions in the frequency domain (as above) is equivalent to convolving the functions in the time domain. Thus, for a single A-scan, this leads to a convolution of the spectral profile and object function, which can be represented as:

$$\Pi(\omega, x_0) = \sum_{j=1}^{N} r(x_0)_j \exp\left[i\phi(x_0)_j\right] \tag{2.8}$$

where ϕ represents the phase, which in turn dictates optical thickness τ (via $\phi_j = \omega\tau_j$)of an imaged object for a specific position j along N sample points [72]. The reflectivity r_j gives rise to a time domain function $\bar{r}(t)$, which for a reflective sample occupying a single point ($N = 1$) generates a peak along an OCT A-line equivalent to the axial PSF. If the source spectral function is taken to be Gaussian (as one would expect from the single mode optical fibres used in OCT), the source can be expressed as in terms of its centre frequency ω_0 and its e^{-1} radius w_ω:

$$S(\omega) = S_0 \exp\left[-\frac{(\omega - \omega_0)^2}{w_\omega^2}\right] \tag{2.9}$$

For such a Gaussian source, the time-domain equivalent e^{-1} radius is w_z, which is related to the FWHM by:

$$\Delta z = 2w_z\sqrt{ln2} \tag{2.10}$$

The axial resolution Δz can then be regarded as a function of the source's coherence length [25]:

$$\Delta z = 0.44\frac{\lambda_0^2}{\Delta\lambda} \tag{2.11}$$

Although not addressed here, Δz is inversely proportional to an imaged object's refractive index [55]. However, this approximation still holds true, especially with respect to the spectral source profile. In the EX1301 a Hann filter is applied, just like a Gaussian function, the Hann is smoothly symmetric. This, combined with the single-mode optics employed, makes it acceptable to rely on a Gaussian approximation in both lateral and axial regimes. As such, Gaussian optics can be used to describe the focused imaging beam's propagation. Its e^{-1} radius w_i varies along the optical axis (z), pinching off to a beam waist at w_0 before widening out to a Rayleigh length $z_R = \pi w_0^2\lambda_0^{-1}$ (the point at which the beam width is double w_0):

$$w_i(z) = w_0\sqrt{1+\left(\frac{z-z_0}{z_R}\right)^2} \tag{2.12}$$

Conventionally, this results in a FWHM at the beam waist Δx_i of:

$$\Delta x_i = 2w_0\sqrt{ln2} \tag{2.13}$$

However, the combination of beams from the reference and sample arms results in a $2^{-0.5}$ enhancement of the detected radius [67], such that:

$$w_x = \frac{w_0}{\sqrt{2}} \tag{2.14}$$

The detected beam waist can thus be expressed in a similar fashion to equation 2.12 by substituting the w_0 term for w_x. This results in an expression for lateral resolution based on the focusing lens numerical aperture (NA):

$$\Delta x = 2w_x\sqrt{\frac{ln2}{2}} \approx 0.37\frac{\lambda}{NA} \tag{2.15}$$

In tissue, the refractive index n increases relative to air. This creates a reduction in NA without degrading lateral resolution, because diffraction effects are also suppressed in relation to n [55].

2D Point-spread Function

As explained in equation 2.7, the OCT image can be regarded as a convolution of its PSF and object function. For two dimensions the image $g(x, y)$ can be expressed similarly, where the object function is now $\Pi(x - x_0, y - y_0)$:

$$g(x, y) = \int_{-\infty}^{\infty} \Pi(x - x_0, y - y_0) h(x_0, y_0) dx_0 dy_0 \tag{2.16}$$

If the imaged object is small enough to practically resemble a point, such that it satisfies the approximation of a Dirac delta function $\Pi(x, y) = \delta(x, y)$, the image output will simply be an expression of the 2D PSF. By producing an object containing a distribution of these notional delta scatterers, the PSF can be mapped across the entire OCT imaging area.

2.4.3 Materials and Methods

PSF Phantom

The original PSF phantom was fabricated in a similar manner to that described for the contrast test object. A DBF epoxy resin block was cast which contained a low density of the same mono-disperse scatterers. However, two challenges arose from using these materials in a low scattering regime. First, imaging artefacts generated side lobes in the Fourier transform as a result of strong beam reflection at the phantom surface were clearly visible; these obscured portions of the OCT data. Second, the PSF signal intensity was comparatively weak. Reflection artefacts were kept to a minimum by polishing and angling the imaged surface , however the outer edges of the DBF phantom did not always cure properly. As a result, polishing often resulted in an uneven deformation of the imaged surface. To mitigate artefacts, produce a uniform illumination across the imaged phantom, and enhance the PSF signal, another resin was used in combination with a different variety of scatterers.

The new resin was a two-part polyurethane (DR006, Atlas Polymers, UK). During the course of fabrication it was observed to be optically clearer than the DBF, whilst also setting to a more even and complete cure. The scatterers added to this new resin were red iron oxide spherical nanoparticles (07674, Polysciences Inc., USA). The particles were not monodisperse – having a predominant diameter of 400 nm distributed between 300-800 nm. Despite this variability, they were still effectively Dirac delta scatterers with respect to the OCT system [67]. Importantly, they proved highly reflective compared to the glass microspheres previously used.

The fabrication method was similar, scatterers were added to the resin's least viscous part and sonicated whilst stirring for five minutes. After combining the two parts, the mixture was degassed at 0.15 *bar* before curing in an oven at 60 °C for 12 hours. Finally, the top surface was polished. Using the new resin enabled a flatness of <75 nm peak to valley with a local roughness of <25 nm, as measured with a surface profilometer over a 2 mm area.

The phantom mould was used to produce an object 25 mm in diameter and 15 mm tall. Scatterer concentration was calculated to produce an average particle spacing L between 25 μm and 50 μm. This was achieved by calculating the mass-volume ratio of particles (m) to resin (V) from $m/V = M/L^3$, where M is the mass of a particle and L is the target spacing.

PSF Measurements

The following measurements were conducted by the paper's main authors: Pete Tomlins and Peter Woolliams. A 3D section of the phantom was imaged by taking multiple B-scans with a 4 μm slice spacing. The resulting image cube was 8 mm wide and 3 mm deep, and background subtraction was performed to remove imaging artefacts. A location map of PSF positions was constructed by thresholding the image data to 40 % signal intensity and above. Any peak signals were set to a value of 1, whilst all other regions were zeroed. This reference map was then used to locate the individual PSF peaks in the original B-scan data, around which were placed square windows of 21×21 pixels. A 2D Gaussian function $h(x, y)$ derived from equation 2.9 was then applied, where:

$$h(x,z) = A \exp\left\{ - \left[\frac{(x-x_0)^2}{w_x^2} + \frac{(z-z_0)^2}{w_z^2} \right] \right\} \tag{2.17}$$

This allowed extraction of estimated values for Δx and Δz at each location. Steps were taken to optimise the fit parameters and discard erroneous values where contributions from multiple PSFs influenced a single measurement.

Average resolution values were then mapped to an 80×30 grid (element size 100×100 μm) across the OCT's B-scan imaging area. This produced a spatial map of resolution throughout a single B-scan.

Using the approximated PSFs for each 21×21 pixel kernel, their corresponding Gaussian functions were deconvolved. Where this was not possible, a Gaussian fit derived from mean values for Δx and Δy was employed, so that a reasonable deconvolution could be facilitated across the entire B-scan area. the Lucy-Richardson algorithm [73] was used for the deconvolution; after which, resolution values for the deconvolved image data were then recorded as before. These were compared with the previous resolution values.

2.4.4 Results

Approximately 25 × 10^3 PSFs were located within the image cube. Figure 2.5 depicts a typical B-scan analysis, with the detected PSFs clearly marked. Spatial variations in resolution are illustrated in figure 2.6 for both axial and lateral components. These appear to indicate a decrease in resolution away from the focal region. Deconvolution appeared to enhance the resolution, as seen in figure 2.7. Measurement of the beam waist from experimental data was undertaken and compared with the theoretical model. These both showed agreement with each other and were reinforced by previously published data on the EX1301 [13]. Both measured and calculated data are shown in figure 2.8 along with values for the effective deconvolved beam radius.

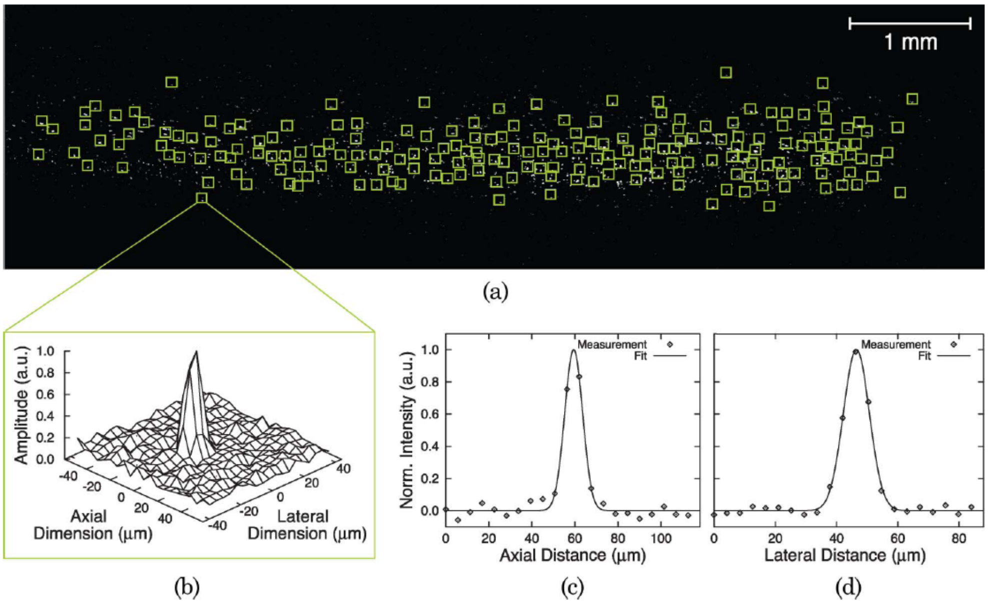

Figure 2.5: a) A single B-scan showing the located PSFs and their associated 21×21 pixel windows. The mapped surface within a single window b), and associated Gaussian fits for c) axial, and d) lateral components are also shown.

2.4.5 Discussion

Results from the published paper appear to indicate the OCT system's non-uniform sensitivity (figure 2.5). This was attributed by the Authors to the system's depth

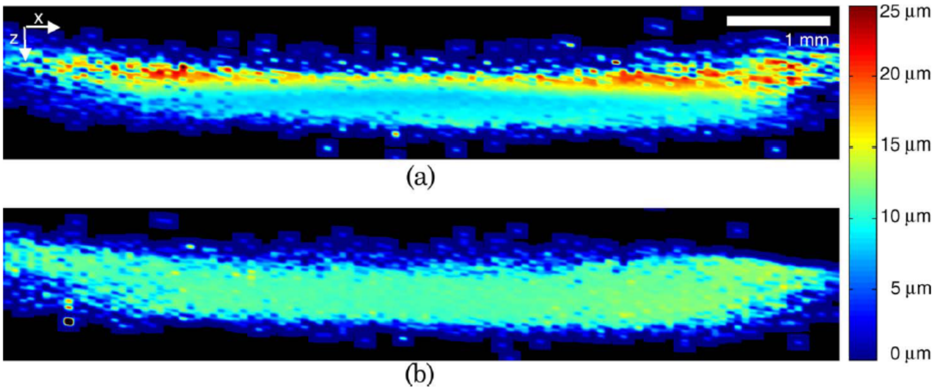

Figure 2.6: Spatial distribution across the B-scan image area of a) lateral resolution and b) axial resolution.

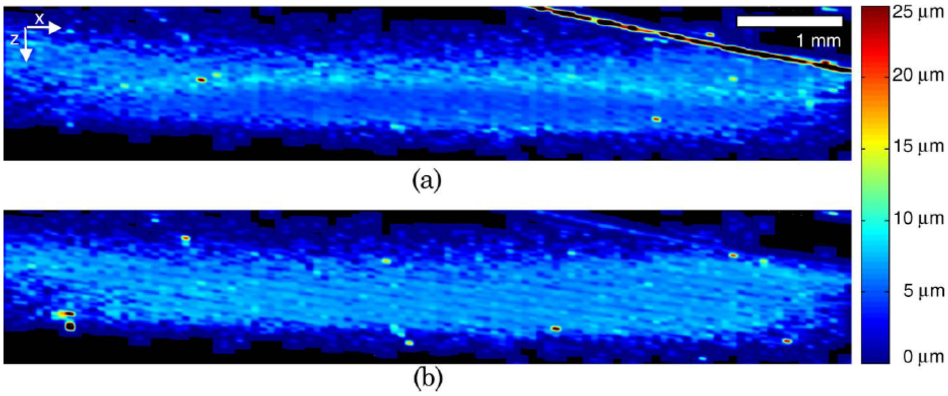

Figure 2.7: Spatial distribution after deconvolution of a) lateral resolution and b) axial resolution.

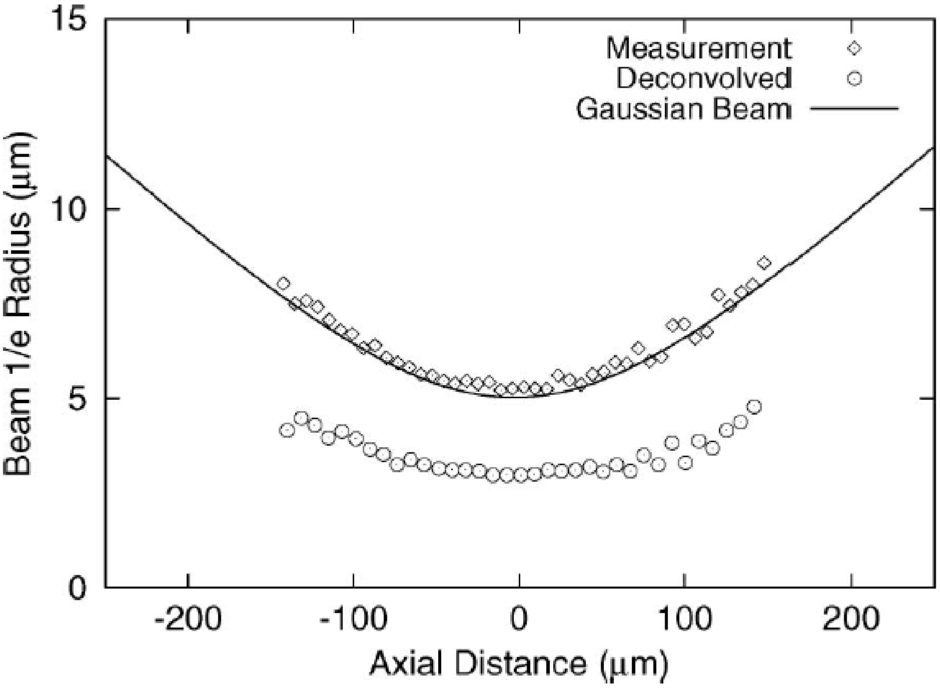

Figure 2.8: Beam waist measurements (diamonds) and theoretical values (line) for a Gaussian model where w_0 is 7.1 μm (measured using a beam profiler and λ_0 is 1310 nm. Deconvolution values are also shown (circles).

of field and (to a lesser extent) its use of Fourier domain detection. The result is a visible horizontal band of detected scatterers, which appears to fade away towards the B-scan's upper and lower edges. The implication in future chapters, when applying digital image tracking, is that displacement estimates will become decorrelated at remote distances from the system focus. Decreases in lateral sensitivity were attributed to the imaging system optics. This was in line with recommendations from the manufacturer that a loss of sensitivity might be observed along the edges of any B-scans wider than 5 mm. Such an issue must be considered when imaging low contrast features in patients.

The shape of the resolution's spatial distribution in figure 2.6 also provides an indication of how that sensitivity varies transversely and across the depth of field. The beam sweeping optics appear to create a gentle curve in the lateral resolution distribution as well as a noticeable decrease towards the B-scan's edges. The Authors suggest that this is the result of an effective increase in NA, caused by a higher beam angle relative to the focusing lens as the beam is swept across the phantom. Further investigation into phase variation has since been conducted and is discussed in Chapter 5, which suggests the curvature, at least, is the result of the depth of focus varying when the beam is laterally swept. Such aberrations could also account for the degradation in axial resolution towards the B-scan edges, which would in turn degrade image tracking sensitivity. The adaptive nature of PSF sampling across the imaged region mitigates this effect, as can be seen in figure 2.7.

Measurements of speckle statistics and their dependency on a sample's optical properties were measured indirectly via the OCT intensity signal. To further reinforce results from this chapter, comparisons of a phantom's bulk refractive index, μ_s, μ_a and scattering phase function could have been made using alternative characterisation techniques independent of OCT. Despite the fact that some of these attributes can only be measured indirectly, they would provide a means of validating assumptions such as the predominance of Mie scattering, the negligible contribution of absorption coefficient (μ_a), the Gaussian behaviour of system optics and the relationship between speckle size and scatterer size.

2.5 Conclusions & Future Work

Results from the resolution phantom study demonstrate significant non-uniformity in both axial and lateral resolutions of the Michelson Diagnostics system, expanding upon previous experimental measurements of OCT axial resolution [54]. Variations were attributed largely to changes in system optics over the lateral scanning sweep, particularly at the peripheries of wide (over 5 mm) images. This would potentially affect the performance of correlation-based image tracking techniques where the influence of noise and non-uniform resolutions can impact on displacement estimates. From the results it is apparent that image tracking will be most effective within the central 5 mm of an OCT image, close to the depth of focus. As such, in Chapter 4, where a localised actuation is applied to image a stiff inclusion, the inclusion is placed close to this zone.

A deconvolution method has been demonstrated for improving resolution in phantoms with isolated point spread scatterers. Although deconvolution techniques have been described previously, this chapter's results lead to the conclusion that any deconvolution filter reliant upon system point spread function may benefit from taking into account the fact that it varies across the imaged region [52, 53]. Furthermore, if deconvolution techniques can be applied to samples exhibiting a better developed speckle pattern (as found in tissue), improvements could be made in tracking performance by effectively reducing speckle size, whilst endogenous contrast between tissue structures may also be enhanced, improving diagnostic performance. However, accurate estimation of a tissue's local refractive index relative to the PSF phantom is required [55].

System sensitivity and image contrast were also investigated, although to a lesser extent. Further work is still needed to produce a phantom capable of objectively and quantitatively appraising system SNR, especially because the PSF results indicate how such a metric can vary with both relative axial and lateral position.

Image contrast and its relation to both imaging system parameters and tissue properties such as μ_s and μ_a were also investigated. Experimental phantoms were designed with varying μ_s so that comparisons could be made. In turn, bi-layer phantoms with a step change in scatterer concentration were also fabricated and a change in signal attenuation was attributed to the shift in scatter coefficient. However, the experimental research was not extended to a full quantitative analysis owing to the limited time spent on this project. Despite this, learning to fabricate contrast phantoms enabled the author to develop an elastography phantom suitable for characterising the image tracking techniques set out in Chapter 3.

Further research conducted by Pete Tomlins has also built upon the initial contrast phantom research, resulting in a competing method for enhancing tissue contrast, which could be applied to skin cancer detection. His team is currently developing a technique named scattering attenuation microscopy (SAM), which aims to enhance tissue structure contrast by analysing signal attenuation rates and quantitatively map this metric onto standard OCT images [56].

Chapter 3

Image Tracking and Strain Estimation Methods

3.1 Introduction

This Chapter contextualises normalised cross-correlation (NCC), the most relevant image tracking method to this thesis and the backbone of elastographic imaging in Chapter 4. Some fundamental concepts and their potential influences on image tracking are discussed, namely: speckle statistics, image signal processing and the choice of tracking parameters. The aim is to identify the best conditions for NCC tracking in terms of specimen properties, imaging system settings and tracking parameters. Furthermore, this chapter provides a response to the relative lack of background literature on NCC within the OCT community, despite its use in a number of OCT elastography publications [74, 75, 76, 51, 77]. These publications contain descriptions of practical applications and experimental measurements for NCC output, but the fundamental mechanisms affecting NCC performance and in-depth system characterisations are absent. Whilst this chapter is not an exhaustive critique on image tracking and strain estimation techniques, it is a characterisation study of the methods explored during the author's research and is thus used to thoroughly examine factors affecting tracking performance, something which the OCT literature has previously lacked

A Matlab implementation of NCC tracking from the Institute of Cancer Research (ICR) Ultrasound Imaging Group was employed extensively throughout the author's research. In this chapter factors affecting the tracker's performance, including OCT image speckle statistics, are explored. Both the degree to which a speckle pattern is developed and the underlying speckle size influence tracker output. Additionally, the type of input signal can modify any resultant displacement estimates. To find the optimum OCT input signal, a range of estimates are taken at different stages of OCT image processing. These findings are used to inform the experimental design and analyses in Chapter 4.

Artefacts in the displacement estimates are also described and presented along with experimental observations. Two mitigation techniques are advanced, these comprise applying the ICR's tracker to each of the MDL system's four channels and utilising the tracker in an iterative process, where a single image set is subjected to repeated passes.

Finally, a strain estimation method employed in concert with the ICR tracker is described. The strain estimator was first described by F. Kallel and J. Ophir [78]. It was implemented by the ICR group and subsequently adapted to image displacement estimates in Chapters 4 & 5 by the author.

3.2 Normalised Cross-correlation

The use of cross-correlation to track displacements can be traced back nearly 30 years, where it was initially employed in the detection of sample motion between A-lines [79]. Later, by applying cross-correlation to successive B-scans and interpolating the correlation peak, it was possible to estimate movement between frames on a sub-pixel scale [80]. Although interpolation methods differ, the underlying technique is still employed for this thesis.

The standard correlation coefficient, C, used to describe a linear association between two continuous variables (X & Y) is expressed as:

$$C = \frac{\sigma_{xy}}{\sigma_x \sigma_y} \tag{3.1}$$

where σ_x and σ_y are the standard deviations of X and Y respectively, whilst σ_{xy} is the covariance between the variables. In NCC, C is normalised to $-1 \leq C \leq 1$ [81].

The form of equation 3.1 employed at the core of the NCC image tracking algorithm for this thesis, is the MATLAB function *normxcorr2*. The function is a discretised equivalent, which generates a correlation coefficient, $C(u,v)$, based upon image feature vectors normalised to unit length, giving an approximate cosine form:

$$C(u,v) = \frac{\sum_{x,y}\left[f(x,y) - \bar{f}_{u,v}\right]\left[t(x-u,y-v) - \bar{t}\right]}{\left\{\sum_{x,y}\left[f(x,y) - \bar{f}_{u,v}\right]^2 \sum_{x,y}\left[t(x,y) - \bar{t}\right]^2\right\}^{0.5}} \tag{3.2}$$

where $\bar{t}$ is the mean image intensity across a chosen feature, f is the image and $\bar{f}_{u,v}$ is the mean image value under a region of interest in f [82].

A practical implementation is represented in figure 3.1, which equates to taking two images (referenced here as A & B) and finding correlations between them. For compression elastography, the images typically depict a sample before and after an increase of applied stress. A region (kernel) in image A is passed through equation 3.2. The kernel is used to represent an image feature from A, this image feature is cross-correlated at every possible position within a search window in image B. The correlation coefficient reaches a maximum value at the location within the search window most closely resembling the feature from A. The relative position of the feature from A and its estimated location in B can thus be used to estimate its displacement. By scanning the kernel (and, accordingly, the search window) across an entire image, it is possible to produce an exhaustive displacement map.

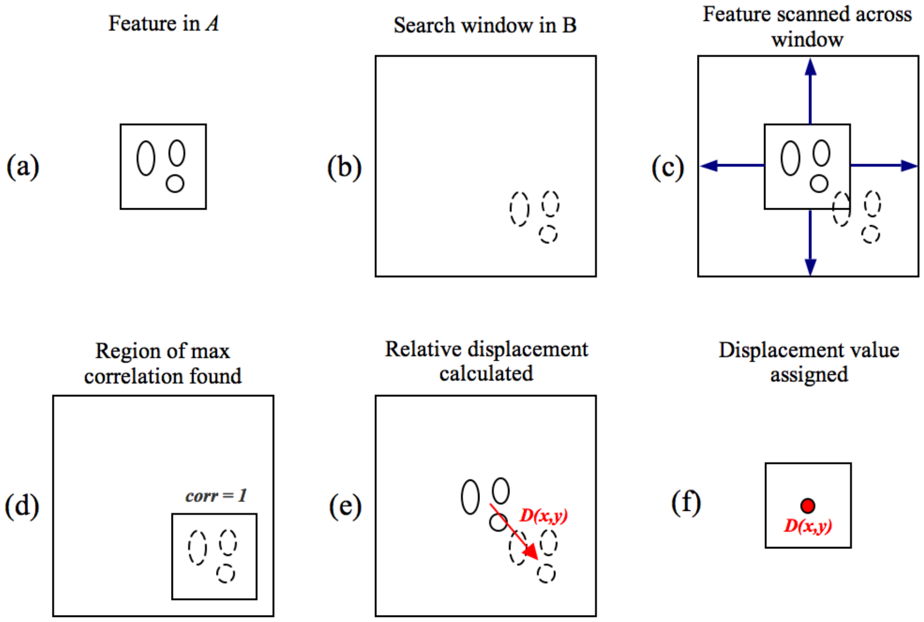

Figure 3.1: The cross-correlation process for a single kernel: (a) a square kernel is defined in image A; (b) a larger search window is defined in image B; (c) the kernel is scanned across the search window and a correlation coefficient recorded at every position; (d) a record is made for the location of maximum correlation coefficient; (e) relative displacement is calculated as the difference in position between feature and region of max correlation; (f) The kernel's central pixel in A is assigned the displacement value and then shifts along 1 pixel. The process is repeated, starting from (a) until a full displacement map is constructed for all pixels.

3.2.1 Correlation Peak Interpolation

Calculating the correlation coefficient's maximum will produce a displacement estimate accurate to the nearest whole pixel. In the context of tracking a single feature between frames, this produces an output similar that shown in figure 3.2. It is possible to improve the estimation's sensitivity by interpolating the correlation function and calculating its peak position. A second order polynomial is applied to the three data points demarcating the correlation peak and the peak location recorded. This enables sub-pixel sensitivity, as can be seen in figure 3.3.

The choice of interpolation method is a compromise between accuracy and speed of computation. In figure 3.3, the interpolated results (diamond) have a slight bias towards the original NCC results (spot), known as peak locking or jitter [83, 84]. This periodicity remains when using other interpolation schemes [80].

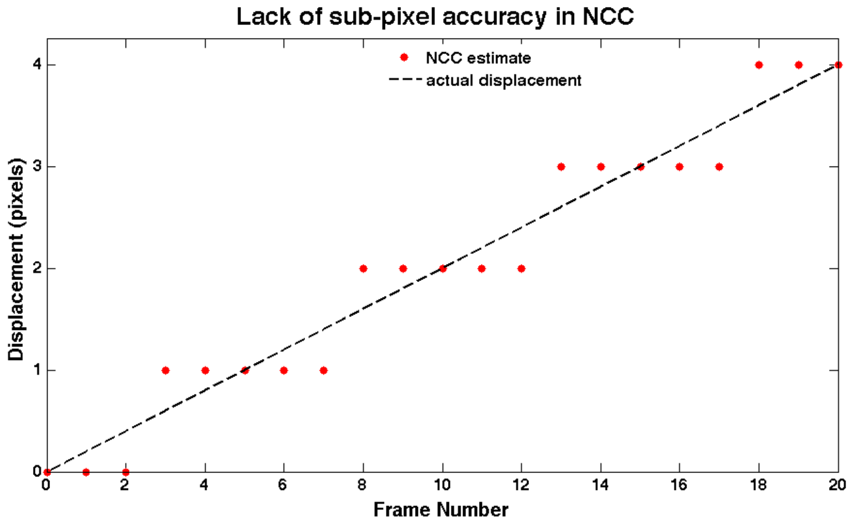

Figure 3.2: Example of displacement estimates from a normalised cross-correlation (NCC) image tracker without correlation peak interpolation. The data reflect movement of a single parabolic feature with a FWHM of 4.3 pixels.

3.2.2 Speckle and NCC Tracking

Speckle

As discussed in Chapter 2, OCT is a coherent imaging technique and so produces an image constructed from speckle intensities. The stable component of this speckle facilitates NCC tracking and characteristics of the speckle pattern will influence a tracker's displacement estimates. The appearance of speckle is also significant for OCT manufacturers, who strive to reduce its appearance via image averaging,

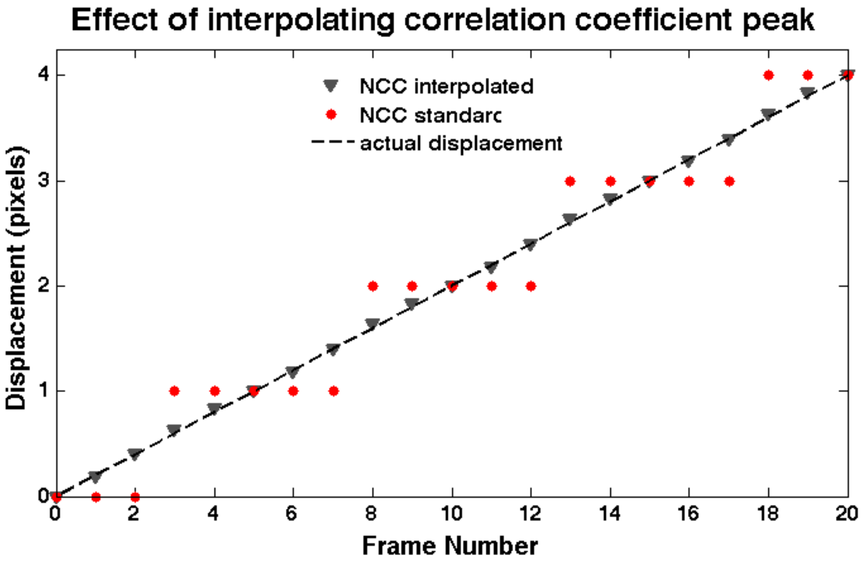

Figure 3.3: NCC estimates employing correlation coefficient peak interpolation compared with the previous non-interpolated results.

compound focusing and various other techniques [85]. However, the implication for NCC tracking is that there may be fewer features to track once these measures have been implemented, making the technique less reliable.

In this section, speckle statistics derived from standard OCT images and simulations are investigated and the effects of image processing are addressed later on in the chapter. A specimen's internal structure will have an effect on the imaged speckle pattern. Where there is a high concentration of randomly distributed sub-resolution scatterers, speckle becomes over developed and independent of an imaged object's physical structure. It depends instead upon system optics and source wavelength. However, NCC can be effective at lower scatterer concentrations where a speckle pattern is either fully developed or slightly undeveloped. Here, the intensity at any one point in the image is dictated by the summed interference of the scattered beam's wavefronts.

First order statistics of the OCT speckle are simplified with the assumption that a speckle pattern is generated by the summation of random small angle scattering events from a high concentration of sub-resolution scatterers, where the scattered light's complex phase is uniformly distributed. The real and imaginary wave amplitude components (U_{re} and U_{im} respectively) combine resulting in a probability density function (PDF) of [86, 87]:

$$p(U_{re}, U_{im}) = \frac{1}{2\pi\sigma^2} \exp\left\{ -\frac{U_{re}^2 + U_{im}^2}{2\sigma^2} \right\} \tag{3.3}$$

This PDF is a product of two Gaussian distributions. Its shape is dictated by a combination of specular and diffuse reflections (where specular reflection is the deflection of light along a single angle and diffuse reflection implies multiple angle scatters - such as in Mie theory or Rayleigh scattering). For a fully developed speckle pattern, a purely diffuse regime is established, resulting in a Rayleigh distribution, which equates to an imaging scenario where individual scatterers are not pictured. Whereas, in a region of only single scatters, the PDF is approximately Gaussian and individual scatterers can be identified in the image. It also indicates a large specular contribution, with a negative exponential form more akin to the simple light attenuation model previously described in Chapter 2 [58]. All PDFs belong to the Rician distribution family. These are the characteristic PDFs for a large collection of random variables with a normal distribution, finite mean and variance. The function can be rewritten in terms of complex signal intensity like so [87, 88]:

$$p(I) = \frac{1}{2\sigma^2} \exp\left\{-\frac{I}{2\sigma^2}\right\} \tag{3.4}$$

where $I^{\frac{1}{2}}$ is the complex magnitude of the OCT signal and $I = \theta_{re}^2 + \theta_{im}^2$. If the NCC tracking approach is to be effective, the PDF must not be in the fully developed speckle (pure diffuse) regime. The speckle will not contain structural information and, hence, will not exhibit a speckle shift relative to an object's motion. It can be seen that PDFs from a range of materials with differing scattering coefficients are characteristic and relate the degree to which the associated speckle pattern is developed (figures 3.4 and 3.5). Also, under experimental conditions, where large structures are present, speckle is not fully developed or scatterers are unevenly distributed within the sample, the PDF deviates from the Rician distribution. This is due in part to the inhomogenous number density and size distribution of scatterers throughout the object, resulting in varying contributions from independent PDFs, each with its own ratio of specular, diffuse and coherent scattering events [89]; as demonstrated by twin peaks in the PDFs of figure 3.5.

Further to a speckle's PDF, changes in speckle distribution and brightness will relate structural information in tissue. These features can also be tracked using NCC, but they often occupy relatively large regions meaning the sensitivity of displacement estimates would be reduced. Ideally for correlation-based tracking, a speckle pattern should be developed to the point that individual speckles are discernable, but closely packed and stable over the entire displacement.

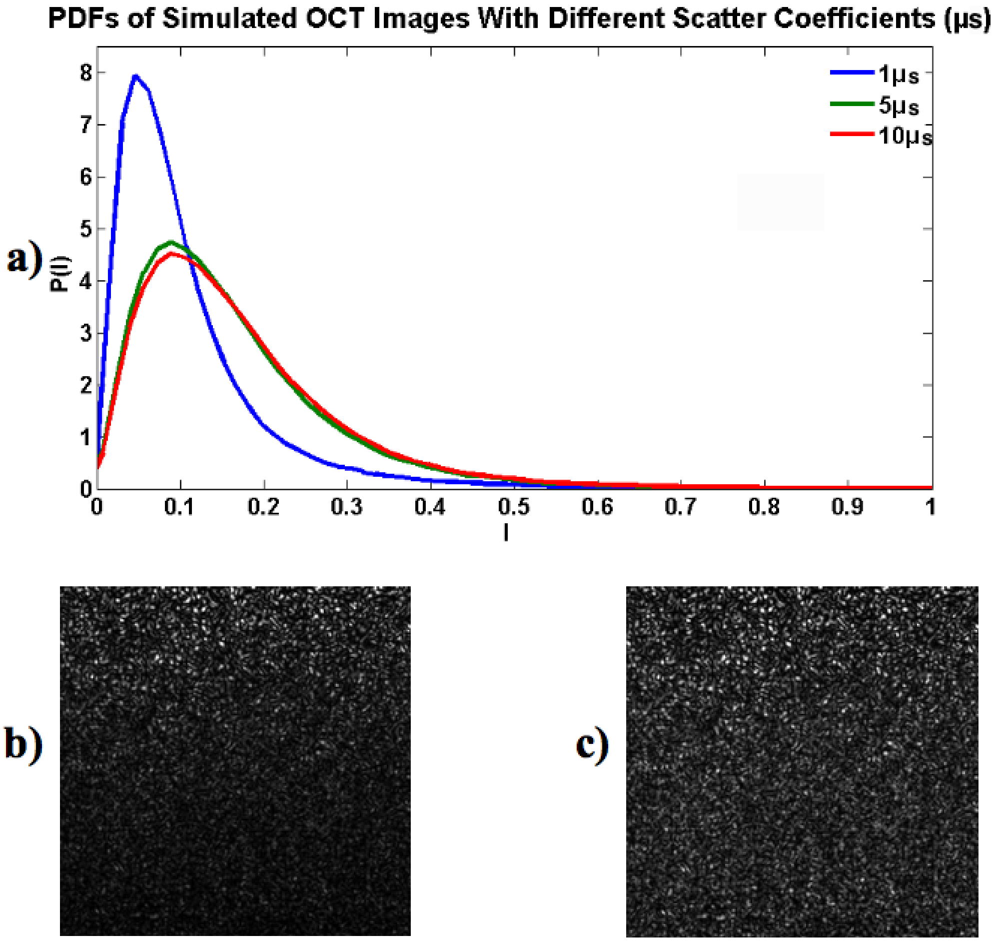

Figure 3.4: a) PDFs as measured from a simulated OCT image when the scatter coefficient μs is varied, changing the intensity distribution of the speckle pattern. The simulated images for relative μs values of 1 and 10 can be seen in b) and c) respectively

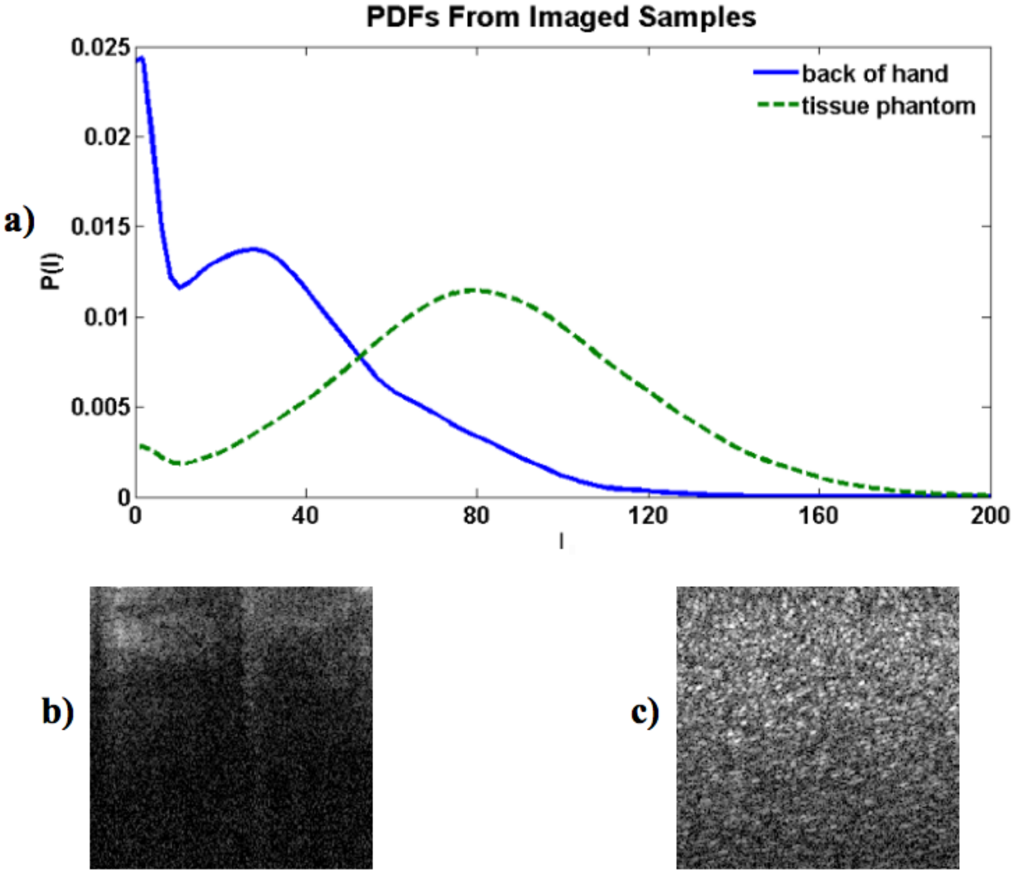

Figure 3.5: a) PDFs measured from actual OCT data and the associated B-scans of b) skin on the hand and c) a tissue phantom.)

Autocovariance and the OCT Signal

Speckle size also influences the tracker's performance, especially regarding the peak interpolation described in section 3.2.1. Second order statistics are used to characterise this feature. Here, speckle size can be analysed by measuring the autocovariance of an image signal. The autocovariance, R, is a measure of variance between two locations within the same image signal (x_n and x_{n+m}) and can be described as:

$$R(m) = E\left\{(x_{n+m} - \bar{x})\,(x_n - \bar{x})^*\right\} \tag{3.5}$$

where, E is the expectation value operator and $\bar{x}$ the signal average. The normalised autocovariance function can be likened to the autocorrelation function, which is an implementation of equation 3.2 where an image is correlated with itself.

To illustrate the dependency of autocovariance peak width on speckle size, the autocovariance functions of simulated OCT images are shown below in figure 3.6 (all simulations are derived from open-source code, written described in literature and written by S. J. Kirkpatrick et al. [88, 90]). It can be seen that an increase in peak FWHM accompanies an increase in speckle size. However, the degree to which a local speckle distribution is developed may also generate variations in the autocovariance peak width, as can be seen when sampling the function for the lateral speckle dimension in a B-scan of skin (figure 3.7). For regions of over developed speckle, the effective speckle size extends of many pixels and there is little structural information within the region. This would result in high decorrelation rates for NCC tracking unless the kernel size is increased to incorporate the entire region.

Analysing the autocovariance function is a useful tool for image characterisation and should be considered when selecting a kernel's size. However, the shape of the autocovariance function is also important with respect to the correlation peak interpolation process described in section 3.2.1. Estimations of the peak's maximum become less accurate if the peak is broad, where a broad autocovariance function peak equates to a broad correlation peak. Conversely, a sharp peak will improve the accuracy with which its location can be estimated [84, 91]. In ultrasound, this often results in preferential use of the RF image signal for correlation-based tracking, instead of its envelope (usually used to form B-scans) [91]. Based on this single assumption, it seems wise to examine a raw OCT image signal and the autocorrelation functions taken at different processing stages when forming a B-scan. A preliminary decision can then be made as to how far down the processing chain an image should go before using NCC tracking. The basic signal processing stages are depicted in figure 3.8.

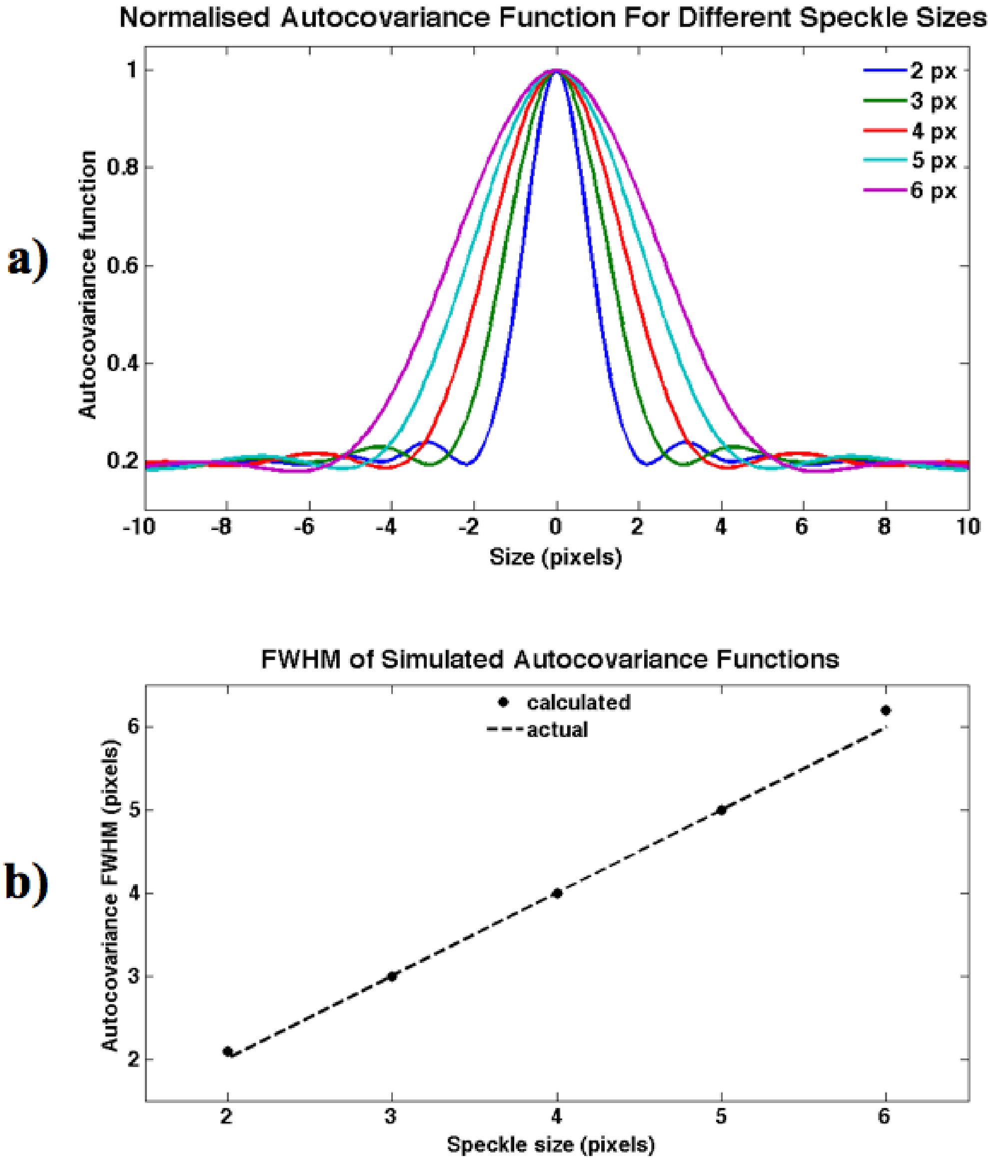

Figure 3.6: The normalised autocovariance functions for simulated OCT images with different speckle sizes are shown in a). The peak full width half maximums are plotted against the actual speckle sizes in b).

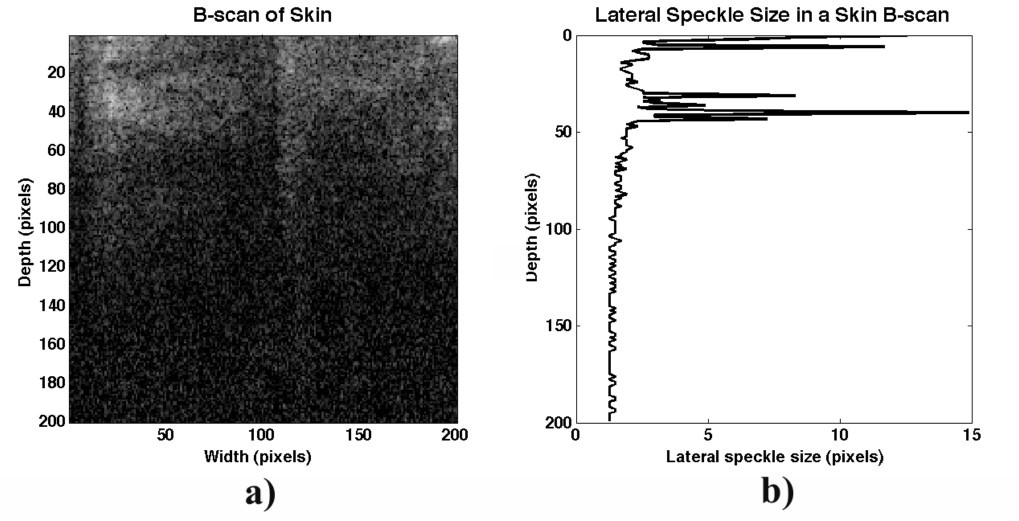

Figure 3.7: a) OCT image of skin from the back of a hand and b) speckle width calculated from the lateral autocovariance at various depths.

Autocorrelation functions of a signal were computed for specific stages in the processing sequence (figure 3.9). These were specifically: the real component of the complex signal, the magnitude of the complex signal, the signal intensity in dB ($20log10$), and the final thresholded image. Whilst thresholding is often desirable as a noise reduction measure when viewing OCT images, it could potentially impede speckle tracking.

Also, it must be noted before continuing that the complex signal intensity should, strictly speaking, be defined as the magnitude squared ($|V|^2$). However, from this point on the term will refer simply to the complex magnitude, $I = |V|$.

From the results it can be concluded that speckle size appears smaller before log compression of the signal. Thus, correlation peak interpolation and the resulting displacement estimates will be more reliable if the tracker is applied to OCT data pre-compression.

3.3 Optimising NCC Image Tracking

Carrying on from the previous section, the focus will now shift from characterising the images to applying the NCC algorithm. Its performance will be measured by analysing decorrelation rates, accuracy and artefacts. The results will be compared at each stage of the image processing sequence previously highlighted in figure 3.8. Additionally, the effects of oversampling and averaging A-lines are shown. This averaging process is an optional setting for Michelson systems which is designed to

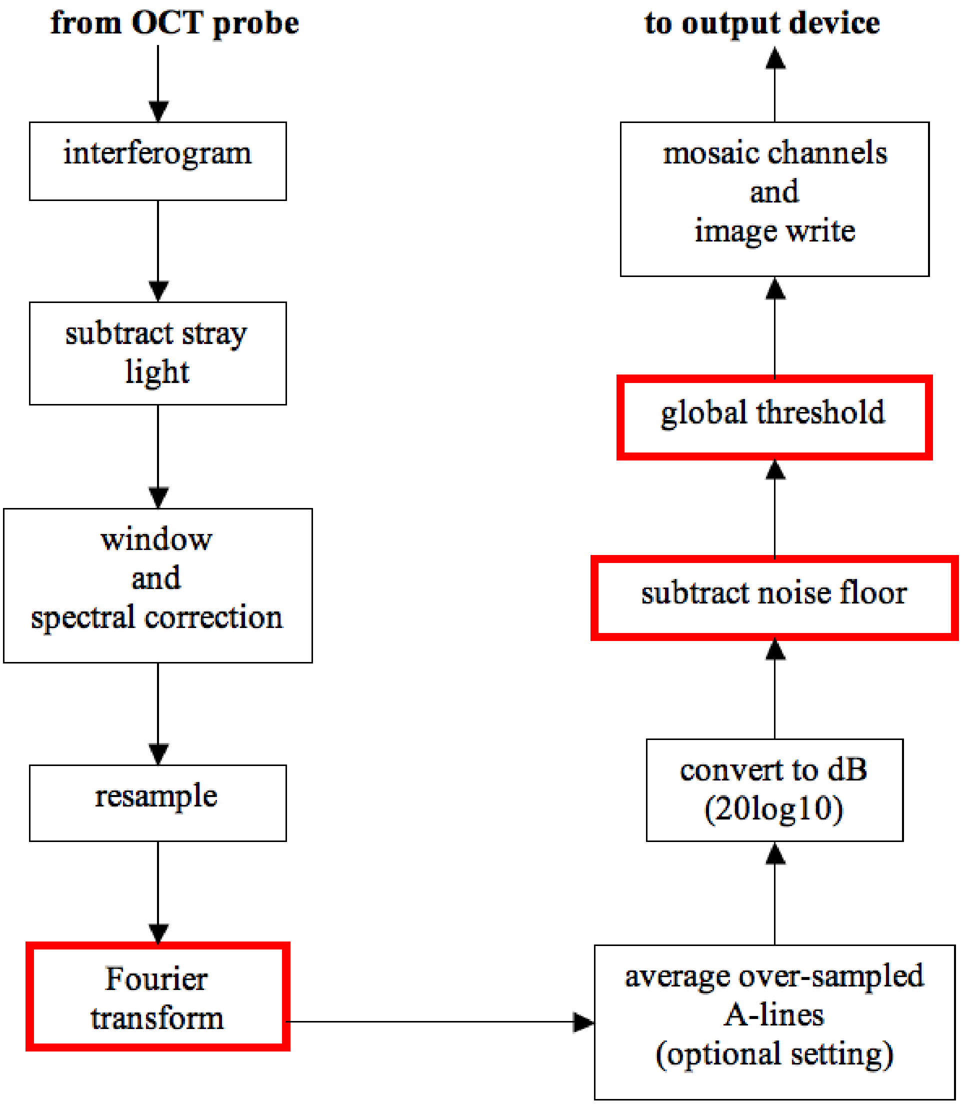

Figure 3.8: Image processing sequence. The highlighted stages indicate which points autocovariance was calculated. At the Fourier Transform, the real component and magnitude of the complex signal was analysed. After subtracting the noise floor an intensity image was analysed, and finally, the thresholded image was analysed. A single image channel was considered and the multi-channel mosaicing process has not been illustrated here.

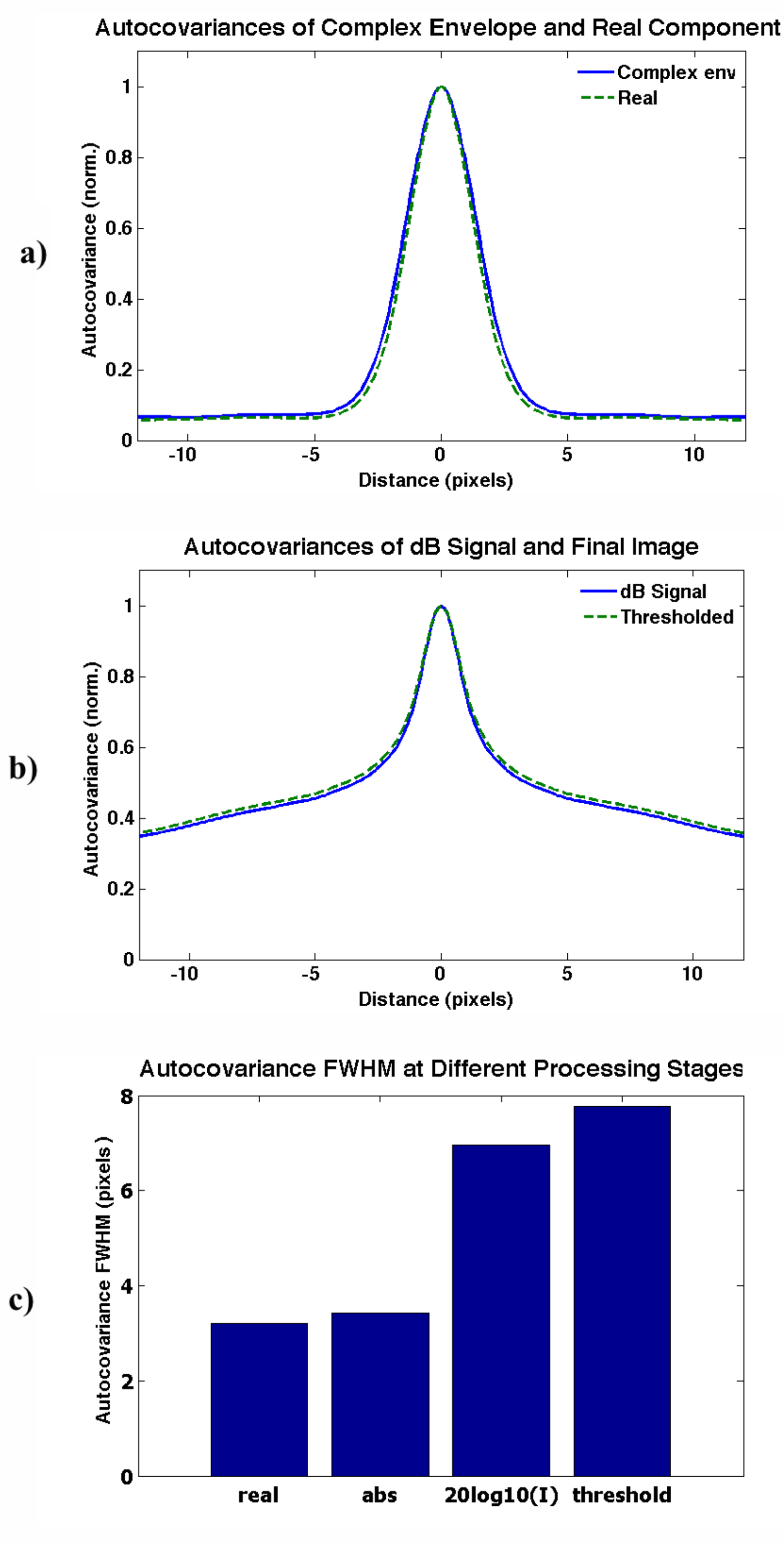

Figure 3.9: Autocovariance functions at different stages of the image processing sequence a) before log compression and b) after log compression. FWHM of each curve is shown in c).

reduce background noise. Finally, the effect of kernel size on displacement estimates is illustrated. For a baseline set of results, the complex magnitude signal (I) was analysed. Here, the imaged object is a phantom similar in construction to those described in Chapter 2, where TiO_2 is mixed into an epoxy resin compound to produce a scattering medium with clearly defined structural speckle. A series of B-scans was captured as the phantom was translated vertically at a rate of 7.5 μm per frame. A single frame and the tracking performance are depicted in figure 3.10. It can be seen that the mean correlation coefficient value has a downward trend, while its standard deviation increases. This reflects a rise in estimation error, which is clearly demonstrated at frame ten in figure 3.10, where a wide variation of displacement values is recorded (as indicated by the error bars). The erroneous displacement values are likely a direct consequence of small correlation function peaks (peak values being the correlation coefficient); as their size decreases, the likelihood of detecting a side peak instead of the main peak increases, resulting in an inaccurate displacement estimation. This can be considered as a type of imaging artefact arising from speckle decorrelation between frames.

3.3.1 Real Component of Complex Signal

The OCT system detects an interference pattern, which is then Fourier transformed to produce an A-line signal. The Fourier domain signal is complex and its magnitude (I) forms the A-scan. This complex signal can be considered equivalent to the real RF carrier signal in ultrasound. As has been mentioned already, there is a measurable performance improvement when applying NCC to the RF signal instead of its envelope (complex magnitude). In an attempt at recreating a similar improvement for the OCT signal, the real component was tracked and the results are shown in figure 3.11. The results show that decorrelation is higher for the real component compared to intensity. There is greater variation in both correlation and displacement estimates, indicating a higher margin of error and higher rates of decorrelation.

3.3.2 Log Compression and Noise Floor Subtraction

Converting the OCT intensity signal into decibels (dB) is achieved through taking log_{10} of the complex magnitude and multiplying by 20. This compresses the signal's dynamic range, making it easier for the OCT system user to interpret [92]. Log compression also retains information across the entire intensity range without significantly reducing signal resolution when converted into an 8-bit format. However,

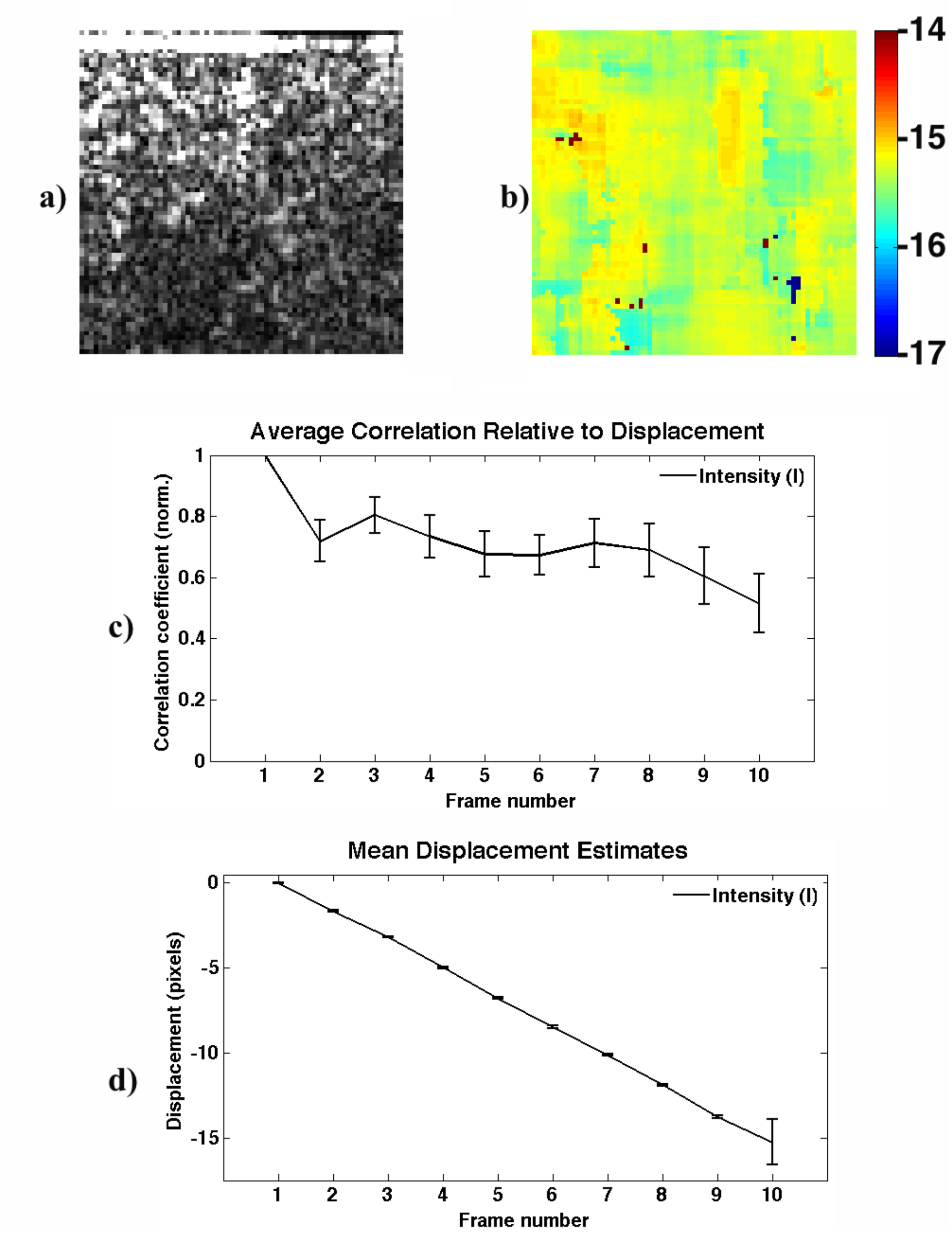

Figure 3.10: The data from a ten frame image sequence of a tissue phantom undergoing an axial translation of 70 μm is shown. Data on a 70×70 pixel region was recorded a) A single frame: intensity (I) image of the 70 pixel region – the colour range has been altered to make more detail visible, b) the axial displacement map after translating 70 μm (frame ten), c) mean estimated displacement with error bars representing two standard deviations, d) mean normalised correlation coefficient, error bars are again two standard deviations.

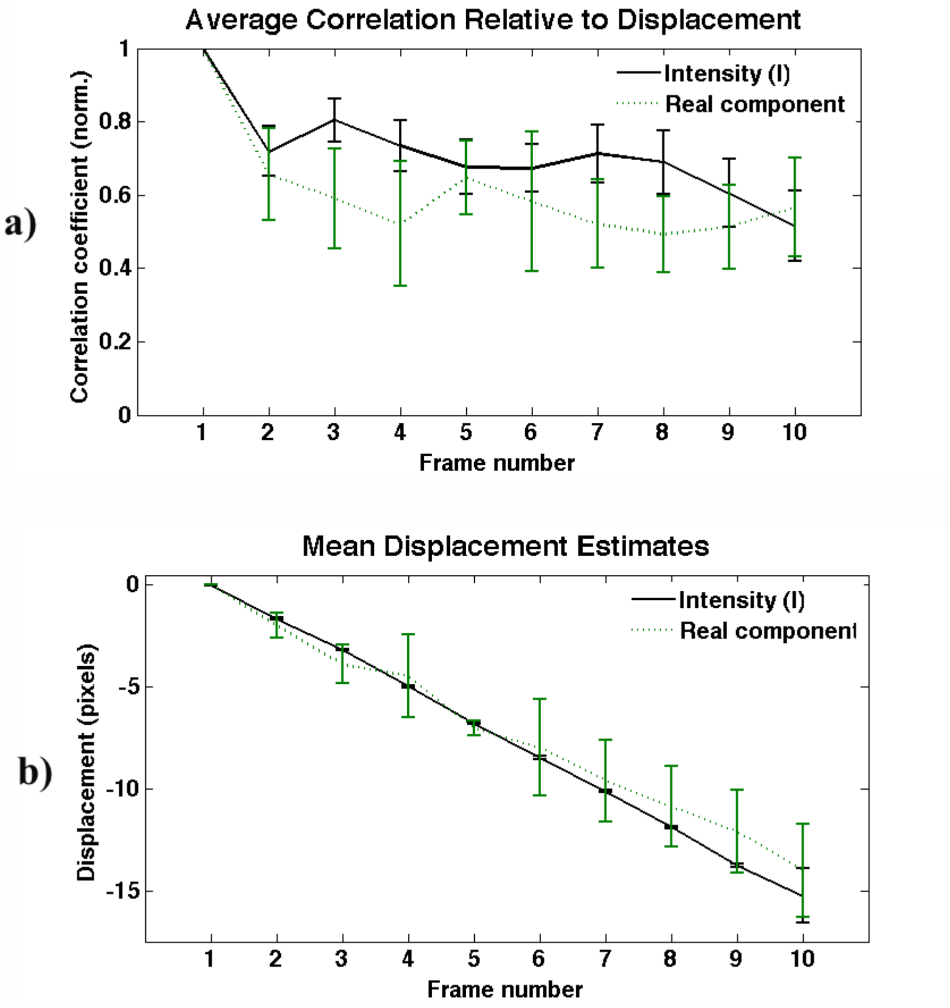

Figure 3.11: NCC data comparison between the complex OCT signal's real component and magnitude (intensity). a) mean correlation coefficient for each frame of the same 70×70 pixel region undergoing vertical translation and b) the resulting mean displacement estimates.

it does result in a measurably larger speckle size. This arises because the FWHM of a signal peak broadens under log compression as its relative height decreases. Consequently, the decibel NCC output (figure 3.12) exhibits more decorrelation and larger displacement estimation errors in frames 9 & 10 where the mean normalised correlation coefficient recedes below 0.5. The implication for NCC tracking is that the original OCT complex magnitude signal provides more robust displacement data, especially for larger translations.

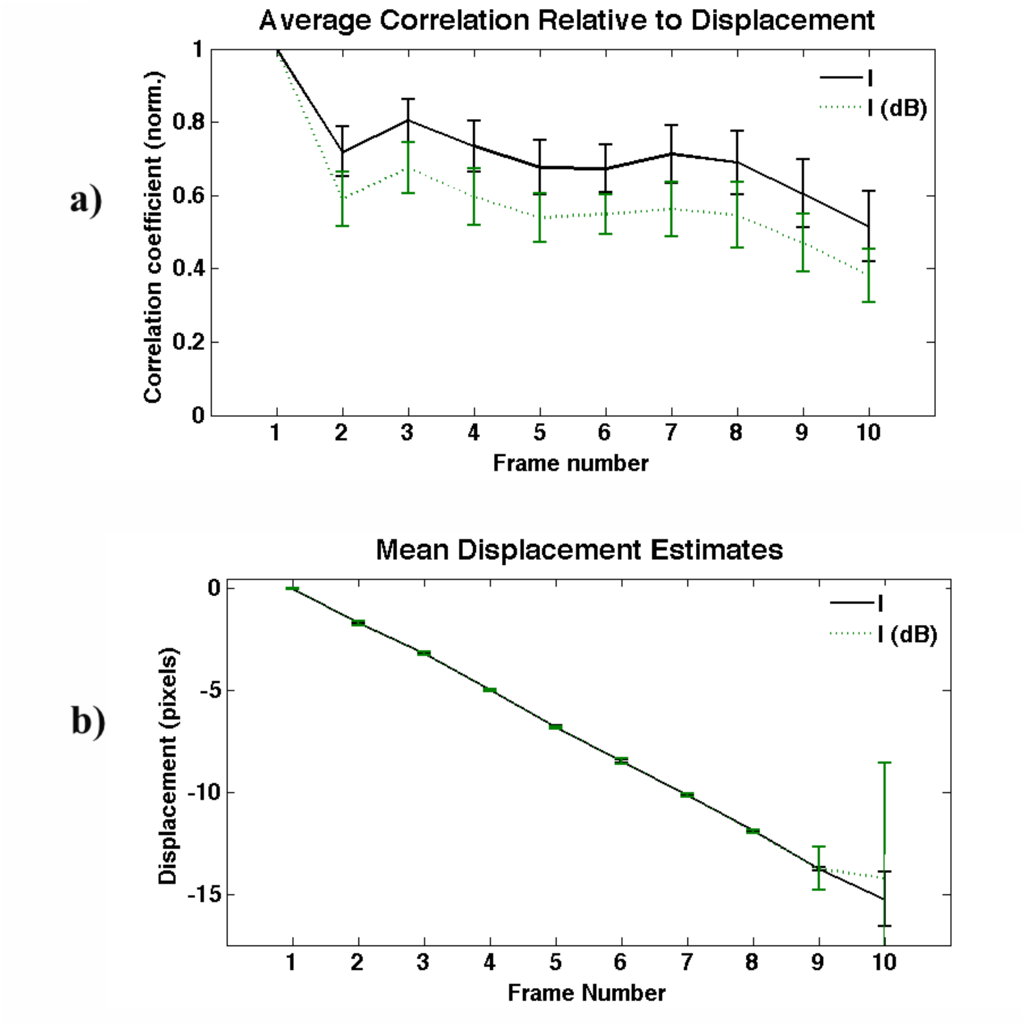

Figure 3.12: NCC data comparison between the original OCT complex magnitude (I) and its magnitude in dB. a) mean correlation coefficient for each frame of the same 70×70 pixel region undergoing vertical translation and b) the resulting mean displacement estimates.

3.3.3 Applying a Global Threshold

Here a global threshold is applied, restricting dynamic range to values between 65dB and 105dB after noise floor subtraction. The thresholded image is converted into an

8-bit greyscale format with 256 intensity levels. This is analogous to the final OCT B-scan image typically viewed by a system user. When NCC performance of this thresholded image is compared to that of the dB image, a minor increase in performance can be noted within the 70×70 pixels region. This seems counter-intuitive because converting the intensity into an 8-bit format should result in an image with less detail, making motion harder to track. However, performance is enhanced through the noise reducing effects of subtracting the noise floor and thresholding. The result is a more stable speckle pattern (figure 3.13).

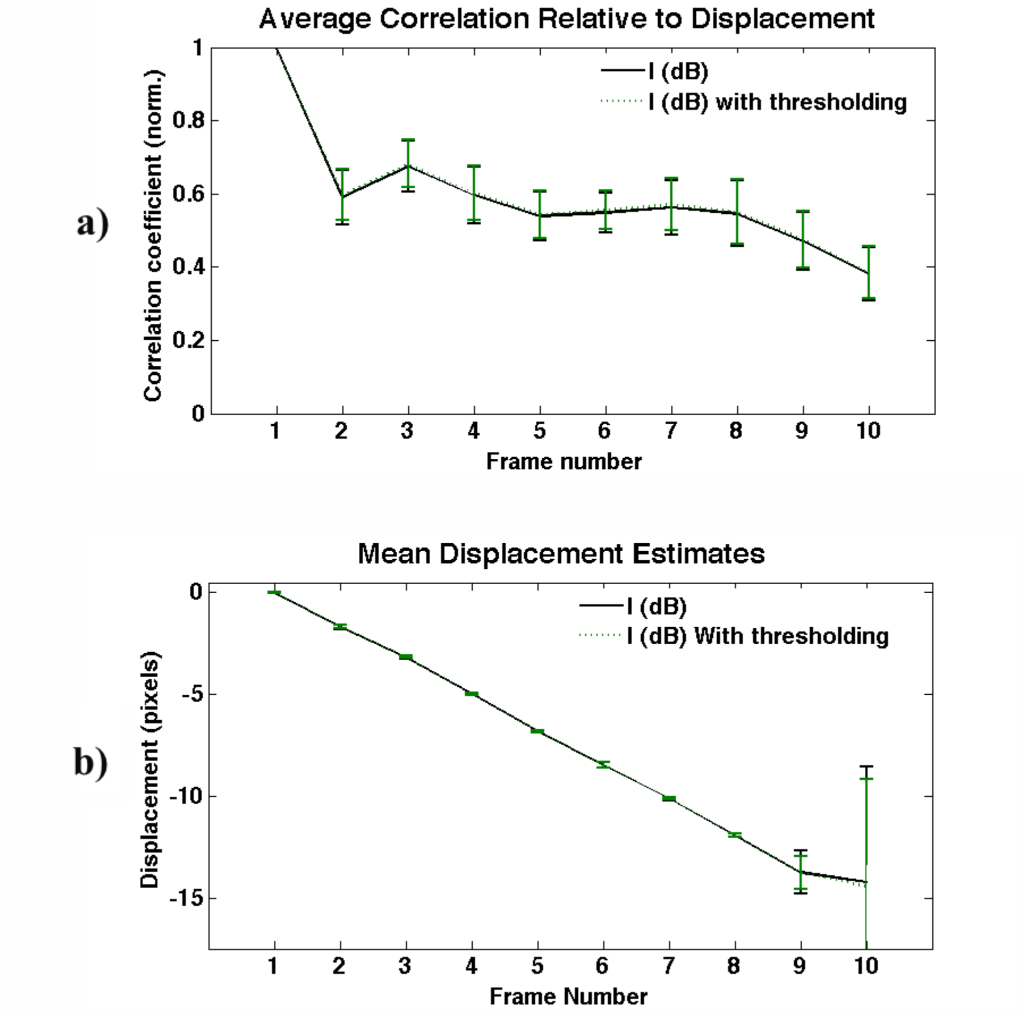

Figure 3.13: NCC data comparison between the dB image signal before and after thresholding (and noise floor subtraction). a) mean correlation coefficient for each frame of the same 70×70 pixel region undergoing vertical translation and b) the resulting mean displacement estimates.

3.3.4 Kernel Size

The accuracy of displacement estimates is affected by kernel size, where the kernel is effectively the feature which is to be correlated. A larger kernel equates to a more complex (and thus unique) feature, reducing the likelihood of spurious correlation estimates. So it would be expected that performing NCC with a relatively large kernel should produce a more accurate displacement map. However, it has also been noted that as the kernel size increases, spatial resolution is reduced and motion within the feature region becomes averaged out. This leads to a reduction in estimated displacement relative to the actual value. Furthermore, there is an increased computational cost associated with large kernel sizes [93, 84, 75] . Thus, minimum and maximum bounds are placed on kernel size. For the minimum, it has to be large enough to accommodate enough detail within the speckle pattern, so that the feature is relatively distinct. The upper bound is dictated by the required sensitivity of the algorithm, this makes NCC better suited to tracking multiple pixel translations, provided the speckle remains correlated. Figure 3.14 illustrates the importance of the lower bound limit for frame number ten, where kernel sizes of 5, 10, 15 and 20 pixels are used to illustrate how a larger kernel can reduce the likelihood of correlating the feature with an unrelated portion of speckle. For all kernel sizes, their mean correlation coefficients are relatively similar. However, the variation of displacement estimates is larger for small kernels – suggesting the NCC algorithm is forming correlations independent of image translation.

3.3.5 Averaging

A feature of Michelson Diagnostics OCT systems is a setting enabling the user to oversample and average each A-line. For an averaging factor of 5, the A-line density across a B-scan is five times higher. An individual A-scan is subsequently formed from the mean of five adjacent lines. Thus the output B-scan is the same number of lines regardless of averaging factor. Averaging is a noise reduction technique based upon the principle that system noise is dynamic and can be averaged out over a number of samples, producing a more stable speckle pattern whilst accentuating structural detail within the B-scan. Figure 3.15 shows the correlation and displacement statistics for frame ten as measured with averaging factors of 1 and 3. There appears to be a marginal performance improvement for the larger averaging factor, although at the sacrifice of quicker acquisition times (An averaging factor of 3 takes three times longer to acquire). The slow rate of acquisition could potentially degrade results of biological specimens which are more prone to turbulence and movement

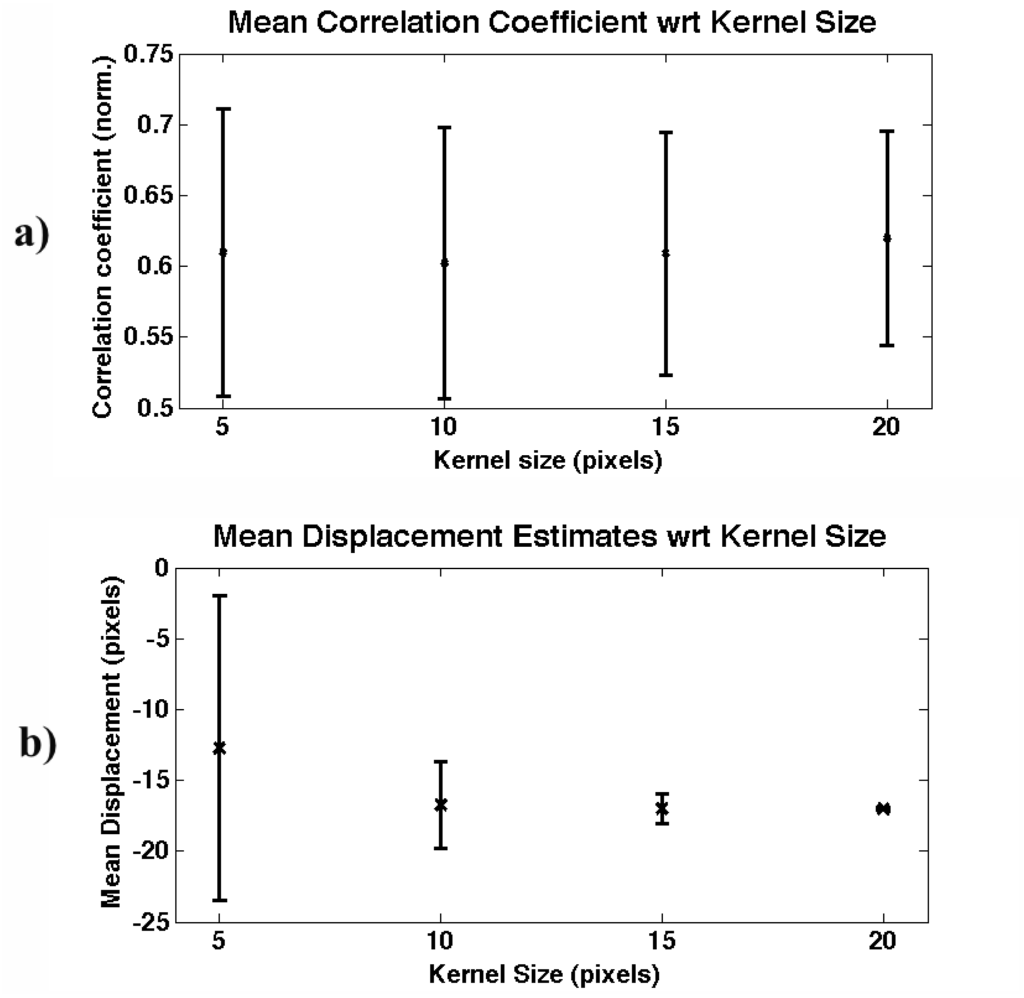

Figure 3.14: NCC data for frame ten using a range of kernel sizes (5, 10, 15 & 20 pixels). a) Mean correlation coefficients with error bars depicting 2× st.devs. b) Mean displacement estimates clearly with error bars of 2× st.devs clearly showing an increase in accuracy with larger kernel size.

from mechanisms such as blood flow etc. Furthermore, certain imaging artefacts, which shall be described in section 3.4, are accentuated by the use of averaging. These have a consequent effect on the uniformity of strain estimates and averaging is therefore not recommended for NCC tracking.

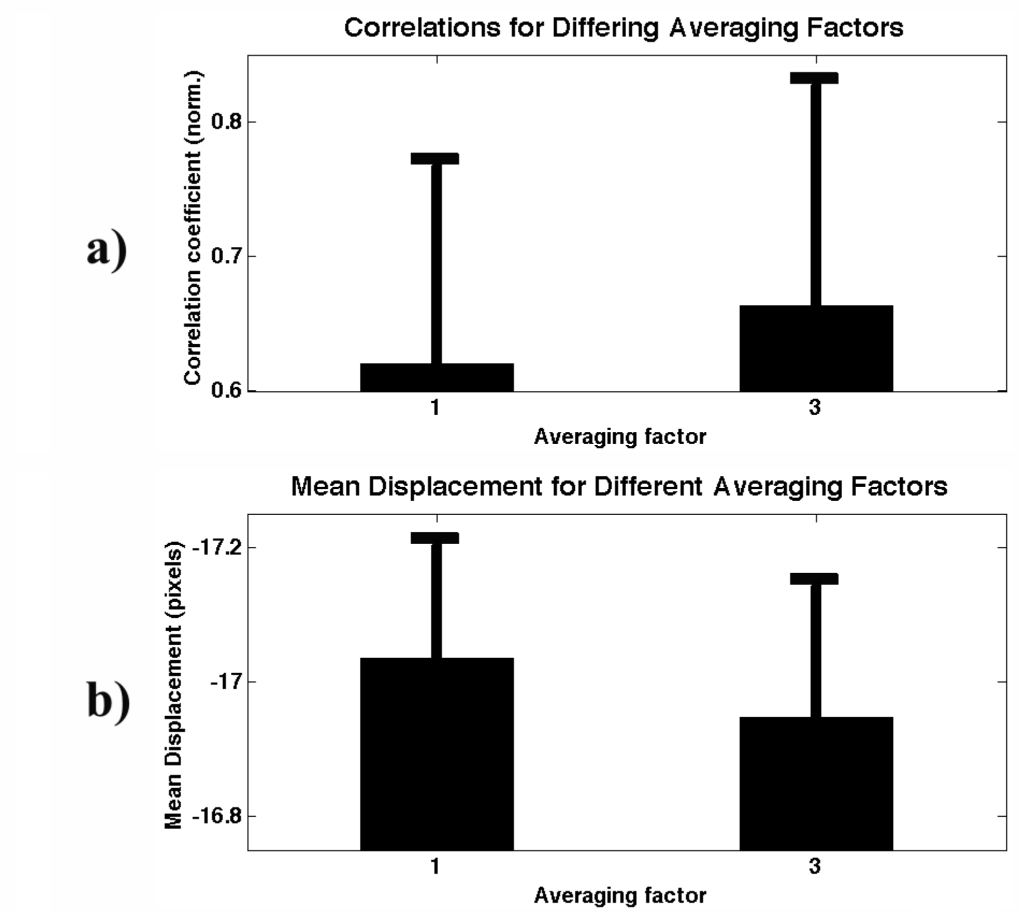

Figure 3.15: NCC data comparison between averaging factors for frame 10. a) mean correlation coefficient for each frame of the 70×70 pixel region undergoing vertical translation, with the vertical error bar representing two standard deviations. b) the resulting mean displacement estimates with error bars again representing two standard deviations.

3.4 Artefacts

NCC tracking is prone to generating artefacts in the final displacement data. These arise from the shape of the correlation function and can be manipulated to some degree by choosing appropriate parameters, which adds another dimension when optimising the tracking procedure. It is especially important that artefacts are kept to a minimum if displacement estimates are used to calculate strain maps, because the strain estimation process amplifies any anomalies or noise that might be present.

The effect of one artefact has already been addressed when describing kernel size, where correlations are made between unrelated regions of an image. The cause of these spurious correlations are briefly described below. Another artefact results from interpolating the correlation function peak – a useful tool for tracking fractional pixel displacements. It has previously been referred to by others as jitter and its roots are explained here too, along with its implications [84].

3.4.1 Spurious Correlations

As previously seen, reducing the kernel size leads to greater variations in displacement estimates. This is because the correlation function across a search region will contain multiple peaks signifying areas with features similar to the kernel. Spurious correlations arise under two circumstances, each leading to the same result. Either: there are many regions closely resembling the feature being tracked (an effect that can often be countered by increasing the kernel size); or the main correlation peak's size decreases until it is indistinguishable from side lobes in the correlation function. This arises when decorrelation occurs. The NCC algorithm will simply record the first tall peak it comes across, regardless of its position. If there are many peaks of equal size, there is no guarantee that the peak most likely related to the translating feature will be chosen. Both causes (self similarity and decorrelation) result in large, multiple pixel jumps in the displacement estimate map. The best mitigating action is to ensure images remain well correlated between frames by minimising disruptive effects such as out of plane motion or speckle decorrelation from very large object movements. By selecting a suitable kernel size and taking the suggested precautions, spurious correlation can be kept to a minimum. Reducing spurious correlations is a priority for biological imaging where decorrelation rates can be higher compared to static objects. As a result, a number of enhancements to standard NCC tracking have been suggested by others, such as multi-resolution tracking, feature-based NCC and pulse shaping (in ultrasound) [76, 94].

3.4.2 Peak Locking (jitter)

Jitter is an artefact characterised by small (within the autocovariance peak), periodic shifts in displacement estimates. With the NCC algorithm used in this thesis, it appears as a result of interpolating the correlation function before locating its peak. For an homogenous speckle distribution, interpolation produces a minor bias in the displacement map towards the nearest whole pixel value (as noted already and seen in figure 3.3). Additionally, in the presence of an unusually bright image region, a periodic sequence is overlaid onto the displacement estimation data as the kernel is swept across. The magnitude of these jitters increases for regions of larger and brighter speckle. For example, a reflective surface will generate a clearly defined displacement estimate jitter. It is also affected by kernel size; the periodic trend appears either side of the bright image region at a distance relative to kernel size. This is demonstrated for an image A-line with a well defined intensity peak under autocorrelation in figure 3.16. The figure also shows a similar autocorrelation where there are a number similarly sized peaks of more uniform intensity, producing less pronounced jitter. Such a characteristic means a user may find it beneficial to log compress their image data if jitter is proving to be a hinderance. However, as already noted, log compression increases the likelihood of decorrelation errors. In Appendix C, the correlation peak behaviour during autocorrelation is visualised as a kernel passes over a peak in the A-line intensity. The interpolation process is highlighted, demonstrating this to be the point at which jitter arises.

Jitter is also problematic when incremental displacement estimations are combined. This is a technique often used as a means of reducing decorrelation noise and errors [95], whilst allowing displacements to be estimated for translations over relatively large distances. An image sequence of a moving object is collected and the NCC tracker is optimised to estimate displacement between adjacent frames. These estimations can then be summed to produce a displacement map over the entire translation range. If the image has structural details that produce regions of large, high intensity speckle, jitter will become visible in the displacement data. Furthermore, by summing over the series of displacement maps, the jitter artefact will be reinforced when motion between frames is small. If motion between frames is more than a few pixels, the artefact will be realised across multiple locations of the summed displacement map, because it will track the bright feature as it moves. In figure 3.17, a displacement map formed from averaging a sequence of sequential estimates is shown. the artefacts can be seen and clearly linked to bright regions of high scatterer concentration.

3.4.3 Channel Banding

For all Michelson Diagnostics OCT systems, the final image is a composite produced from four separate images taken simultaneously by four separate image channels. The depth of focus in each channel is offset slightly from the others; additionally, there is a lateral offset between each channel, which is also corrected for in the final image. Both factors result in a subtle discontinuity of the speckle pattern at

a)

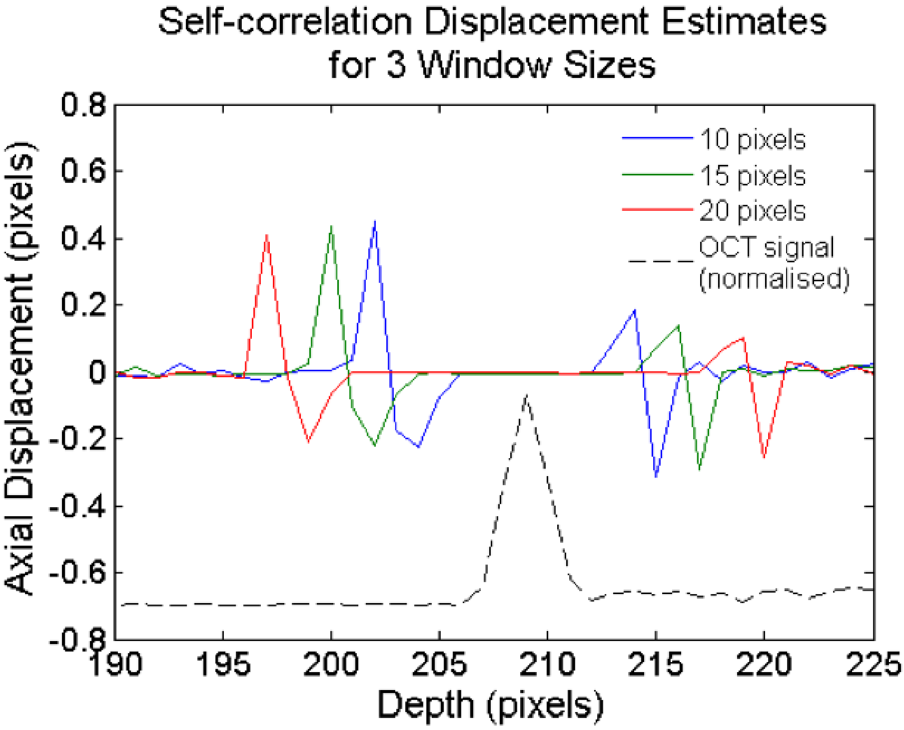

b)

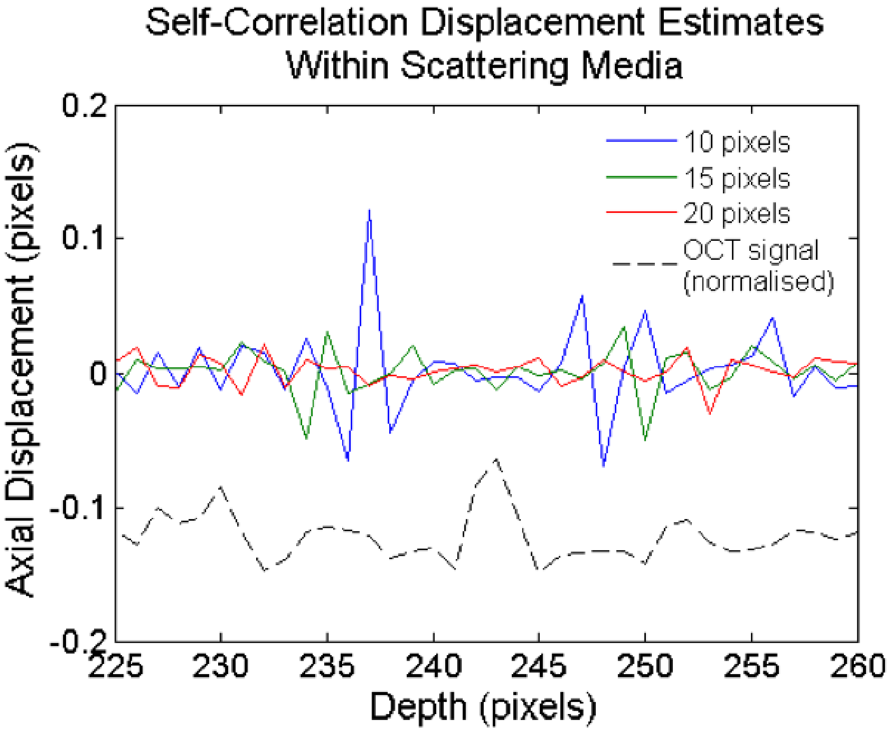

Figure 3.16: Autocorrelations across a portion of a single A-line executed using different kernel sizes where: a) only a single, high intensity peak is present in the image data; and b) a number of relatively similar peaks are present in the image data, showing a consequent decrease in jitter magnitude.

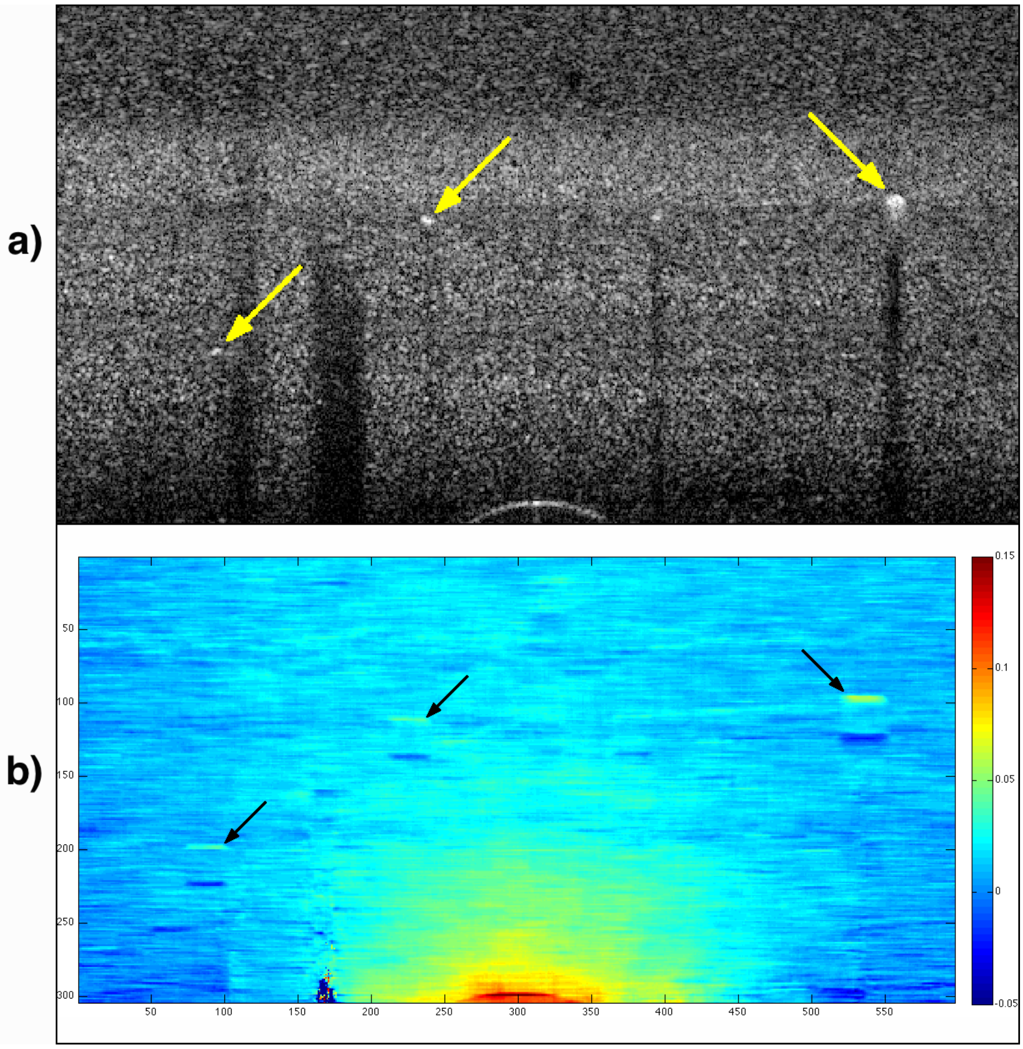

Figure 3.17: Axial displacement map (b) composed by sequentially analysing a 20 frame image sequence and then averaging together their displacements. The curved surface at the bottom of the OCT image (a) is the top of a ball bearing, which is being pulled downwards, creating the distinctive radial displacement distribution. sources of the jitter artefact are indicated by arrows for three especially prominent cases. Colour scale in pixels.

the channel boundaries in the final image. This arises because the speckle pattern at any given location is dependent on the optical path lengths of any scattered light interfering at the detector, which contributes to that specific speckle. If the position of the channel changes, so do any associated path lengths, meaning the signal contribution from each channel will vary. An experimental treatment of this problem can be found in chapter 4.

3.4.4 Potential Mitigation Techniques

Two methods of mitigating the above artefacts have been investigated. The most straight-forward is negation of channel banding. This is a simple process in which the image tracking algorithm is applied to each channel separately, with the final strain and displacement maps produced by stitching this data together (as mentioned before this can be seen in Chapter 4). Another mitigation technique that has been explored is the use of a multi-resolution tracking approach. In this thesis, the method involves taking three correlations of the same image set and combining the displacement data via a weighted average linked to the correlation coefficient:

$$\bar{D}(x,y) = \frac{d_1(x,y)\,(c_1(u,v)) + d_2(x,y)\,(c_2(u,v)) + d_3(x,y)\,(c_3(u,v))}{c_1(u,v) + c_2(u,v) + c_3(u,v)} \tag{3.6}$$

where, $\bar{D}(x,y)$ is the weighted average displacement at a given pixel location (x,y); d_1, d_2 and d_3 are the three estimated displacements and c_1, c_2 and c_3 are the respective correlation coefficients for those displacement estimates.

The three image tracking runs are executed for differing levels of detail and resolution. This approach employs differing kernel sizes as well as differing step sizes, where step size is the distance between successive searches in an image. By increasing step size, resolution is degraded and the associated dataset is reduced in size. A step size of 1 pixel (known as an exhaustive search) is usually applied throughout this thesis with the exception of the multi-resolution technique described here. Once all three displacement maps have been obtained, the low resolution datasets are up-sized to match the exhaustive search dataset. Bicubic interpolation is applied to smooth the up-sized data. Next, a weighted average is taken at each location for each of the three displacement values against their related correlation coefficients (the low resolution correlation maps are similarly up-sized). This results in a final displacement map. The approach combines a quality-guided method, whereby the influence of a specific displacement value is weighted against its correlation coefficient, with a multi-resolution approach, where some detail is initially sacrificed to produce a smooth (but low resolution) displacement map and this detail is partially reintroduced by combining iteratively higher resolution datasets. The parameters for a multi-resolution search and the final displacement data produced from a weighted average of the three can be seen in table 3.1 and figure 3.18. The results show a decrease in overall estimation error, however, the average displacement estimations remain unchanged.

Search number	Kernel size	Step size
1	25	10
2	20	5
3	15	1

Table 3.1: Parameters for each of the 3 searches used in the multi-resolution technique.

3.5 Strain Estimation

The NCC image tracker produces two displacement maps, one for the axial component and another for the lateral. These datasets can be used separately or in tandem to calculate a strain estimation. In all cases, the fundamental process remains the same. This comprises application of a smoothing filter to the displacement maps, reducing noise and the effects of artefacts. Strain can be thought of as the derivative of displacement, i.e. its rate of change, thus the next step is application of a gradient estimation function along a 1-D section of the data. The calculated gradient value is mapped to the centre of this section and the process repeats for all possible regions within the displacement data. This produces a strain map. The orientation of the 1-D section (vertical or horizontal) and the component of displacement being analysed dictates the kind of strain being estimated. Some relevant strain components are shown in table 3.2, all of which can be calculated using the lateral and axial displacement outputs from NCC tracking.

Although Matlab has a native gradient estimation function, better results were possible through calculating gradient along the 1-D section by fitting a first order polynomial. However, this approach is computationally more expensive. The strain estimation technique is based on the least squares strain estimation (LSQSE)

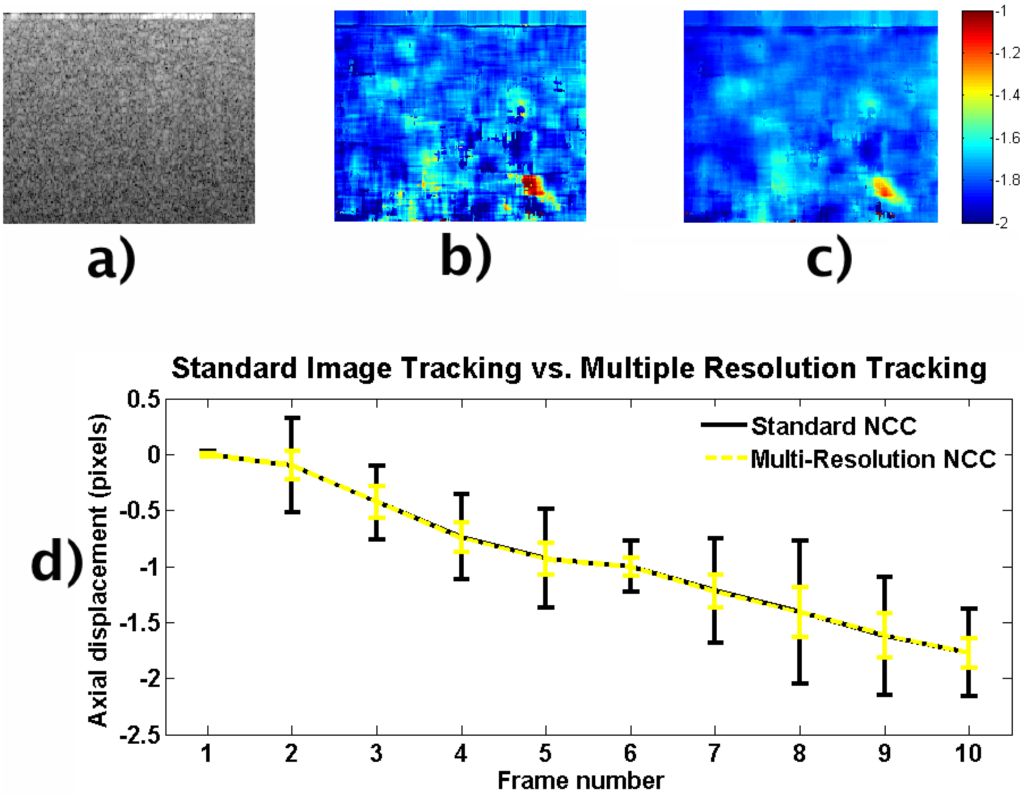

Figure 3.18: Displacement data for an axially translated tissue phantom image sequence represented by a single frame in a). The displacement map from frame ten for a standard exhaustive search is shown in b). A comparable multi-resolution map using the parameters in table 3.1 is shown in c). The mean displacement data for both techniques is plotted in d), with error bars equivalent to two standard deviations.

Displacement Components	Axial displacement	v
	Lateral displacement	u
Strain Components	Axial normal	$\frac{\partial v}{\partial y}$
	Lateral normal	$\frac{\partial u}{\partial x}$
	Axial shear	$\frac{\partial v}{\partial x}$
	Lateral shear	$\frac{\partial u}{\partial y}$
	Total shear	$0.5\left(\frac{\partial v}{\partial x}+\frac{du}{dy}\right)$

Table 3.2: Displacement & Strain Components

method, because its piecewise approach improves strain signal to noise (in the presence of uncorrelated noise) compared to a standard gradient calculation [78]. However, where noise is correlated (as is the case for artefacts arising from jitter, which produce displacement values in response to structural detail rather than motion) the information may be retained and amplified along with other variations in displacement. This can be seen in figure 3.19, where the strain estimator is applied to displacement data arising from an autocorrelation of a tissue phantom. Although displacement and thus strain are practically zero, variations appear within the strain data. These are further enhanced when the OCT system's averaging factor is increased – most likely in response to the decrease in decorrelated noise.

The strain estimator incorporates a 2-D median filter. Its window size can be selected to optimise the balance between loss in spatial resolution and effective data smoothing. The 1-D kernel size is also customisable, allowing further optimisation between noise reduction, sensitivity and resolution loss.

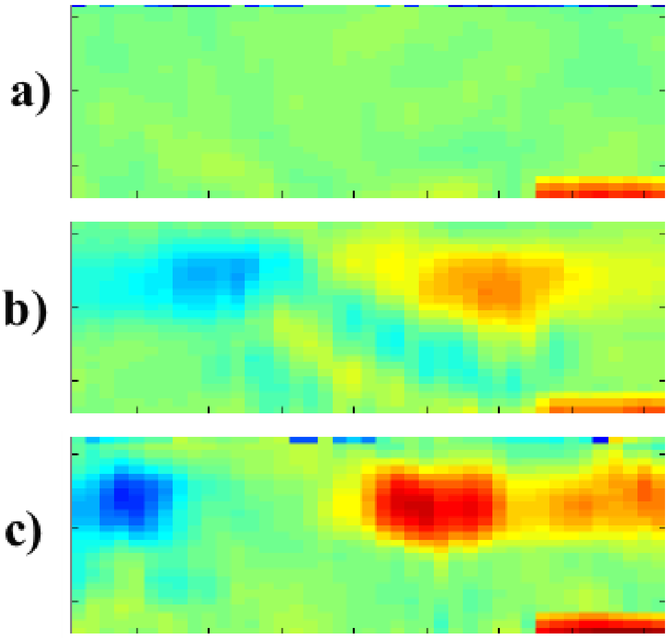

Figure 3.19: Strain maps constructed from autocorrelations of a tissue phantom. The same image sequence was recorded for three averaging factors: 1, 3 and 5; a) to c) respectively. The colour scales are identical across the three figures.

3.6 Discussion

This Chapter has demonstrated the use of NCC to produce displacement estimates with sub-pixel accuracy in both simulated OCT images and phantoms. Sub-pixel tracking requires interpolation of the correlation function's peak, executed here using a second order polynomial.

Correlation tracking is only possible if discernible structural information is contained within the OCT speckle pattern. This was ensured in tissue phantoms by tuning scatterer concentration to produce a slightly under-developed speckle pattern. The degree to which a speckle pattern is developed was characterised by measuring its PDF. Skin images exhibited regions of fully-developed speckle, as seen in figure 3.5, which will degrade the performance of NCC tracking.

Speckle size also affects NCC performance for two reasons. First, it will reduce accuracy when interpolating the correlation peak; Second, it sets a lower bound for kernel size, because the kernel must be large enough to incorporate image features with no internal speckle structure.

OCT signal processing influences NCC performance too. Log compression increases decorrelation, leading to errors in displacement estimation. This appears to be a result of the associated FWHM increase in intensity signal peaks, although a definitive link was not established. Thresholding and subtracting system noise from the image data reduced errors, but did not improve mean correlation. Furthermore, in the MDL system, the noise floor could only be subtracted from the dB signal and could not improve tracking performed on the OCT's complex magnitude.

Kernel size was shown to influence NCC performance and, as mentioned above, must be chosen relative to the image properties. Estimation error can be greatly reduced through increasing kernel size, even though the mean correlation coefficient remains the same. This reinforces the presumption of false correlations occurring when the kernel is too small.

The effect of an increased averaging factor is not immediately obvious in displacement data, however it appears to reinforce artefacts generated by NCC, which become amplified when viewing strain. The two observed artefacts are decorrelation and jitter, which have been previously observed in ultrasound imaging [84].

Strain estimation involves sampling the differential of displacement, which amplifies any trends in the displacement data. This includes both noise and correlation artefacts. As a result, jitter can impede the use of incremental imaging, which had previously been demonstrated to reduce incoherent noise in strain estimates [95]. Strain estimations for this thesis are calculated using the LSQSE technique combined with a median filter. Both processes are designed to mitigate the usually poor SNR associated with finding the derivative of a signal [78].

A number of refinements to the NCC technique have been suggested by previous authors. These include quality-guided techniques combining the use of a-priori knowledge [76]. Anecdotal evidence suggests an improvement in NCC performance can be gained from analysing the OCT signal's complex envelope instead of its magnitude. However this method would require hardware modifications to the Michelson Diagnostics system, including the use of a high bandwidth light source with a wide numerical aperture, and thus could not be implemented [74]. Instead, NCC performance was optimised by analysing the OCT complex magnitude signal and selecting suitable kernel sizes, which required knowledge of the scale of displacements being tracked (figures 3.14 and 3.16).

Artefact mitigation techniques were investigated. In the first instance, three cross-correlations were executed for decreasing kernel sizes. An averaged displacement value weighted against correlation coefficient was then calculated from the three correlations and used to form a single displacement map. This approach reduced overall error, producing a similar effect to a smoothing function without altering mean displacement values. Whilst the presence of artefacts and noise were reduced, this method is computationally expensive, especially when combined with the two further mitigation techniques explored. These were: estimating displacement and strain in each channel before combining them; and using incremental tracking, where displacements between adjacent frames in an image sequence are averaged together.

3.7 Conclusions

This Chapter details characterisation studies implemented on the normalised cross correlation image tracker using simulated and experimental OCT images. The results were used to determine the optimal light scattering properties of the elastography phantom in Chapter 4 and to refine the tracking process. Sub-pixel tracking of displacements is demonstrated to be most effective when applied to the OCT signal before log compression, noise floor subtraction and thresholding. Previous literature in OCT correlation-based image tracking has emphasised the importance of kernel size, this chapter expands upon the literature by providing a discussion on and experimentally verifying the effect of these other factors [74, 51]. A minimum kernel size of 20 pixels has been determined for phantoms. Speckle statistics of skin give an indication that tracking performance in tissue will deteriorate as a result of high decorrelation rates. This can be partially mitigated through the use of a larger kernel size and implementation of artefact reduction techniques. These techniques are computationally expensive as they require multiple cross-correlations and are thus avoided when analysing phantoms. Chapter 4 will address the actual application of NCC for use in elastographic experiments, detailing its relative merits and success.

Chapter 4

Shear Contrast From a Localised Actuation

Having explored the underlying principles of optical coherence elastography (OCE) in previous chapters, a practical demonstration is now described. Optical and mechanical properties of the phantoms are defined and a quantifiable, controlled actuation method employed. This chapter builds upon previous work by demonstrating that elastographic imaging is sensitive to changes in mechanical properties, even if there is no associated scatterer contrast variation through the use of a repeatable controlled actuation. Furthermore it demonstrates the potential value of correlation-based imaging in OCT as a means of evaluating different strain components (most notably shear) [74, 75, 96]. Finally, the use of these techniques in conjunction with MDL's multi-channel system is also shown for the first time.

In this experiment, a magnetically actuated implant imparts a localised actuation within a specimen. This is subsequently imaged and elastograms derived. Descriptions of the elastography phantom, both actuation and imaging apparatus, and a finite element model of the experiment are provided. OCT channels are processed separately to reduce imaging artefacts. Different strain components are also combined into a single elastogram to aid contrast.

Finally, the actuation technique is used to form elastograms in raw chicken, with speckle statistics closer to human skin. Owing to increased decorrelation rates, displacement tracking is carried out using the incremental, multi-resolution method previously described in Chapter 3.

A stiff inclusion is discernible in elastograms from the phantom model. The associated implant actuation is 56 μm. In chicken, decorrelation reduces the maximum trackable displacement to < 9 μm (as demonstrated in Appendix D). However, internal structure is still visible in axial normal strain elastograms.

4.1 Introduction

Skin elastography has been used to differentiate between healthy and diseased tissue such as abscesses, keratoses and psoriases [97, 98]. Reports also suggest elastograms can be used to differentiate between malignant and benign skin tumours using high frequency ultrasound [99, 18]. Elastography can aid cancer diagnosis across a range of cases, with clinical trials currently underway to investigate its use specifically in imaging skin neoplasms [19]. The technique therefore has potential as a diagnostic aid and contrast enhancement technique when imaging skin using OCT.

The technique described in this chapter uses an implant positioned away from the imaged site to enable elastographic measurements of a suspected lesion without physical contact. The implant is remotely actuated using an external magnetic field, producing an associated strain at the lesion. Elastograms are then acquired to generate contrast between structures with differing stiffness.

Both experimental results and finite element (FE) simulations were conducted. For the experiments, phantoms with a superficial resemblance to tissue samples incorporating a stiff surface lesion were fabricated based on the observed properties of melanoma in a rat model [100]. To generate the localised actuation, a small magnetisable metal sphere was also incorporated into the phantom. The FE model was designed to closely resemble these phantoms, producing a complementary set of results. The experiment was finally repeated with a chicken breast, which was deemed to simulate image characteristics closer to human skin. Normalised cross-correlation (NCC) was used to track displacements in the experiments and a least squares strain estimator (LSQSE) was implemented to produce strain maps from this data. More detail on these two techniques can be found in Chapter 3.

It is worth noting that the technique described here could also be employed by a range of imaging modalities other than OCT. Additionally, other actuation methods are also feasible. The metal implant was used because it is an effective tool for generating tightly controlled and repeatable shear stresses, however a more subtle technique would be necessary for future clinical applications where its placement becomes a concern. For example, magnetic nanoparticles have been actuated in tissue to produce elastographic and contrast signals [101, 102]. Such a technique will be discussed in the next chapter.

4.2 Materials and Methods

Elastograms were generated from FE simulations. These were then compared with elastograms taken from OCT images of two phantoms in order to verify observations from the modeled data. For all simulations and measurements, the phantoms were treated as linear elastic solids with minimal visco-elastic properties and Young's moduli based on direct measurement. They generally emulated diseased and healthy tissue with one incorporating a stiff lesion and the other being uniform throughout.The lesion was approximately seven times stiffer than surrounding tissue, a figure previously observed in rat models of melanoma [100]. Mechanical actuation was achieved by remotely pulling on a magnetisable metal implant embedded in the phantom using an external magnet.

Images prior to actuation were correlated with those taken during a constant, applied strain to produce elastograms. Displacement maps were produced in Matlab using NCC with a square reference window 25 pixels wide. Next, an LSQSE incorporating a 15 pixel median filter and 20 pixel estimation window was applied to the displacement data.

4.2.1 Elastography Phantom

The tissue phantoms were fabricated using a two part condensation-cured RTV silicone rubber (MM282-A & B, ACC Silicones Ltd) mixed with silicone fluid and titanium dioxide powder (T/1900/53, Fisher Scientific, UK) at a concentration of 1 mg g^{-1} to promote optical scattering. Silicone fluid (F111/50 polydimethylsiloxane, ACC Silicones Ltd) was added during preparation to tune the phantom's Young's modulus [102]. The mixture was stirred and sonicated for an hour to disperse the TiO_2 before adding the MM282-B catalyst. The stiffer lesion was produced by adding less silicone fluid. To aid dispersion of the TiO_2, hexane fluid was added as a thinning agent at a volumetric ratio of 1:1 before sonication. Finally the mixture was degassed, causing the hexane to evaporate off without affecting the curing process [103], and then cast into moulds. A magnetisable metal implant was incorporated by casting the phantom in a series of layers, such that the top of the implant was 1.58 mm from the phantom's surface. The implant was a chrome steel ball-bearing with a diameter of 0.79 mm (Grade 25 AISI 52100 chrome steel, Simply Bearings Ltd, UK). Figure 4.1 is a photograph of the experimental set up in which the phantom can be seen. Two phantoms were constructed (figure 4.2). The first was a homogenous block with a height of 4 mm and sides of length 40 mm. The second had equal dimensions and modulus, but contained an inclusion made from stiffer rubber centred above

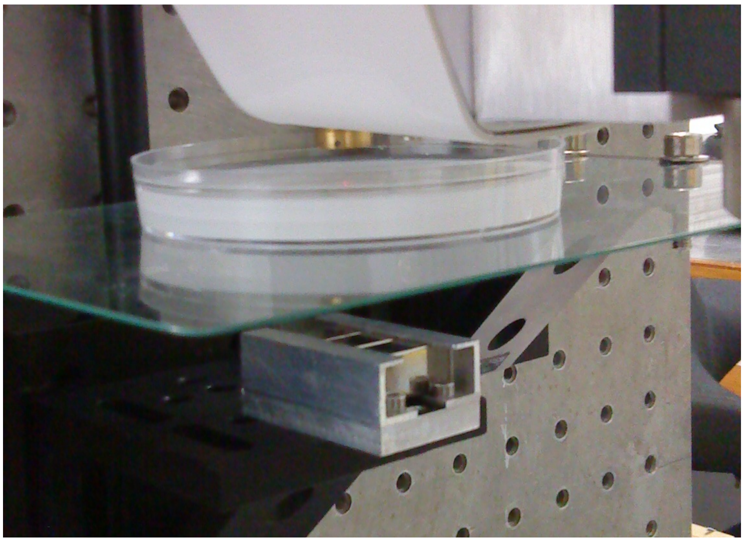

Figure 4.1: Photograph depicting the experimental apparatus in which the phantom is clearly visible between the OCT probe and actuator assembly. The phantom was removed from the petri dish when conducting the experiment to reduce the distance between ball bearing and magnet.

the implant. The inclusion was a disc 0.8 mm in height, with a diameter of 2.0 mm, positioned such that its upper face was flush with the top surface of the phantom. The scattering properties for bulk and inclusion were closely matched, with little variation in optical contrast between the two, as can be seen in figure 4.2(b). The inclusion was securely bonded within the phantom by introducing it to the mould before allowing the surrounding rubber to cure.

The apparent Young's moduli of the phantoms were measured by casting test objects and subjecting them to compression tests (Instron 3342 with 2519-103 load-cell, Instron, UK). For the bulk and inclusion, these were measured as 36.7 ± 7 kPa and 268.5 ± 31 kPa respectively at a compression rate of 2% s^{-1}.

4.2.2 OCT Probe and Actuator

A diagram of the experimental apparatus is shown in figure 4.3. It comprises an OCT system (EX1301, Michelson Diagnostics Ltd, UK) and magnetic actuation assembly. The OCT light source (HSL-2000-10 MDL, Santec Corp.) produces a central wavelength of 1305 ± 15 nm with a 150 nm sweep and a peak power output of 15 mW. Pixel size is 4.3 μm in tissue assuming a bulk refractive index of 1.35. B-scans are obtained at a sample rate of 14.2 MHz and 10 kHz A-scan acquisition. There are four imaging beams, or channels, each with a 0.25 mm depth of focus centred at adjacent axial positions. These are combined in to a single image with

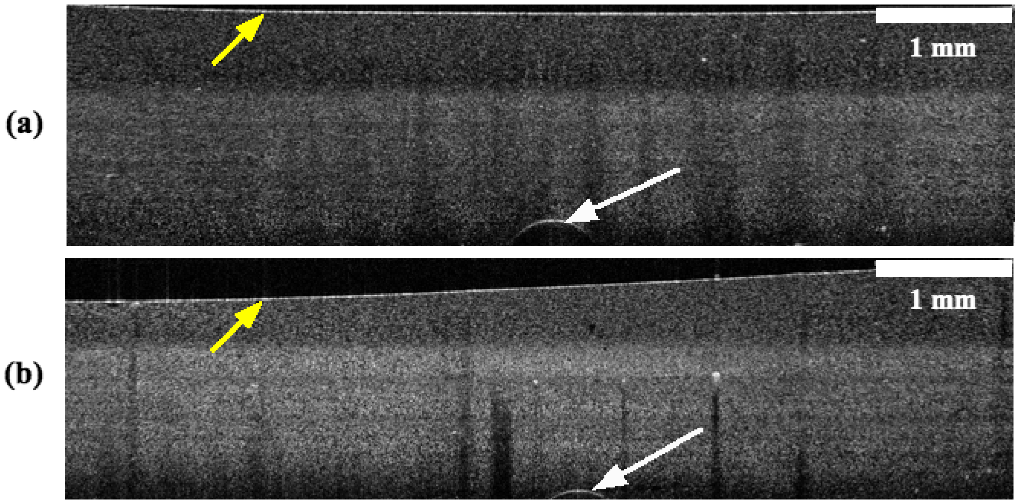

Figure 4.2: OCT images of the control and inclusion phantoms (a & b respectively). In both images, the upper surface of each phantom is visible (indicated by the yellow arrow). The top of the magnetic implant is also visible (white arrow). The stiff inclusion is situated above the implant in (b), but is virtually indistinguishable from its surroundings. Horizontal banding artefacts can be seen at the interface between the four OCT channels.

an effective focal range of 1 mm and a point spread function of 10.9 ± 2. 0 mm axially and 8.9 ± 2.0 mm laterally at FWHM for each channel [67]. Chapter 2 describes OCT system performance in more detail. No smoothing is performed on the OCT signal, although horizontal banding artefacts are generated when the four channels are combined. The operating software offers some control regarding channel blending. This is explored in Chapter 3.

The actuation assembly was constructed from a custom-built three-element Halbach array of neodymium-iron-boron magnets fixed to a vertical translation stage (PT1/M-Z7, Thorlabs Inc.), which applied a known axial force to the magnetisable metal implant embedded within the phantom. The three elements are arranged, so that their combined fields are concentrated along a single face of the Halbach array. This produces a region with a strong magnetic field B and a relatively uniform distribution parallel to the array's surface. Additionally, the array exhibits a steep perpendicular field gradient. The actuation assembly is arranged underneath the phantom, so that the active face of the Halbach array is aligned with the implant along its central axis. This ensures that the field from the array is aligned along a single axial component, $\partial B_z/\partial z$. In this instance the magnetic force experienced by the implant F_{im} has a single directional component proportional to the gradient and strength of the field B_z, such that $F_{im} \propto \nabla(B_z^2)$. Although there were practical difficulties in positioning the small implant relative to the actuator, any lateral force

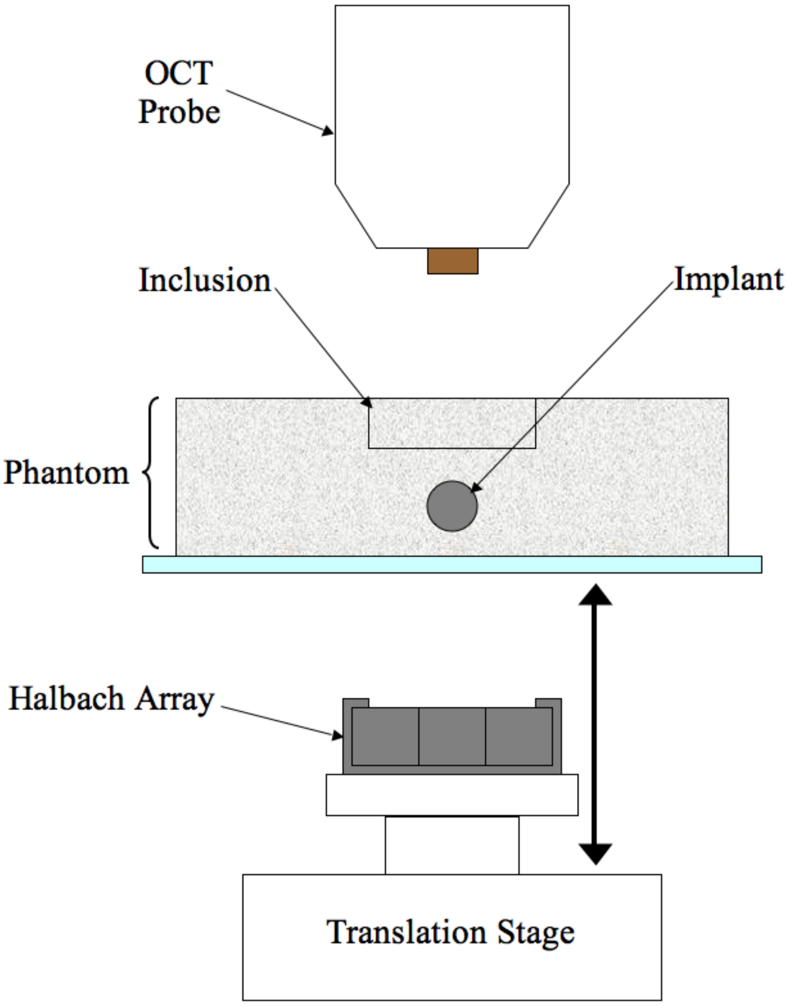

Figure 4.3: Schematic of the OCT probe and magnetic actuation apparatus

components that might have been introduced through misalignment were countered by the Halbach array's uniform lateral field distribution.

The field strength B and gradient $\partial B_z/\partial z$ were measured using a Hall probe as 0.4 T and 67 Tm^{-1} respectively at a distance of 5 mm along the array's central axis (figure 4.4). As the separation between the magnet and implant varied, so the force experienced by the implant changed. This was measured by attaching an implant to a force balance and comparing its weight change relative to the distance from the array. A force-distance profile was compiled in Matlab by plotting the measurements and applying a polynomial interpolation, which can be viewed in figure 4.5. This profile was then used to predict the force exerted on implants in the phantom for particular Halbach array separations encountered during the actual experiment.

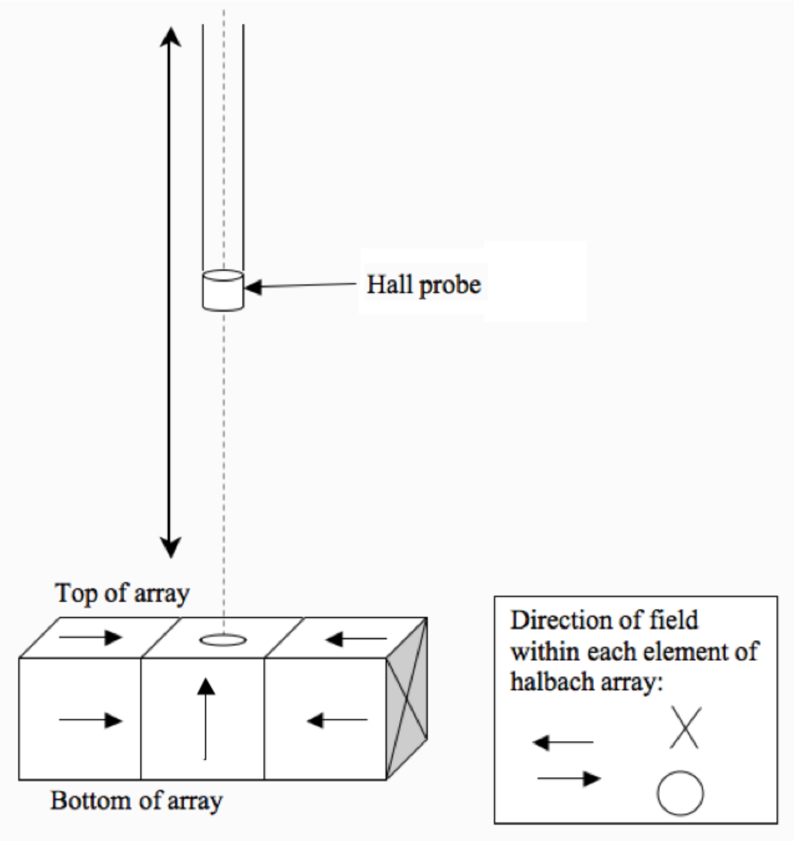

Figure 4.4: The Halbach Array

4.2.3 Finite Element Model

Comsol Multiphysics 3.4 (COMSOL, USA) was used to generate a 2D FE model resembling a cropped, central cross-section through the tissue phantom using the planar strain static analysis module. The cross-section had a 20 mm width, 4 mm

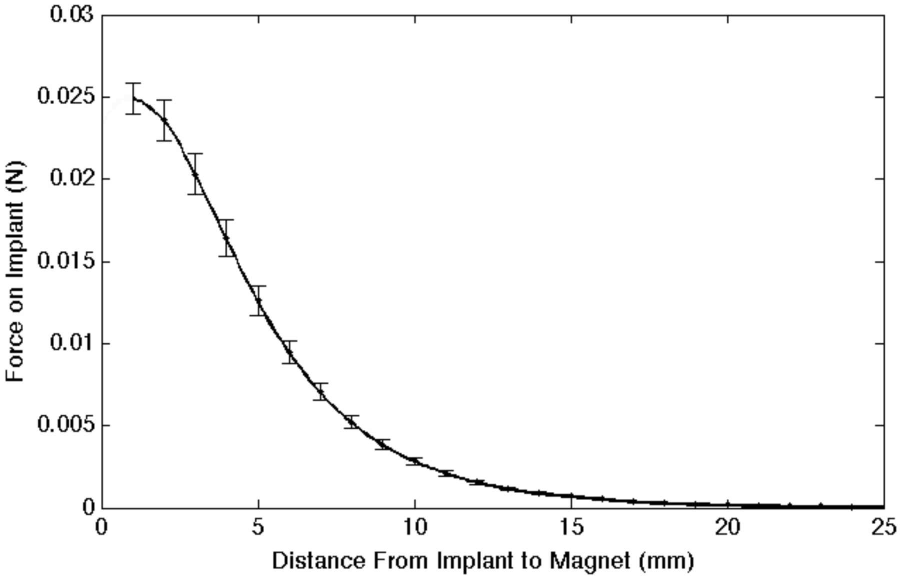

Figure 4.5: Force profile of implant, relative to distance from the Halbach array, obtained using a ninth-order polynomial interpolation across experimental measurements.

height and Young's modulus of 37 kPa with a Poisson's ratio of 0.49, effectively making it an incompressible linear elastic solid. A 2D model of reduced dimensions was adopted because there was insufficient computer memory to simulate the phantom's entire 3D structure at a suitably fine mesh density. The lower boundary supported by assigning it a zero vertical displacement. This still allowed for lateral deformation and free movement of the other external boundaries. The 2D model comprised 2090 mesh points and incorporated a rigid circle with a diameter of 0.79 mm to resemble the magnetisable implant. The circle was assigned the mechanical properties of high-strength alloy steel, as chosen from the default Multiphysics material library. In a second model, a rectangular inclusion (width 2.0 mm, depth 0.8 mm) with Young's modulus of 269 kPa was positioned between the circle and model's upper surface to mimic a stiff inclusion (figure 4.6). Axial forces were applied to the circle, resembling those experienced by the implant, so that it underwent an axial displacement towards the model's lower surface of approximately 23.5 μm.

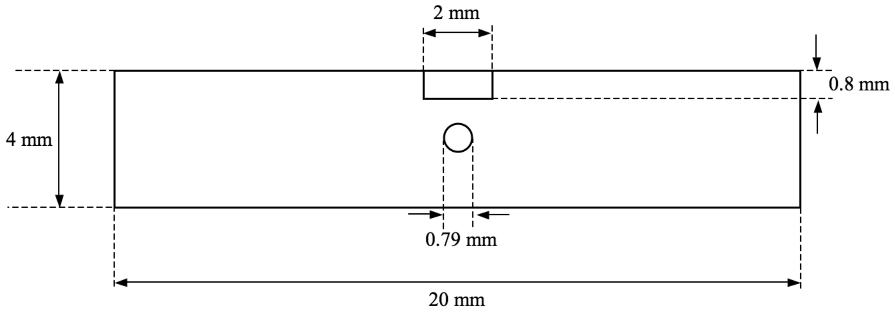

Figure 4.6: Schematic of the phantom's 2D finite-element model incorporating a circle for the spherical implant and a rectangle for the stiff inclusion. The model's width is half that of the real phantom.

4.3 Results

4.3.1 Finite Element Simulations

Displacement

Displacement maps produced from the FE simulations were constructed for an actuation force of 890 μN in both the control and inclusion phantoms (figure 4.7). These illustrate the non-uniform displacement field with respect to the implant's direction of actuation. Figures 4.7(b) and (d) also show that changes in the displacement field are suppressed inside the stiff inclusion as it resists deformation. The displacement maps indicate increased lateral deformation underneath the inclusion, whilst the axial displacement field broadens to incorporate it. The overall result is a quantifiable change in the distribution and magnitude of displacement in the presence of a stiff inhomogeneity. However, due to the field's non-uniform nature, limited contrast between the inclusion and its surroundings can be seen in the displacement data.

Normal Axial Strain

Analysing strain data provides a more useful approach. Figure 4.8 shows the axial normal strain through the centre of both phantoms where its magnitude is greatest. The inclusion causes a change in the surrounding strain field, a step change in the strain occurs at the inclusion boundary and strain outside the inclusion is intensified. These features are useful contrast mechanisms. First, in the presence of an inclusion, strain inside the stiff region is attenuated whilst the field outside intensifies. Second, the sudden change in magnitude at the inclusion's boundary is a means of delineating its geometry. However, contrast is only generated from normal strain in regions where the measured field is of sufficient magnitude. This region is

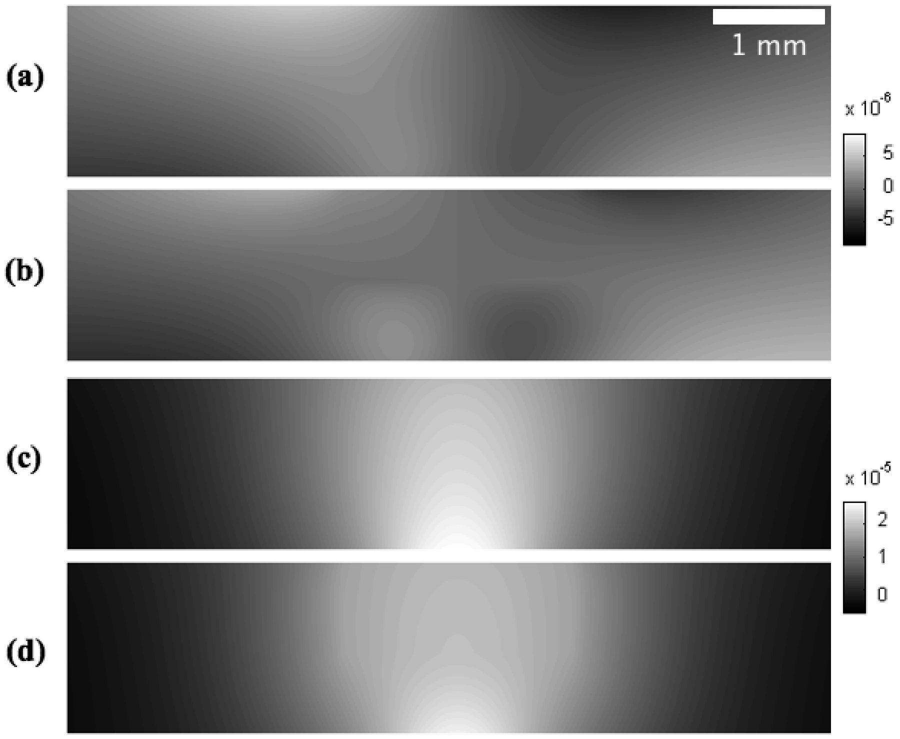

Figure 4.7: FE simulations of the phantoms showing lateral displacement in the control phantom (a) and inclusions phantom (b), as well as axial displacement in the control (c) and inclusion phantoms (d). Note the colour scales in (a) and (b) are much smaller than (c) and (d). Colour bar units are in metres.

confined to a narrow band directly above the implant which is much smaller than the overall width of the inclusion. Outside of this area, normal strain falls off rapidly producing insufficient contrast. In the presence of noise, such limitations would be compounded.

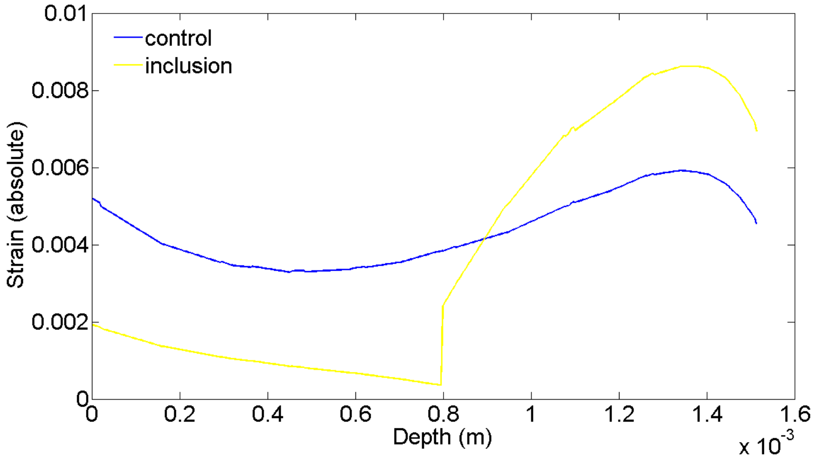

Figure 4.8: Axial normal strain through the centres of both control and inclusion phantoms. The inclusion boundary can be seen at 0.8 mm depth.

Total Shear Strain

Calculating the magnitude of total shear strain from its two components (axial shear and lateral shear) provides contrast over a wider area. As can be seen from figure 4.9, sufficient contrast is generated to distinguish the 2 mm inclusion despite producing a strain field with an inherent null zone at its centre. The null zone arises where phantom deformation is primarily in the direction of motion of the implant. This results in a large normal strain component, but little or no shear.

4.3.2 Experimental Results

Displacement

The actuation force exerted on the implant was measured to be 890 ± 40 μN. Displacement maps of both lateral and axial components of motion were constructed using normalised cross-correlation and these are shown in figure 4.10. It can be seen from the images that noise is present in the data, as are horizontal banding artefacts arising from the channel boundaries. Despite this, there is still general agreement between experimental and simulated data. A region of high noise is visible along the top left-hand side in the inclusion phantom images, which was the result of

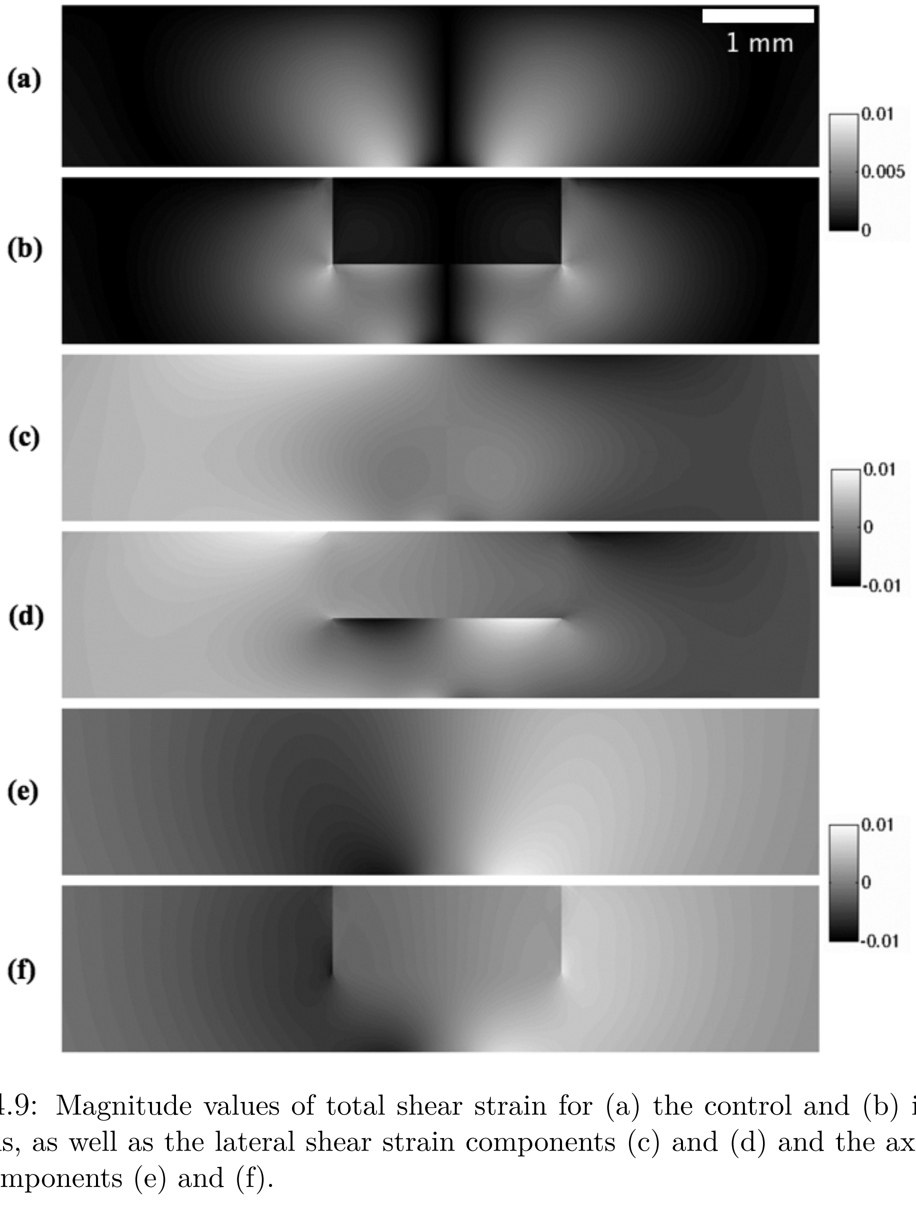

Figure 4.9: Magnitude values of total shear strain for (a) the control and (b) inclusion phantoms, as well as the lateral shear strain components (c) and (d) and the axial shear strain components (e) and (f).

decorrelation arising from a lack of scatterers outside of the phantom (as can be seen in figure 4.2(b)).

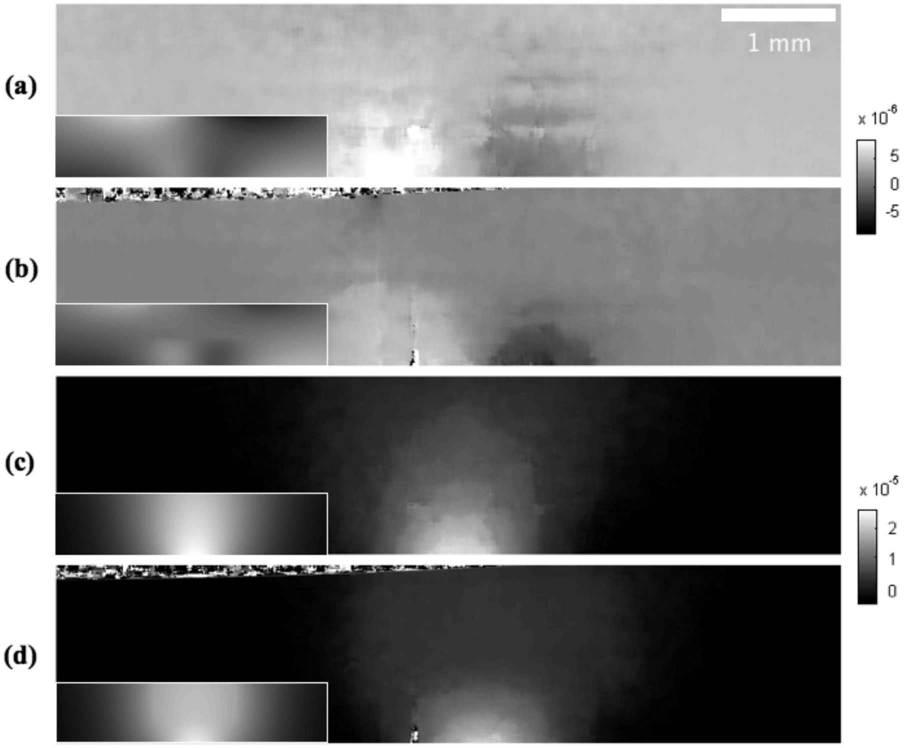

Figure 4.10: Displacement maps produced using normalised cross-correlation for lateral components of motion in the control phantom (a) and inclusion phantom (b), and for axial components in the control (c) and inclusion (d) phantoms. Inset pictures are the corresponding simulations previously shown in figure 4.7. Colour bar units are metres.

Normal Axial Strain

Estimations of axial normal strain are plotted in figure 4.11. As with those shown for the simulation data (figure 4.8), these were calculated using the LSQSE method. Banding artefacts and noise make it impossible to identify the inclusion boundary.

Total Shear Strain

The poor signal for normal strain makes it increasingly desirable to produce useful images from shear strain (figure 4.12). By depicting the magnitude of total shear strain, it is possible to form an elastogram in which the previously invisible inclusion can now be distinguished. Its boundaries are visible in figure 4.12(b), with the exception on the central region where there is not enough shear to generate contrast.

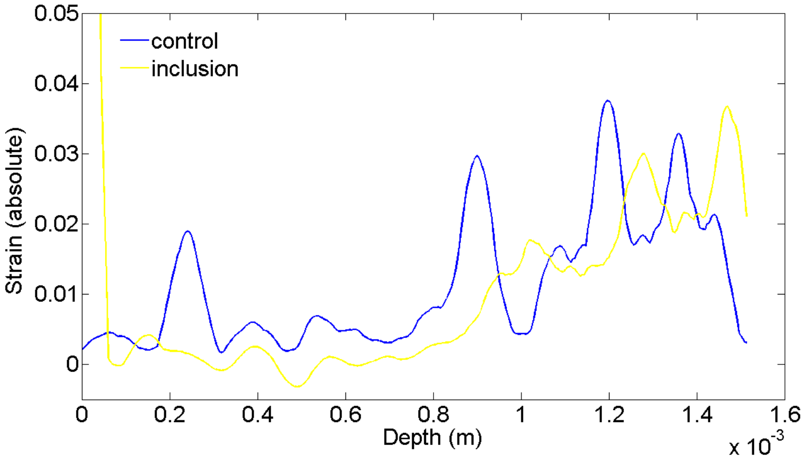

Figure 4.11: Axial normal strain estimations through the centre of both control and inclusion phantoms. The inclusion boundary is at 0.8 mm depth.

Horizontal banding artefacts also appear to obscure the strain distribution, especially in figures 4.12(c) and (d). These two elastograms were formed from lateral displacement data where the artefacts are again caused by the seams between each OCT channel in the original images (figure 4.2).

4.3.3 Strain Ratios

To further clarify the technique's performance, the ratio between average and total shear strain and a background reading was plotted. This was achieved by considering the total shear strain elastograms and measuring their mean background in a 50 × 50 pixel region situated in an area of low strain. Next, the mean strain for every A-line between a depth of 0.215 mm and 0.645 mm (a distance of 50 pixels) was recorded. The ratio between each A-line's mean value and the background measurement was calculated for control and inclusion phantoms using experimental FE data. The results are plotted in figure 4.13. Figure 4.13(d) illustrates the inclusion's effect on the strain ratio. As would be expected, the experimental data exhibit a large noise component compared to FE simulations, resulting in smaller peaks at the inclusion boundary. In the experimental data, the inclusion was located slightly off-centre, which accounts for any misalignment with the simulated results.

Strain ratios were also produced for a vertical band bisecting the inclusion and passing through a region of high shear. This time, instead of taking mean A-line values, the average strain along each row of pixels within the band was recorded. These results are shown in figure 4.14. The peaks in strain ratio in figure 4.14(b) and especially 4.14(d) are the result of decorrelation and banding artefacts. The artefacts

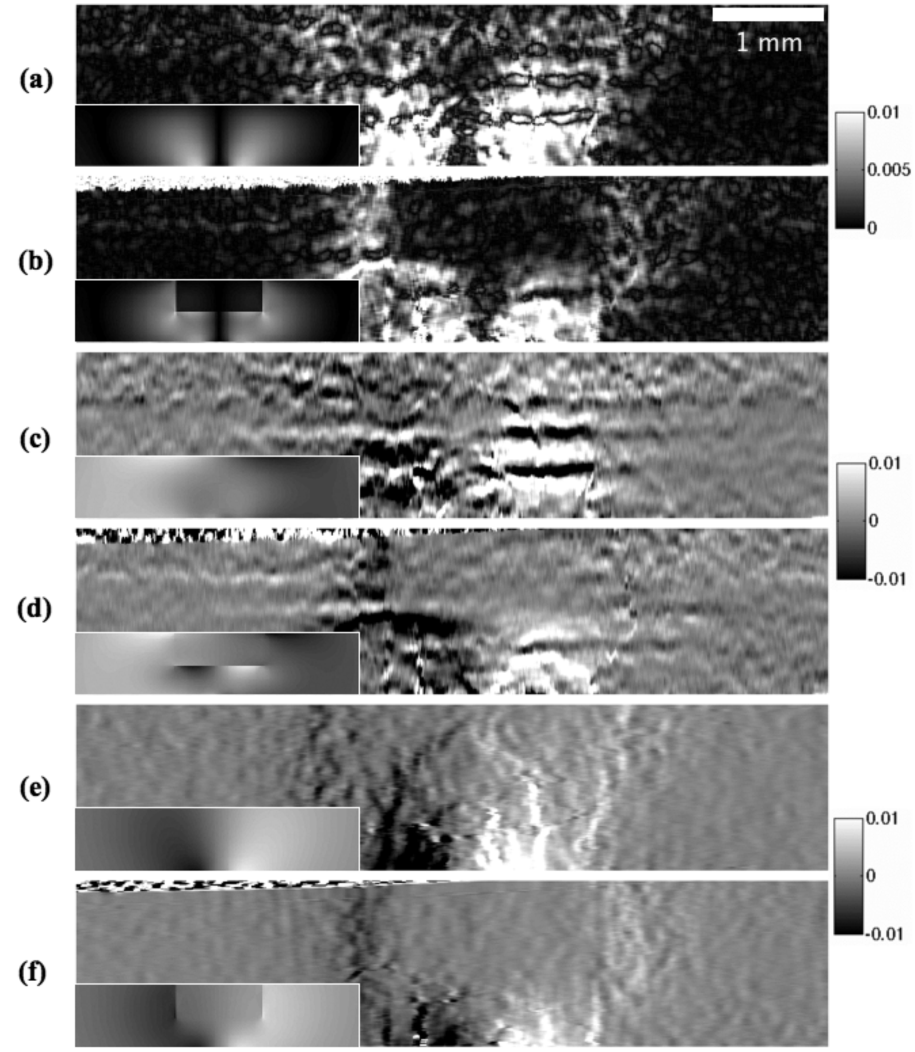

Figure 4.12: Magnitudes of the total shear strain estimations in (a) the control phantom and (b) the inclusion phantom, along with the lateral shear strain components (c) and (d) and axial shear strain components (e) and (f). Inset pictures show the corresponding simulations. Banding artefacts can be clearly seen in the lateral shear elastograms.

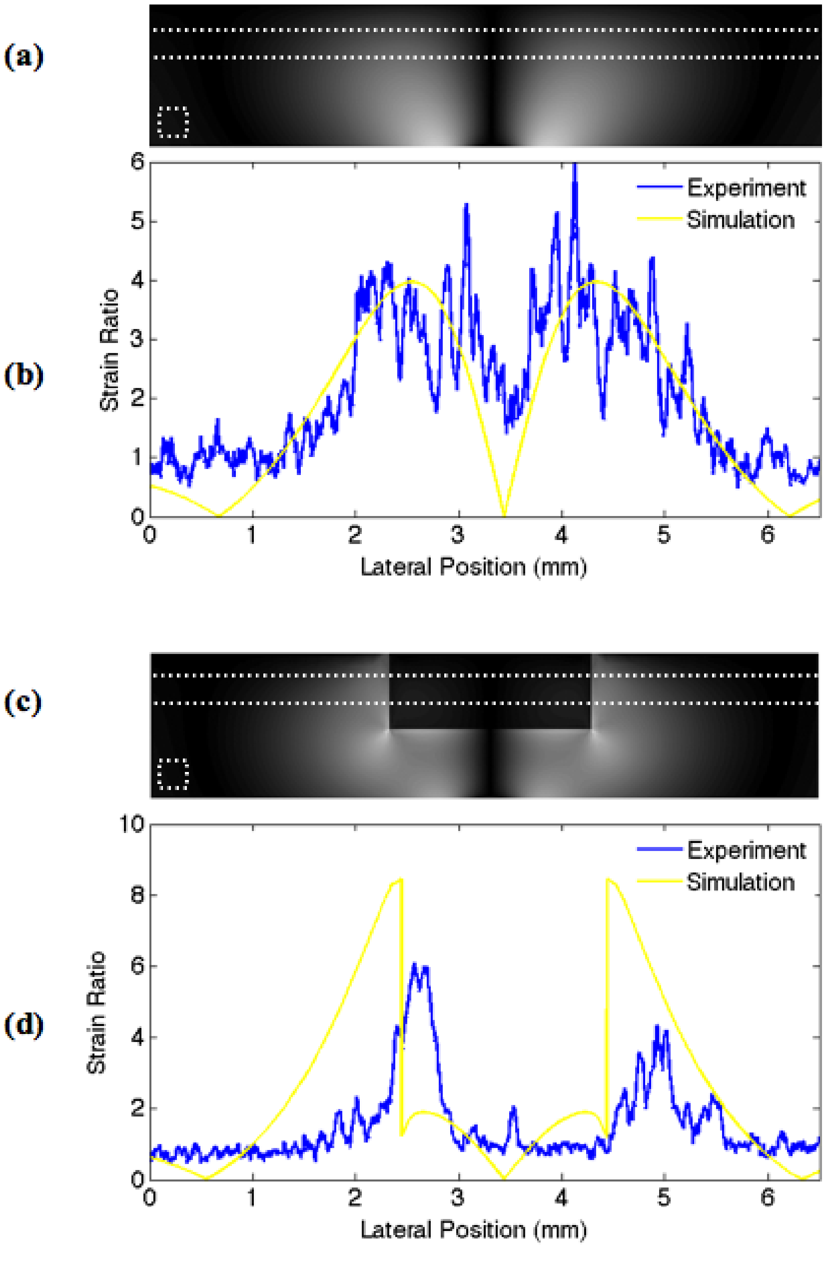

Figure 4.13: The images (a) and (c) illustrate the square regions of interest used to calculate the mean background value and show the horizontal band within which mean A-line values were recorded. Plots of the shear strain ratio across (b) the control and (d) inclusion phantoms are depicted for both experimental data and FEM simulations.

may also account for the undulating, low frequency variations in the signal, which can clearly be seen in figure 4.14(b) at the inclusion boundary.

4.3.4 Improving Performance

Separate Channel Processing

The horizontal banding artefacts previously mentioned occur in displacement and strain maps derived from mosaic OCT images. Banding can be reduced if the signal from each channel used to produce the OCT image undergoes NCC tracking separately. As there are four channels, this will result in four sets of displacement and strain data. These are horizontally cropped and stacked to produce a mosaiced map analogous to the original image. Channel cropping and mosaic construction is illustrated in figure 4.15 and an elastogram comprising the four separately processed strain maps is shown in figure 4.16. The strain map constructed from separate channels reduces the effects of banding significantly, although discontinuities can still be seen across channel boundaries.

Combining Shear and Normal Strains

A further potential improvement is the utilisation of both shear and normal strain components. By averaging all components together, a global strain magnitude can be presented. This new strain distribution counteracts the central null zone observed in total shear elastograms. Figure 4.16b shows such an elastogram, however it is clear from this image that correlation artefacts have been compounded (radial bands emanating from the elastogram's lower edge) and to be truly useful, improved signal to noise/reduced artefact generation is required.

4.3.5 Imaging Tissue

In a final demonstration, an implant was embedded into a chicken breast and the experiment repeated. Chicken has speckle characteristics closer to those of human skin, as can be seen in the PDFs and OCT images in figure 4.17. Testing the actuation and NCC tracking methods in an animal model provided a way of verifying how effectively both techniques could be applied in-vivo.

The implant was introduced into the chicken by attaching it to a thread, which was then passed through the flesh using a needle. The ball bearing was positioned just below the tissue surface with the thread left in-situ. Unlike the phantom experiment, uncertainty over the implant's exact position made it impossible to know

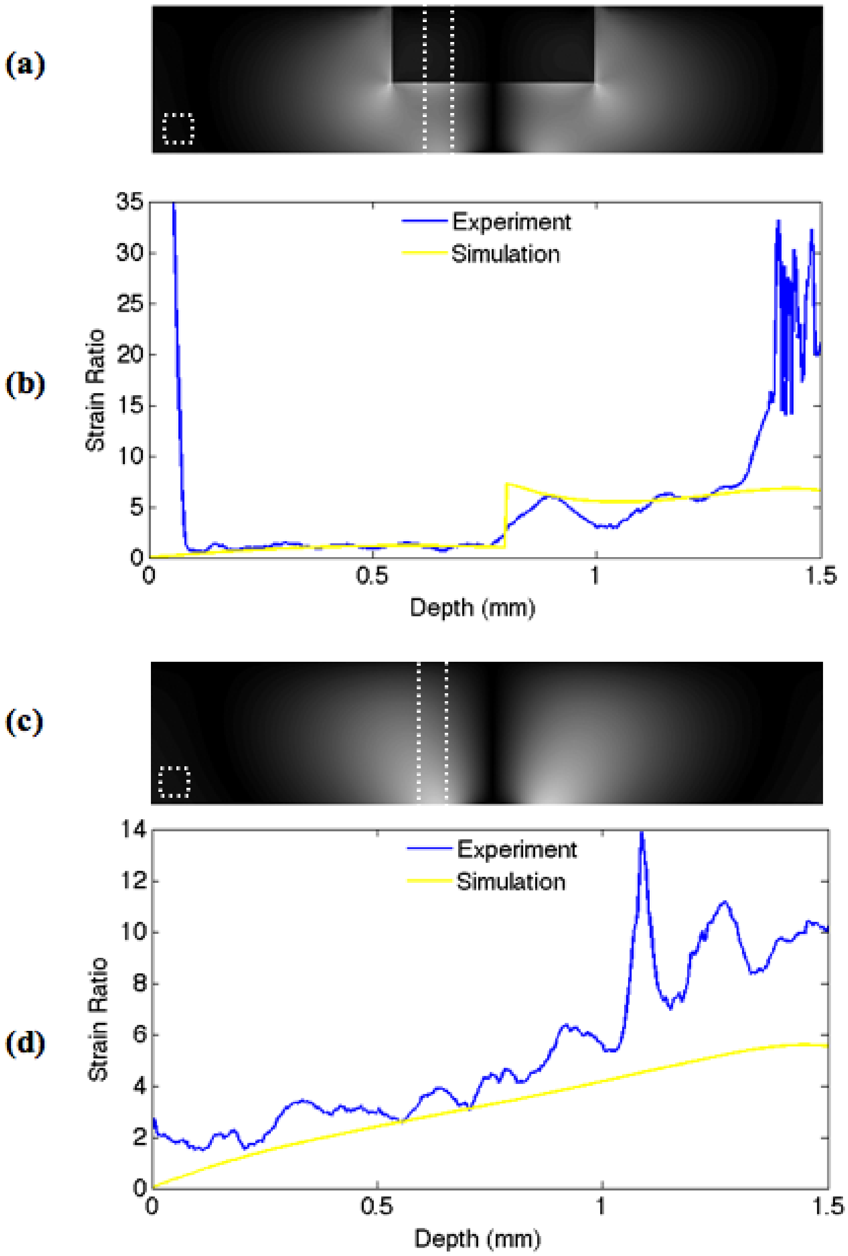

Figure 4.14: Images (a) and (c) illustrate the band in which mean strain values for each row of pixels were recorded. Graphs (b) and (d) show the change in the strain ratio with depth for control and inclusion phantoms, respectively. The inclusion boundary in (b) is at 0.8 mm.

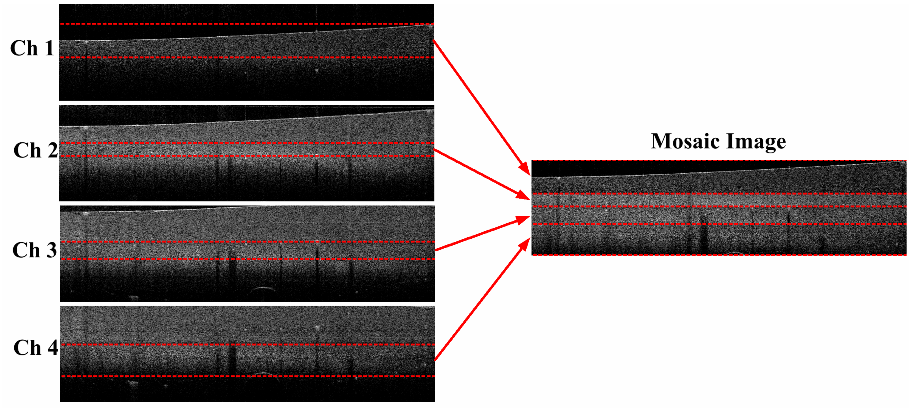

Figure 4.15: OCT images from each of the four channels (left), with the regions utilised in the final OCT image bounded by dashed red lines. The final OCT image (right) constructed by concatenating the cropped parts from each channel to form a mosaic.

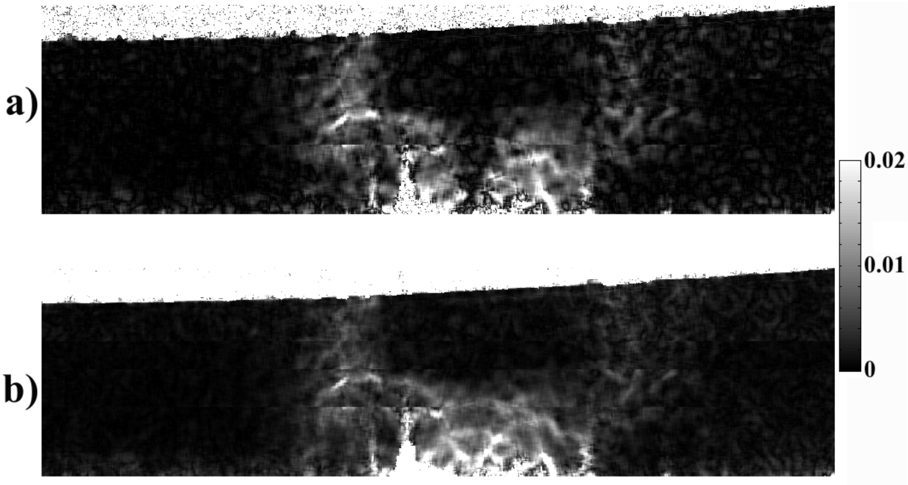

Figure 4.16: The final total shear strain elastogram a), comparable to figure 4.12b. The global strain magnitude consisting of the averaged total and axial strain components is shown in b). Both strain maps were constructed from individually processed channels, which were then combined in a similar fashion to the OCT image mosaic.

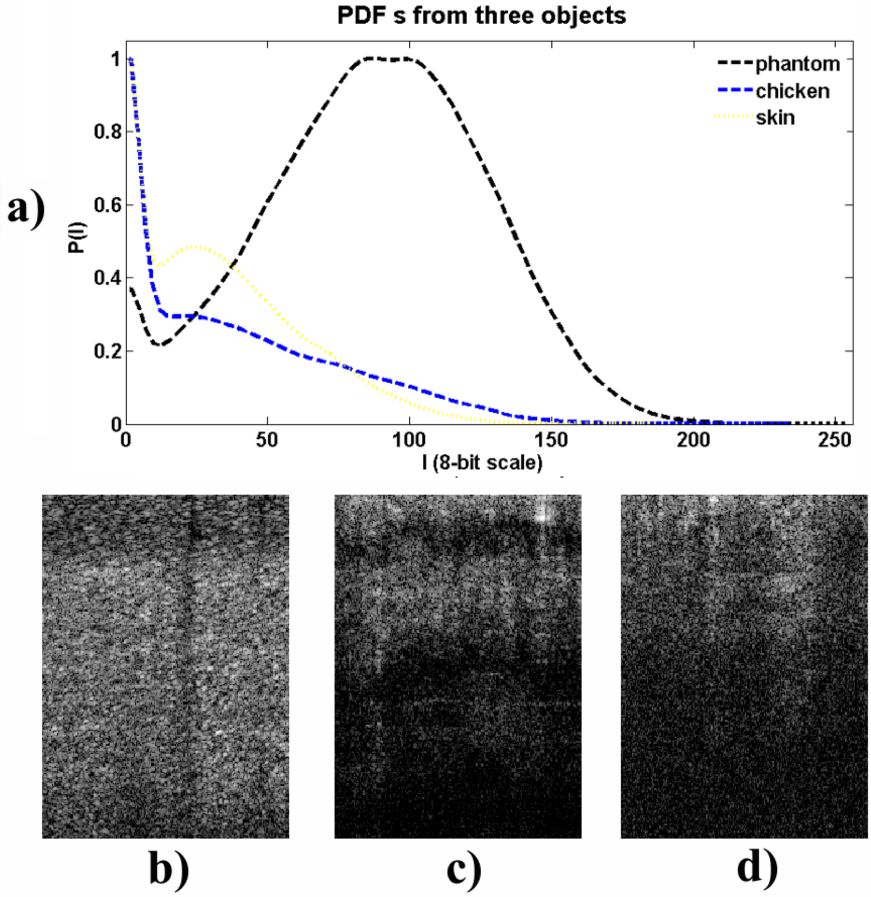

Figure 4.17: Probability density Functions taken from a 275 ×200 pixels region are shown in a) for OCT images of three samples in 8-bit (256 level) format. The samples are: b) silicone phantom, c) chicken breast and d) human skin. There is a marked similarity between the PDFs of chicken and skin compared to the phantom.

its relative location from the Halbach array. This increased the likelihood of out of plane motion, which, with the highly developed speckle pattern, resulted in greater decorrelation rates. A larger kernel size of 30 pixels was used to limit this, however decorrelation was present in large regions of the data (figure 4.18).

Further tracking enhancement techniques were thus employed: an incremental, multi-resolution approach (as outlined in Chapter 3.4.4) was used. Its three tracking cycles had respective kernel sizes of: 40, 35 and 30 pixels; and associated step sizes of: 10, 5 and 1 pixels. This technique produced a sequence of elastograms from the original OCT image sequence, which contained 49 frames taken during magnet translation across its full range of motion (with a magnet translation of 50 μm per frame). Correlations were made between images spaced 15 frames apart to allow for a detectable displacement. The multiple displacement maps were then averaged into a single dataset. The incremental approach was deemed suitable because it reduces decorrelation rates [95]. However, a secondary effect was to amplify jitter. The multi-resolution method limited its influence, resulting in a smoothing of the final displacement data.

The final results are also shown in figure 4.18. In both cases, it is apparent that a large axial normal strain component is generated within the tissue's upper layer. This effect dominates any shear distributions similar to those observed in the phantom and FEM studies. The results from each stage are depicted in more detail in Appendix D.

4.4 Discussion

The implant produced a non-uniform shear field, enabling detection of a stiff inclusion in both phantom and FE models. Here, measuring the magnitude of the total shear strain field proved most effective, despite the appearance of a central null zone. Elastograms were affected by banding artefacts at the interface between OCT channels. The origin of these artefacts is not yet entirely clear. However, a plausible explanation might be the lack of speckle correlation across channel boundaries. The channels have staggered focal regions and separate beams, leading to differences in their phase, such that speckle is uncorrelated between channels [104]. The sudden shift in speckle geometry produces speckles with very sharp edges, cut off at the channel boundary. This would result in enhanced jitter artefacts, following a similar principle to that described in chapter 3. This processes reduces the image tracking algorithm's effectiveness, leading to horizontal banding in displacement data, which is accentuated by the LSQSE. A channel blending utility can be used to smooth the

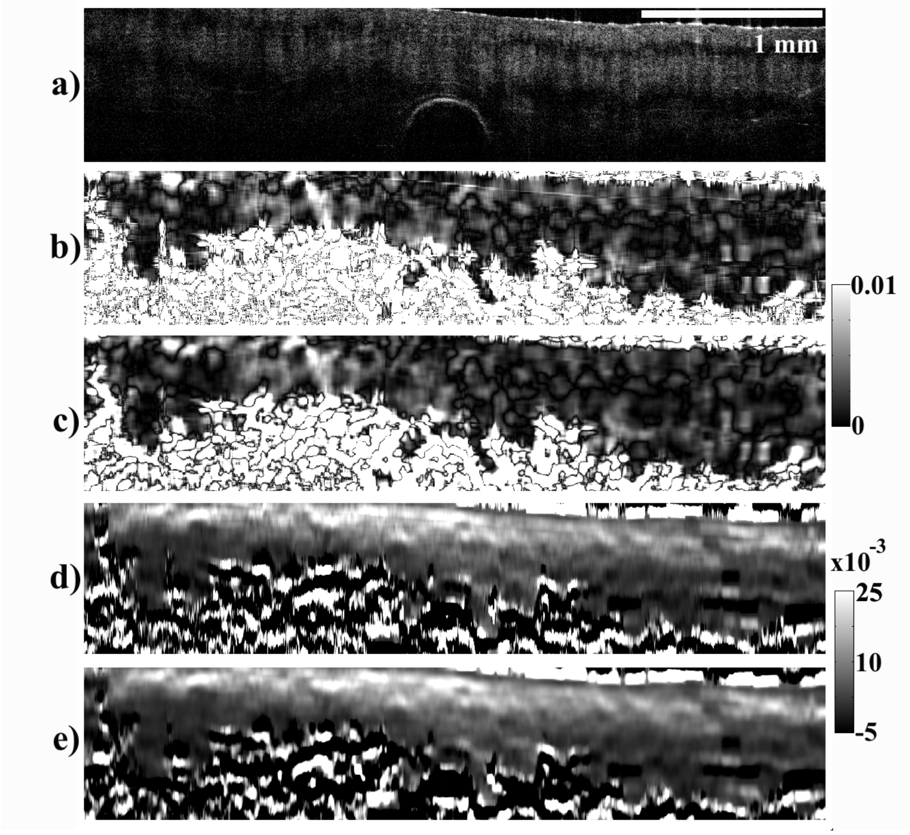

Figure 4.18: a) OCT image of the chicken breast, with implant clearly visible bottom centre. b) magnitude of total shear strain using standard tracking, c) magnitude of total shear strain using the combined multi-resolution incremental technique. d) axial normal strain from standard data, e) axial normal strain from the combined data.

transition, but was observed to have a little effect on image tracking performance. Instead, the most effective mitigation technique was tracking motion in each of the four imaging channels separately, before stitching them into a single dataset.

The null zone in shear elastograms was filled by combining data from total shear and axial normal strains. However, this also accentuated correlation artefacts (in this instance, jitter). Further improvements to the tracking process were applied when repeating the experiment on chicken breast. Here, decorrelation rates were higher. An incremental image tracking approach was employed as a countermeasure and combined with a multi-resolution tracking technique (also previously described in Chapter 3). The multi-resolution method was a quality-guided technique employed to reduce the influence of jitter. A quantitative appraisal of these techniques' effectiveness is yet to be carried out. However, some qualitative improvement can be seen from results presented in this chapter.

The phantom model provided a general representation of melanoma in the absence of elastographic data on non-melanoma skin cancers (NMSC). It did not take into account average values of skin's optical properties, stiffness, viscoelasticity, anisotropy or the extremely wide variation linked to age and the measurement technique [105]. Measurements also assumed that the phantom's compressive modulus and finite-element model's tensile modulus were identical.

Results from chicken show normal strain dominates over shear. The cause of this shifting influence was not investigated, but the normal strain distribution does reflect tissue structure in standard OCT images where a horizontal band of fibrous tissue might have acted as a brace against shear stresses. Additionally, the presence of epoxy resin and thread close to the ball bearing could have reduced the localisation of actuation, producing a more distributed strain field. Conversely it cannot be discounted that the strain map is dominated by artefacts arising from the tissue structure rather than presenting a reliable, independent strain signal.

In every experiment, the implant was never perfectly aligned either with the inclusion or Halbach array. The Halbach array was positioned manually and both of these factors increased the likelihood of out-of-plane motion, leading to decorrelation. However, the array's field density at a given depth is relatively uniform across the imaging region and adverse effects were not observed. Despite this, if the technique is to be applied in-vivo, thought must be given as to how the implant and actuator can be positioned relative to the region of interest.

For tissue, increased rates of decorrelation and resultant degradation of sensitivity in strain maps were mitigated using an incremental, multi-resolution approach. Decorrelation is a primary consideration, especially for in vivo imaging where Brownian motion and other movement artefacts (such as the movement of red blood cells in vessels between B-scans) are increasingly predominant. It is desirable that speckle motion unrelated to the implant is kept to a minimum, along with any out-of-plane movement; thus, B-scan rates need to be high enough to correlate the implant's motion but robust to other movement. In the case of blood flow, this is attainable because vasculature typically appears as regions of low signal in the OCT image, meaning vessels will exhibit a low displacement signal owing to decorrelation between frames. Additionally, implant displacement must be small enough so that it does not cause decorrelation itself. A maximum axial displacement between scans was observed to be roughly 7 pixels in phantoms, but < 3 pixels in chicken breast (where decorrelation was widely distributed throughout the data). There is also an upper limit for scan rate dictated by the signal to noise ratio, whereby the displacement between two frames must be sufficiently higher than background noise. This further complicates tissue imaging, where any structures decrease the homogeneity of the overall speckle pattern, making the correlation process increasingly liable to jitter.

It must be noted that contrast generation from highly localised, non-uniform displacements has been the subject of previous research in both ultrasound and OCT communities [106, 107]. However, measuring total shear strain generates better contrast in the presence of shear stresses from a localised displacement.

4.5 Conclusions

A remote elastography method has been used to generate contrast between internal structure in both phantoms and tissue. No contact is made with the region of interest. The goal of this study was to establish the parameters within which OCE can aid diagnosis of skin neoplasms and margining of tumours. Further to this, elastography may also assist in long term monitoring of tissue over the course of a protracted treatment such as photodynamic therapy [108].

In this study, a silicone rubber phantom with a stiff inclusion 2.0 mm × 0.8 mm in size was used to represent a melanoma model. The inclusion was shown to be distinguishable from shear strain elastograms despite not being visible in standard, multichannel OCT images. Finite-element simulations were also in agreement with these experimental results. Strain ratios across the inclusion boundary changed by 6, with a background strain ratio of 2. Research by Hitachi Medical under E. L. Siegel and B. Dasgeb has reported strain ratios in skin of between 5.3 – 32.2 for malignant lesions and 0.01 – 3.0 for benign lesions using high frequency ultrasound

[109, 110].

Elastographic information was obtained in chicken breast, which had a more developed speckle pattern than human skin, this suggests correlation tracking could be applied to OCT images of human skin.

The presence of noise and artefacts reduced elastographic sensitivity. This was partially mitigated in post-processing and further methods for overcoming this issue, including phase tracking, are currently being investigated. Other methods of actuation, such as indentation, or highly localised magnetic nanoparticles could also be adopted to reduce invasiveness and increase sensitivity.

Chapter 5

Phase-sensitive OCT

5.1 Introduction

From the previous chapter it is clear that improvements in displacement sensitivity would enhance the performance of elastographic contrast involving OCT systems like those produced by Michelson Diagnostics. Furthermore, the intrusive nature of deploying an implant close to a suspected tumour site may have implications for patient imaging (although applications in pre-clinical work could be more easily realised). In this chapter, research into phase sensitive imaging is presented. The work was undertaken to investigate potential ways of increasing motion sensitivity through bypassing the imaging artefacts and high speckle decorrelation rates associated with NCC methods in tissue, whilst retaining non-invasive actuation such as surface indentation. A basic description of phase is offered and experimental implementation of both static and dynamic measurements are illustrated. In the case of dynamic phase, a simple indenter was positioned away from the region of interest and used to generate a mechanical actuation in the form of traveling surface shear waves. Static measurements were performed on image sequences of the actuated phantoms from Chapter 4.

Practical considerations are also addressed regarding the use of magneto-motive OCT (MM-OCT) in conjunction with the MDL system. MM-OCT is a contrast generation method currently under development in which magnetic nanoparticles are introduced into a specimen and remotely actuated. This produces a dynamic change in the OCT signal associated with the excited scatterers. The signal modulation can then be used to generate elastographic contrast.

This is the first time phase sensitive OCT is demonstrated using the MDL system. A practical comparison of its performace in relation to NCC tracking is outlined in an experimental model where no discernable structure is visible between mechanically different regions. This complements previous work on phase sensitive OCT where ambiguity remains as to how much of the elastographic signal is intrinsic to the contrast between structures' scattering properties and tehir mechanical differences [96, 111]. More generally, a number of unresolved challenges and limitations regarding phase measurements using OCT still remain unaddressed by previous research, especially in conjunction with MM-OCT [112, 101, 113]. Some of these issues are explored throughout this chapter. They can be categorised into three broad groupings: hardware, signal processing and actuation development. Suggestions for further enhancements are also offered.

5.2 Measuring Static Phase

Analysing OCT phase data has become an established means for detecting motion. In the 1990's it was initially the preserve of tissue Doppler imaging studies, but has recently been applied to areas such as elastography and rheology [114, 115, 102]. The fundamental principle involves measuring shifts in the complex OCT signal's phase at a specific location. By considering the OCT signal as a complex wave function, its phase is limited between $+\pi$ and $-\pi$ spanning the interference signal's coherence length. Using these assumptions for a sample exhibiting a strong reflection signal with no speckle, such as a mirrored or glass surface, the phase is relatively uniform between adjacent A-lines. However, the following experimental results show the assumption of a uniformly flat surface generating a uniform phase distribution is too simple.

System optics affect the relative optical path length of the imaging beam as it is laterally scanned, especially if the OCT system traces a fan beam across an imaged sample [116]. For a high NA system, the result is a curved depth of focus distribution, which is deeper along the lens axis and shallower off axis. Such a distribution was not visible in experimental PSF measurements detailed in Chapter 2, something unsurprising considering the MDL system uses a telecentric lens to equalise path length changes as the beam is laterally swept. The phase measurements described here, however, demonstrate that optical path length measurements of a flat surface do vary laterally across the B-scan. This is indicative of an undefined, but consistent variation in system optics across the OCT's lateral scanning profile. Furthermore, additional artefacts have been observed, especially in bulk phase shifts between A-scans. Although not definitively proved, these variations reinforce the suggestion that the OCT system's optical configuration may not always be consistent between

A-lines. This has already been observed in other systems, but the exact cause was, again, unproven [117]. Despite these challenges, sensitivity to small actuations is still demonstrated and normal axial strain maps from phantoms are compared with NCC image tracking data. The results are proof of phase imaging's increased sensitivity compared to speckle tracking when imaging axial displacements. However, the techniques employed here limit phase shift measurements to just one axis. As such, strain estimations are confined to axial normal strain.

5.2.1 Theory

Optical coherence tomography is a low coherence interferometric imaging modality. All experimental work within the thesis was carried out using a swept-source, Fourier domain system. As such, the A-line signal is constructed from a wavelength-dependent interference signal $S(\omega)$. To generate standard OCT images, a complex signal is formed from the Fourier transform of $S(\omega)$ and its magnitude is taken, which results in a real, depth-encoded signal $I(y)$ (where wave number is analogous to depth). This is repeated for a series of laterally separated A-lines, thus forming a single B-scan $I(x, z)$. The image signal can be simplistically represented as [96]:

$$I(x, z) = FT(S(x, \omega)) = |A(x, z) \exp -i\phi(x, z)| \tag{5.1}$$

where the magnitude of $FT(S(x, \omega))$ is used to generate the usual OCT A-line intensity profile. The phase term $\phi(x, z)$ is bound between $\pm\pi$ and is ostensibly random over this range. However, for a specific location containing detectable scatterers, any phase shift $(\Delta\phi(x, y))$ between two measurements is linearly related to axial scatterer displacement, $d(x, z)$ when the phase change is smaller than $\pm\pi$:

$$\Delta\phi(x, z) = 2nkd(x, z) \tag{5.2}$$

where n is the specimen's bulk refractive index and k is wavenumber [96]. Calculating displacement from a phase shift in tissue requires an associated value for refractive index, n (the MDL system sets an approximation of 1.35). By rearranging equation 5.2 and substituting for k, displacement $d(x, z)$ can be expressed as [115]:

$$d(x, z) = \frac{\Delta\phi(x, z)\lambda_0}{4\pi n} \tag{5.3}$$

Measurements of $\Delta\phi$ can be calculated for the same location between consecutive B-scans, or for a location within adjacent A-scans, providing the lateral spatial sampling is dense enough to reduce phase shifts arising from intrinsic scatterer structure. When measuring axial height changes of the optically flat surface, $\Delta\phi$ was measured between the first A-line and the A-line of interest:

$$\Delta\phi(x_n, z) = \phi(x_n) - \phi(x_0, z) n = 0, 1, 2... \tag{5.4}$$

The MDL system itself has a theoretical coherence length l_c in free space of approximately 2.5 μm, as calculated using the following equation [55]:

$$l_c = 0.44 \frac{\lambda_0^2}{\Delta\lambda} \tag{5.5}$$

This distance equates to the length over which phase is bound between $\pm\pi$, where λ_0 is the source central frequency and $\Delta\lambda$ its bandwidth, both quoted by the manufacturer as 1305 nm and 300 nm respectively.

5.2.2 Method

Measurements were taken of an uncoated mirror blank (Thorlabs UK Ltd., PF05-03) with an optical flatness of 10% the beam wavelength (less than 140 nm). The mirror blank was placed on a two-axis rotation stage so that its angle relative to the horizontal could be altered both within the imaging plane and normal to it. All measurements were taken with a normal angle of 5°, tilting the surface out of plane to reduce saturation at the detector. Image data was recorded for a series of surface angles relative to the horizontal image axis by changing the stage's angle of rotation within the image plane. Phase profiles were extracted by processing the complex Fourier transformed interference pattern and horizontally unwrapping its phase at the surface's signal peak. A smoothing spline fit was then applied to the surface phase profile at 0° and the resultant curve was used as a correction function for measurements at all angles. After correction, the mean profile gradient was calculated and compared with the actual surface gradient.

Static measurements of phase shifts between B-scans were taken for a tissue phantom undergoing a localised actuation (described in in chapter 4). Here, the phase shift between two adjacent images in a sequence was extracted to produce a fringe pattern (the result of phase values bound by the system source coherence length). A series of post-processing steps was carried out to reduce random phase noise and smooth the data. The phase map was bound between $+\pi$ and $-\pi$. It was unwrapped vertically (i.e. for each A-line) using Matlab's *unwrap* function and rescaled to depict the displacement. Next, axial normal strain was estimated from these displacement maps using LSQSE. The process was repeated for each channel and a final mosaic image constructed from the data. These results are displayed with NCC elastograms for the same image sequence. Strain estimation and mosaicing are described in Chapters 3 & 4.

Post-processing of phase shift maps was necessary to reliably unwrap the data. This was achieved by applying low pass Butterworth and median filters before sampling phase. The post-processing technique (depicted in figure 5.1) was based upon Doppler imaging methods [118, 115], closely following steps previously described by Steven. G. Adie et al. [119].

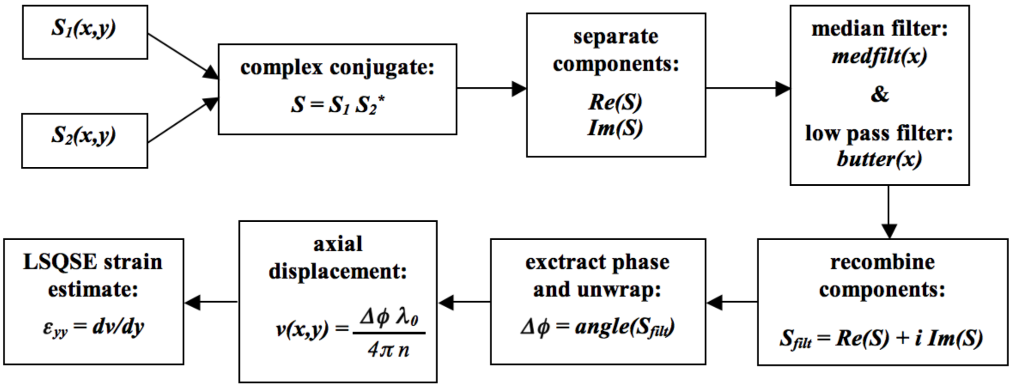

Figure 5.1: Processing stages undertaken to produce final axial displacement and strain maps derived from phase shifts between B-scans (S_1 & S_2).

5.2.3 Results

The first experimental results depict an OCT intensity image of a flat surface and its associated phase after lateral unwrapping (figure 5.2). Both data sets were axially interpolated before plotting phase along a fixed depth coinciding with the primary phase distribution. It is evident from these plots that the flat surface generates a curved phase profile and remains correlated over a large axial span. For a simple arrangement such as this, a straightforward rectification of the curve artefact was attempted by applying a smoothing spline fit to the phase data and then subtracting one from the other. To test how accurate this method was, the spline fit from a flat surface was subtracted from image data of angled surfaces. The results can be seen in figure 5.3. For the first 200 lateral sample points, the correction produces a good straight line approximation, however the angled surfaces' corrected profiles gradually become non-linear. Unwrapping errors generated by phase noise would have a compound effect as transverse position increases, furthermore; if the original flat surface was not correctly positioned at exactly 0°, the corrected angle profiles would exhibit a gentle curve. Both of these effects would explain the divergence from a straight line of the corrected profiles after roughly 1 mm.

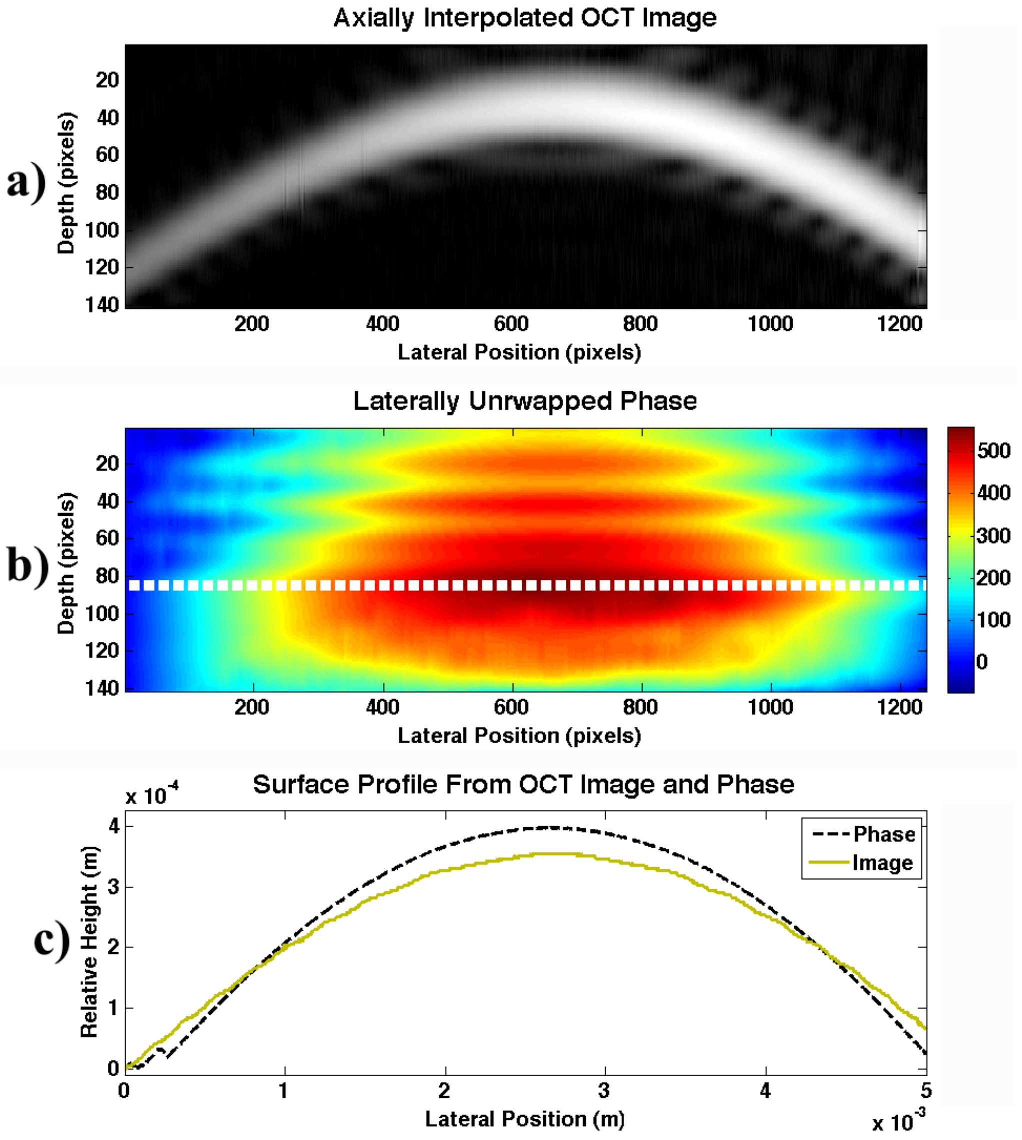

Figure 5.2: Axially interpolated OCT image signal across a flat surface a). Phase profile derived from the OCT complex signal b), which was unwrapped laterally using Matlab's *unwrap* function before interpolation (units in radians) and surface height profiles in c) measured from both phase and intensity data.

Next, phase was measured for B-scans of a tissue phantom. Distributed scattering centres produce an ostensibly random phase map, however, the source was stable enough for changes to be measured between adjacent B-scans. By recording these phase shifts, a fringe pattern was formed, bound between $\pm\pi$. Post-processing reduced noise enabling the production of an axial displacement map from which normal strain was estimated. This is displayed in figure 5.4 along with images at

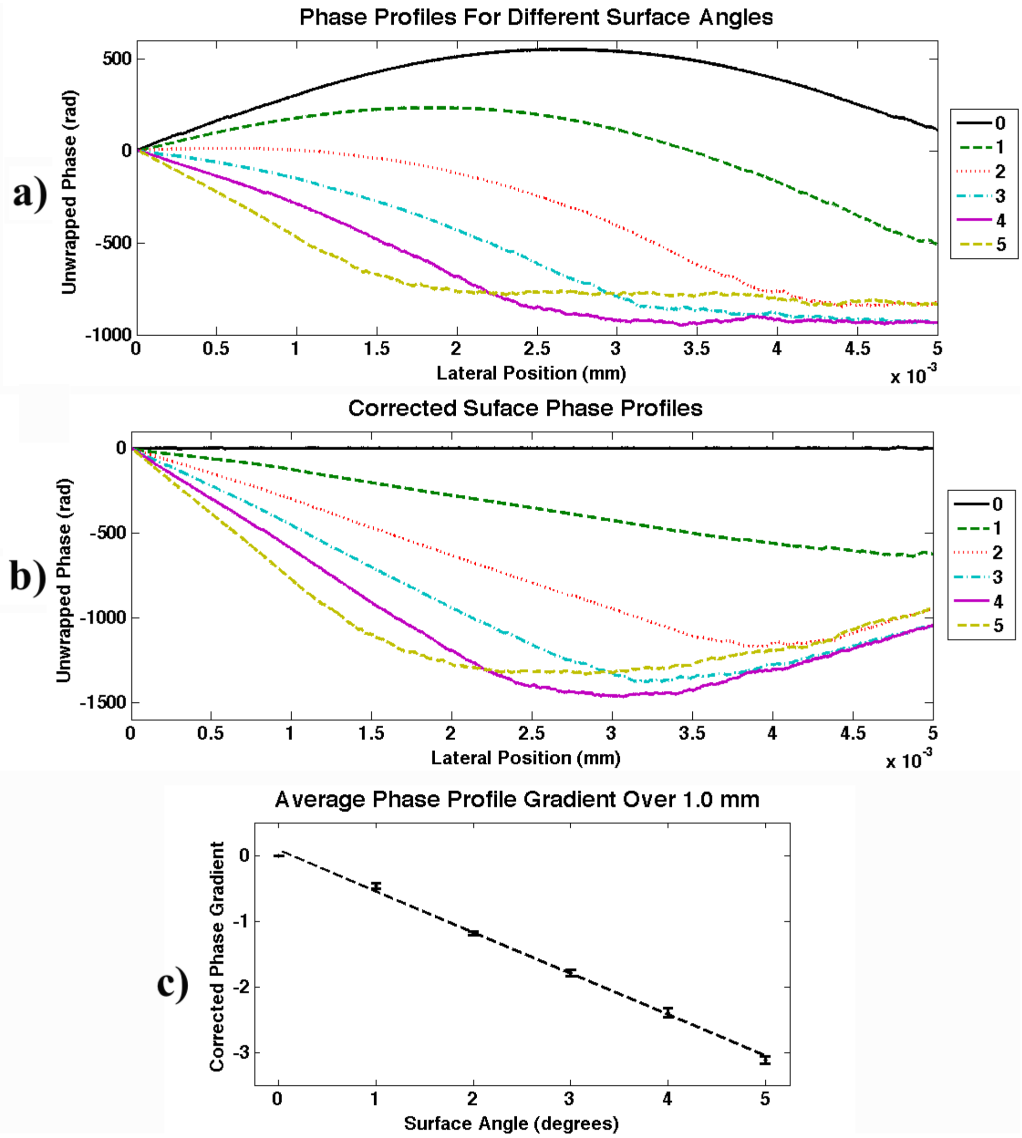

Figure 5.3: Surface phase profiles a) Measured as previously described for a number of surface angles (0–5 degrees) relative to the OCT image's horizontal axis. b) The same phase profiles after correction by subtracting a spline fit of the 0 degree profile. c) Mean corrected profile gradients across the first 1 mm with error bars equivalent to two standard deviations.

some of the processing stages. A ramp mask was employed to cover regions with a SNR below 3.

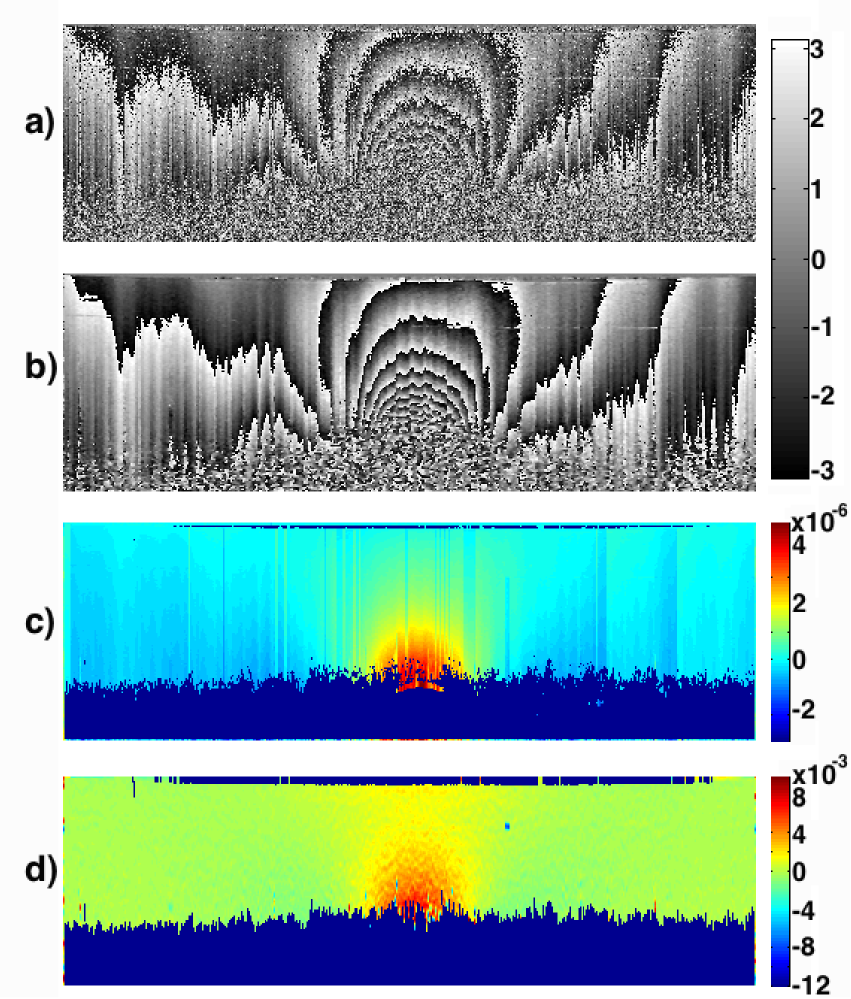

Figure 5.4: For a single OCT channel image sequence depicting an implant actuation: a) unprocessed data showing the phase in shift in radians between B-scans, b) post-processed phase shift map, c) axial displacement map (scaled in metres) similar to that displayed in figure 4.10, d) absolute axial normal strain map derived using LSQSE.

Strain maps are displayed below in figure 5.5, for data derived using both phase and NCC tracking. Strain ratios along a horizontal band 50 pixels thick and coincident with the stiff inclusion (where present) are plotted to demonstrate phase tracking's superior sensitivity. Strain ratio was calculated using the same method described in Chapter 4. Finally, the time taken to generate an elastogram from a single OCT channel was timed in each instance to compare the time cost of both methods. The phase tracking method took 751±16 seconds compared to 2150±38 seconds for NCC tracking; a distinct performance advantage.

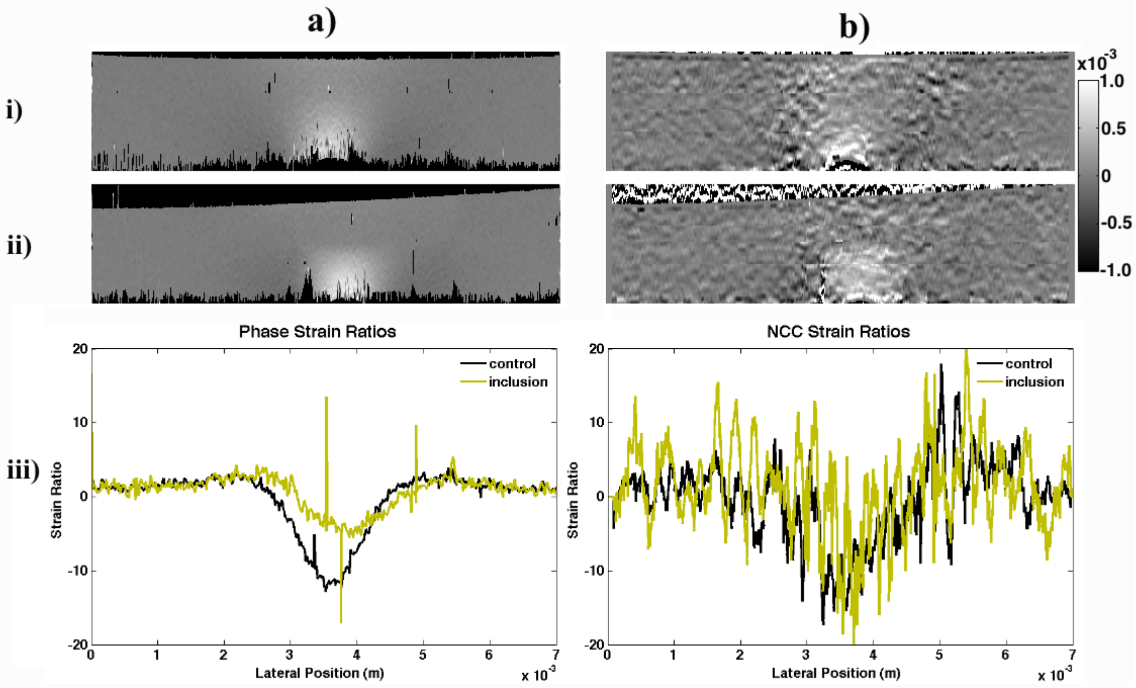

Figure 5.5: Strain estimations derived from a) phase data and b) NCC tracking. The control phantom is shown in i), inclusion phantom in ii) and mean strain ratio for a horizontal band passing through the inclusion's location in iii). The colorscale depicts absolute strain and the maximum implant displacement was approximately 1.5 pixels.

5.2.4 Discussion

For the optically flat surface, displacements between A-lines as small as 50 nm ±50 nm were measured from phase data after correcting for optical distortions at an angle of 1° to the horizontal image plane. The large errors can be seen clearly in figure 5.6 as discrete spikes. Actual displacement at this angle is 70 nm between A-lines and the 20 nm difference from experimental measurement is a likely result of human error when positioning the manually operated translation stage. This advances a suggestion that the correction function was not obtained from a perfectly horizontal surface, which would leave subsequently corrected profiles with a slight curve. A study by Dr Steve Matcher, at MDL, in collaboration with the University of Sheffield has concluded that these spikes in phase data arise from an asynchrony in the source sweep and data acquisition [120]. In future, distortion effects could be reduced by using a test object across a range of depths (i.e. axially translating a flat surface and measuring its phase profile at multiple heights). Alternatively, a correction function for the entire B-scan might be calculated from information on the system optics. This could be derived from placing a flat reference object across the OCT image and deriving a 2D correction function for the rest of the B-scan from its phase profile. The fact that spikes in the phase profile manifest in an unpredictable manner makes this a desirable option. However, imaging such a test object at the same time as the intended specimen requires careful positioning and consideration of the object's optical properties. Particularly, it must generate a strong imaging signal without degrading that of the target.

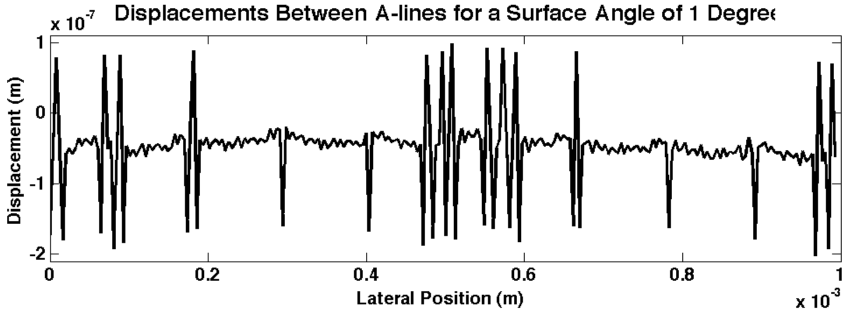

Figure 5.6: Displacement at the optical flat's surface between adjacent A-lines, as measured for a surface angle of 1° from the horizontal.

When imaged, an optically flat surface appeared curved. For a surface normal to the beam axis, the geometry of this curvature depends upon lens optics and the galvanometer sweep profile; both of which were unknown. Thus instead of modeling a geometric correction function, the optical surface was positioned normal to the beam axis and a fitted spline was extracted from the resulting phase profile. This spline was then used as the correction function. Similar correction methods for the related problem of shifting depth of focus have been applied successfully to en-face images [116]. Scanning a flat surface and correcting for the curve effect enabled a measurement of phase sensitivity of 50 nm.

Phase shifts between B-scans were measured across an image sequence depicting an elastography phantom undergoing actuation via an implant as described in the previous chapter. Elastograms of axial normal strain were constructed from this data and proved superior to results obtained using NCC methods, both in terms of sensitivity and computing power.

The phase shift maps displayed an apparently arbitrary modulation in mean phase change in entire A-lines similar to the spikes observed in figure 5.6. These manifested as crenelations in the phase fringe pattern and vertical jumps in the displacement data. Their source is unknown, but two mechanisms with the potential for causing them are: errant vibrations transmitted to the experimental apparatus from other equipment within the laboratory; or variation in the system optics, such as synchronisation between triggering and acquisition of the OCT's swept source, or sudden shifts in the optical path length between detector and lens. Out of these, source synchronisation seems an increasingly likely cause, because the phase shifts do not exhibit periodic behaviour and because vibration damping features were incorporated into the experimental apparatus. Furthermore, the source's performance specifications (Santec Corp., HSL-2000-11 MDL) give a variation in centre wavelength of ±15 nm. If this is a dynamic variation exhibited within B-scans it may account for the artefacts. Bulk shifts in phase between A-lines have been observed by others and corrected for using a mean subtraction method, however such a technique cannot work in a scenario where a non-uniform strain field is being imaged [117].

Further compounding this issue in phase tracking is the presence of uncorrelated noise. Such noise was effectively removed through post-processing, although the combination of noise and unwrapping artefacts noticeably influence the final displacement data. Despite this, axial normal strain elastograms still exhibit a high degree of sensitivity and compare favourably with those obtained using NCC tracking when analysing small (less than a few pixels) displacements.

Lateral normal and shear strain components cannot be measured using the phase imaging technique as described here. This is an impediment to generating a simple contrast map between background strain and the stiff inclusion, because each strain component generates a non-uniform distribution containing only partial information on the mechanical boundary between inclusion and bulk – hence the desire to combine axial and lateral stress components (stated in Chapter 4). As a result, this method would be better applied to elastographic imaging of planar axial stress. In future, bulk phase shifts may be corrected by using an optically flat reference object positioned across the OCT field of view, but thin enough to enable simultaneous imaging of a sample. Subtracting its phase profile from each row of B-scan data may remove curvature aberrations and spikes in phase that are uniform along entire A-lines.

After observing the limitations of imaging axial normal strain, another elastographic method was proposed whereby phase shifts between adjacent A-lines were measured instead of adjacent B-scans. Such a method is more akin to Doppler measurement techniques and can monopolise on the sensitivity of phase measurements, whilst mitigating the effects of artefacts. This potentially more sensitive method requires an actuation across A-lines, and is thus referred to as a dynamic process – rather than the static process of imaging displacements before and after applying an actuation. Most importantly, it has the potential to generate images based on the local elastic properties of tissue without needing to analyse multiple strain components.

5.3 Dynamic Phase Measurement

Vibration measurements have been used in both ultrasound and OCT as a means of generating elastographic contrast [119, 121]. In OCT, the method employs phase measurement techniques similar to those already described, but this time tracking shifts between adjacent A-lines rather than adjacent B-scans. The technique requires measurement of axial displacements from a controlled mechanical excitation. The actuation can come from a variety of sources, such as a mechanical linkage or even magnetically actuated nanoparticles dispersed within the sample [101, 112]. The fundamental principles of such a method were investigated to ascertain whether the technique could be implemented using the MDL system. System performance in the dynamic regime was tested in terms of both displacement and frequency sensitivity on porcine skin. Phase data was processed in much the same way as previously described to measure shifts between adjacent A-lines.

5.3.1 Method

Dynamic measurements were conducted across a range of A-line spacings from 0.5μm to the default 4μm. Porcine skin was imaged at these sampling densities whilst simultaneously applying a vibration to the specimen's surface using an indenter constructed from a needle coupled to a speaker cone. The set up could be used to generate periodic displacements across a range of frequencies and amplitudes below the system coherence length. Phase data was processed in a similar fashion to that previously described for static phase imaging. However, a number or modifications were made: first, a band pass filter, customised to the vibration frequency, was included. The pass band spanned 4% of the lateral phase spectrum and its centre frequency was automatically selected for via a peak detection algorithm that could identify the vibration frequency. This same peak detection method was also used to condition the low pass filter so that its pass band was at 5% above the vibration frequency.

Phase shifts were recorded close to the focal region for a single channel to guarantee high SNR. This data was then averaged to produce a single lateral profile, which was Fourier transformed to produce a frequency spectrum. To verify the method's capacity for detecting different amplitudes and frequencies over a range of A-line densities, a series of basic measurements was undertaken for each of these parameters.

In the experiment, it was assumed that the indenter actuation generated a planar shear wave across the OCT B-scan. Using the phase tracking technique described, it was possible to measure axial displacement between adjacent A-lines arising from the shear wave's propagation. The MDL system has an A-line acquisition rate, f_s of 10 kHz and the Nyquist criteria dictates what maximum excitation frequency, f_b, can be reliably measured before aliasing occurs:

$$f_s > 2f_b \tag{5.6}$$

For a phase shift of $\Delta\phi(x, z)$, the lateral dimension is coupled to time via sampling frequency f_s. By Fourier transforming the phase shift map along its lateral plane (i.e. parallel to wave propagation), a spectrum can be formed with characteristic peaks depicting excitation frequency and shift amplitude:

$$P(v, z) = |FT\left[\Delta\phi(x, z)\right]| \tag{5.7}$$

Lateral spatial resolution of the wave forms recorded in the phase map is limited by spatial sampling and driving frequency f_b. Additionally, the spectral lateral resolution is also dictated by the span over which the Fourier transform is implemented. For this series of experiments, the Fourier transform encompasses the entire B-scan's width and is comprised of depth-averaged data; thus it does not convey information relative to spatial location.

5.3.2 Results

A-line Spacing

Different lateral sampling densities were used to acquire images of a 120 Hz vibration at constant amplitude. For phase tracking between A-lines to be effective, the structural phase component must vary little between lines relative to the mechanical excitation signal. This is best achieved using M-mode imaging, where one location is repeatedly scanned, however, such a method provides no lateral resolution. Thus, B-scans were imaged to indicate if different lateral sampling densities could practically be used in tissue. The results are shown in figure 5.7, where solid dark blue regions indicate the presence of a mask coinciding with regions where there is low signal to noise.

Vibration Amplitude

Direct measurements of the indenter's amplitude were not conducted. However, the speaker's driving voltage could be varied. As such, measurements of phase

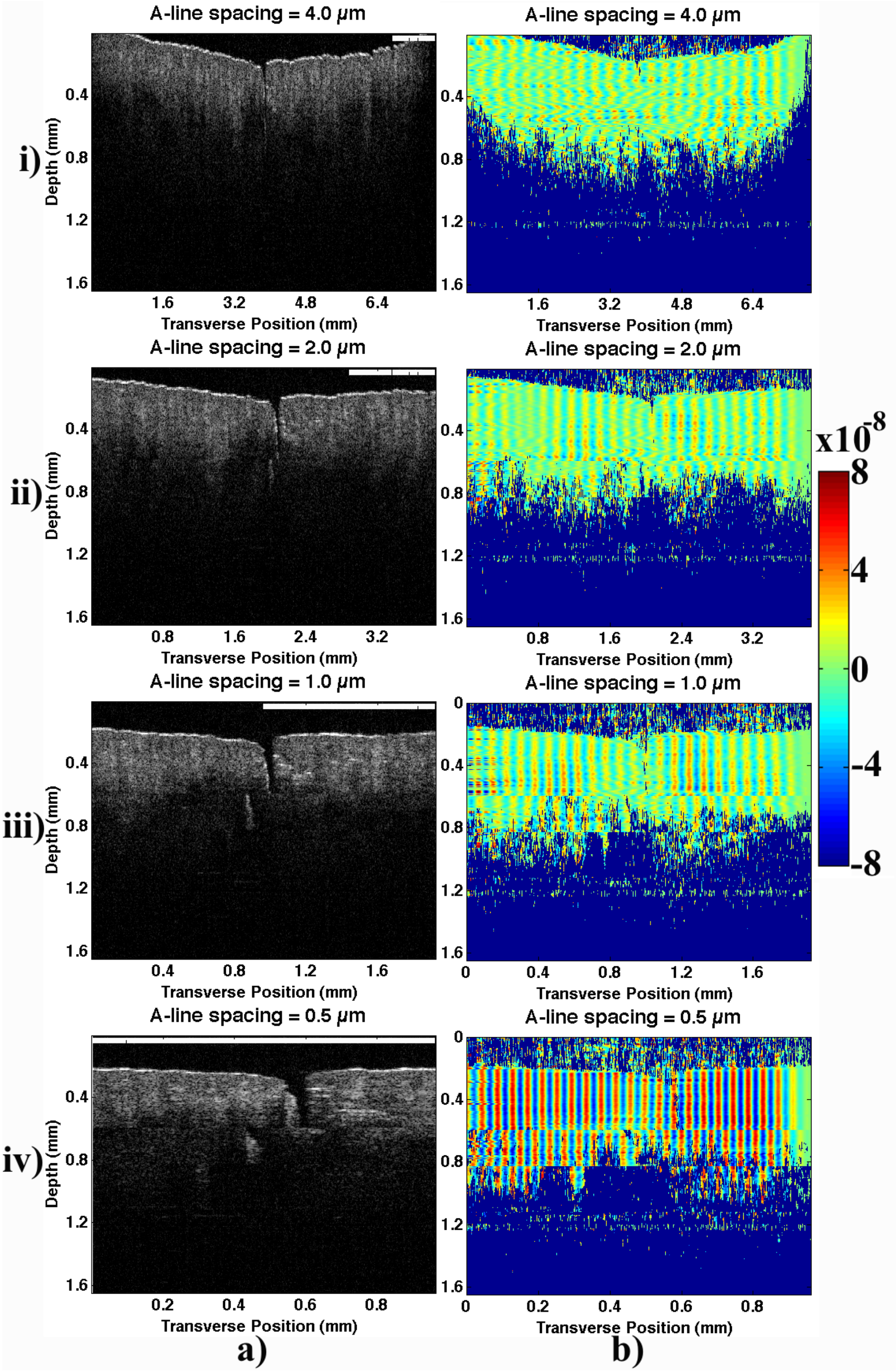

Figure 5.7: OCT images of pork skin a) and their respective phase shift maps b) for A-line spacings of: i) 0.5, ii) 1.0, iii) 2.0 & iv) 4.0 μm. The horizontal white bar in a) indicates 1 mm.

shifts between A-lines were taken relative to different input voltages at an excitation frequency of 400 Hz. The results (figure 5.8) depict a non-linear response with an upward trend mirroring increased indenter amplitudes. However, it could not be demonstrated whether any lack of uniformity was a result of the signal processing, the indenter's potentially non-linear response to voltage or an indication of the tissue's own mechanical response.

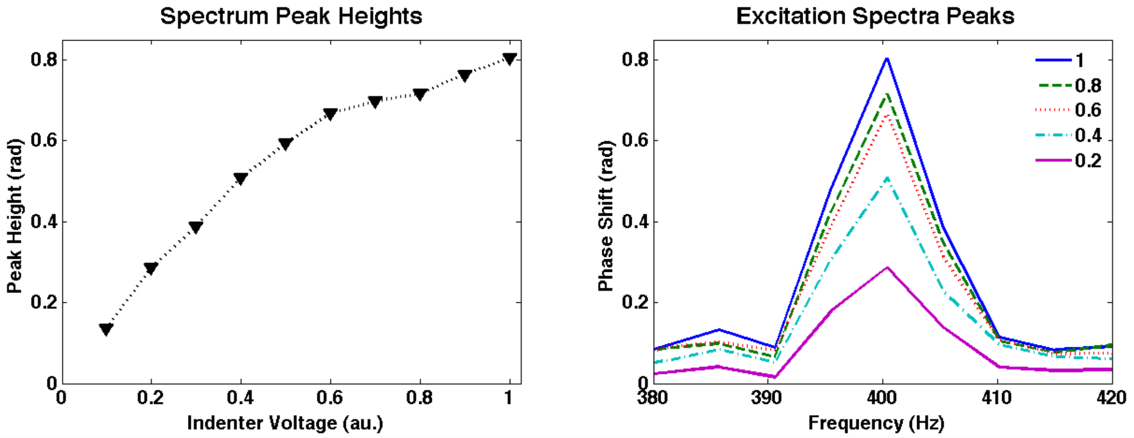

a) **b)**

Figure 5.8: a) Phase shift amplitudes across a range of indenter voltages and b) The excitation peaks in phase shift spectra for some of the measured amplitudes.

Vibration Frequency

Again, direct measurements were not possible, but driving frequencies could be easily specified and were in agreement with resulting phase measurements. Phase shift spectra were acquired from separate images depicting a range of vibration frequencies between 100–1000 Hz at 100 Hz intervals and constant driver voltage. It can be seen from the results (figure 5.9) that there is a downward trend in phase shift amplitude as excitation frequency increases. The cause remains unaccounted for, although it is likely a combination of indenter response and, importantly, tissue mechanical response.

5.3.3 Discussion

This series of experiments has demonstrated the application of phase tracking to Michelson Diagnostics' OCT systems as a means of increasing axial motion sensitivity. It has been shown that the technique is sensitive to changes in driver frequency and amplitude; and that it can be applied to B-mode imaging. Robust phase tracking opens up potential for using OCT to effectively track blood flow and improve

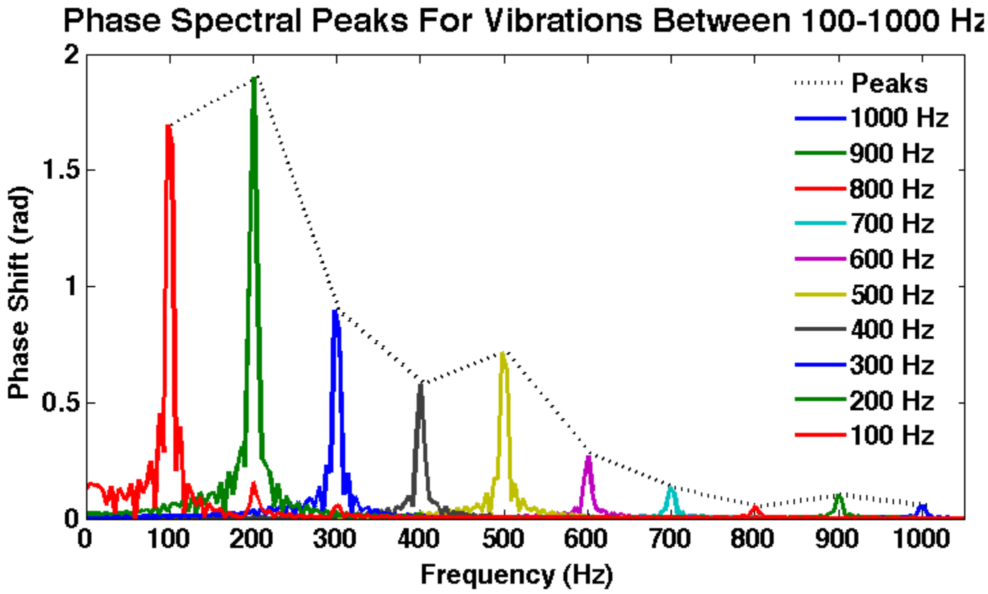

Figure 5.9: Phase shift spectra for a range of indenter frequencies.

visualisation of audio frequency vibrations [122, 114, 119]. The generation of such vibrations can be used a source of elastographic contrast enhancement, analysing the mechanical response of excited tissue or tracking actuated contrast agents.

A number of experimental flaws limited research. If repeated again, improvements would be made so that indenter amplitude and position were known. This would enable comparisons to be made between phase data across a range of sample stiffnesses and excitation amplitudes. Comparisons between different specimens could not be made because the initial position of the indenter relative to the object's surface was never known within any useful degree of accuracy.

Synchronisation of OCT image acquisition with the indenter could also provide elastographic information on a sample's rheological behaviour. This method has already been demonstrated on a number of occasions as a means of probing tissue by scanning its response over a sweep of actuation frequencies [102, 119].

Further refinements could also be made. For example, reductions in noise could be attained by augmenting B-mode and M-mode imaging regimes through acquiring multiple A-lines before stepping the imaging beam to its next lateral position. In this way, noise and speckle changes in the phase shift data would be kept to a minimum whilst retaining the ability to form entire B-scans. However, any increase in B-scan acquisition rates would render an image prone to unwanted subject movements, especially for patient or animal imaging.

An ideal system would track high frequency vibrations, increasing lateral spatial resolution and these would be imaged using dense lateral sampling, both for the same reason and to enhance SNR. Such an OCT configuration would be required to have fast A-line acquisition speeds, whilst the importance of frame rate becomes secondary.

Finally, it is significant that shear wave propagation speeds could not be measured using this technique; the system A-line sampling rate (10 kHz) and spacing (0.5 μm minimum) were inadequate. A similar challenge has been addressed in ultrasound, however, and there is established research into overcoming the issue using a range of methods from system synchronisation to interference wave imaging [14]. On a cautionary note, shear wave speeds in skin vary drastically across measurements as a result of morphology or measurement location. Published data quote a range from 3 ms^{-1} to over 100 ms^{-1} [123, 124].

5.4 Magnetomotive-OCT

The initial goal of the author's PhD research was to generate contrast in OCT from magnetic agents. With this in mind, a section on phase tracking is not complete without a description of magnetomotive-OCT (MM-OCT) and a description of some associated parameters. Measurements of dynamic phase shifts generated from actuating magnetic nanoparticles (MNPs) have already been acquired by others, employing the technique for both elastographic and rheological analysis, as well as contrast enhancement [102, 125]. Notably, the interplay between these two factors (mechanical behaviour and contrast signal) do not appear to have been studied in any great detail, although it is mentioned that the frequency of magnetic actuation must be tuned according to a tissue's observed elastographic response [113].

The MM-OCT system typically described in literature is a high axial resolution (3 μm) FD-OCT with a displacement sensitivity close to 20 nm. This is in contrast to measurements of axial resolution on the MDL system of approximately 10 μm with a phase sensitivity close to 50 nm. Some practical considerations therefore have to be made about the feasibility of using a Michelson Diagnostics system for MM-OCT. These are addressed individually below:

5.4.1 The Contrast Agent

MRI contrast agents such as Ferucarbotran and Ferumoxtran can be adopted as MM-OCT contrast agents. In MRI, these are usually delivered intra-venously via a slow infusion or bolus injection [126]. For such a scenario, typical doses of between 4 μmol Fe/kg and 100 μmol Fe/kg are used. This equates to less than 6 mg Fe/kg body weight. The contrast agent is administered over a period of many hours before imaging and it is extremely likely that nanoparticles will accumulate in different locations within the body. Processing and excretion will also occur because the agent has an associated biological half-life. Furthermore, particle sizes and coating will dictate their distribution, binding and transport throughout the body. All of these mechanisms dictate the effective concentration and mechanical response at a disease site, making MM-OCT a balance between system sensitivity and available contrast signal. Previous literature states MM-OCT has the ability to detect concentrations of MNPs as low as 27 μg/g in tissue and recent work has demonstrated a detectable contrast signal from functionalised MNPs in a rat model at a dose of 150 mg/kg body weight [101, 113]. However, little research could be found on the likely deposition mechanisms and degree of aggregation of particles during the MM-OCT studies, making it difficult to predict how a concentration of MNPs will react under magnetic actuation. Research into magnetic drug delivery has gone some way towards analysing the dynamics of actuated MNPs within the body, indicating a steady progression towards understanding the mechanisms governing transport and deposition at disease sites [127, 128].

5.4.2 Imaging

Forming 2D images using MM-OCT could be executed in two ways: first, a series of laterally-spaced M-mode data can be obtained; alternatively, a densely sampled B-scan can be taken. In the M-mode configuration, lateral spatial resolution is equivalent to the larger of OCT lateral point spread function or A-line spacing. For a B-scan configuration, lateral resolution becomes the apparent wavelength of magnetomotive actuation. This is because at least one period of oscillation is needed to sample the magnetomotive signal.

Previously in this chapter, it was demonstrated that phase data from the MDL system is sensitive to displacements < 6 μm (1.5 pixels) in the static regime and dynamic shifts < 80 nm between A-lines. From these experimental observations, it can be assumed that any dynamic actuation exerted by MNPs in tissue would have to produce phase shifts of a similar magnitude. However, to estimate the resulting actuation amplitude, further information is required.

By considering the phase signal at constant depth along a B-scan (i.e. across a row of pixels), it is reasonable to assume dynamic magnetomotion will produce a periodic signal analogous in form to a sine function $Z(t)$. At the same time, the OCT beam sweeps laterally across the specimen, so that $Z(t)$ is linked to a spatial component $(Z\,(x(t)))$. As long as such an actuation is restricted to axial displacement, it can be expressed as :

$$\begin{aligned} Z\,(x(t)) &= A\,sin\,(\omega t_x) \\ when\ \ vel_x &= 0 \end{aligned} \tag{5.8}$$

Sampling frequency f_s and A-line spacing l_x are significant considerations because they dictate sweep velocity v_s and thus not only the Nyquist criteria, but also spatial resolution. Furthermore, these system specifications are linked to the magnetomotive signal's angular frequency ω, which is itself dictated by the visco-elastic response of tissue. For example, an optimum response of 56 Hz–100 Hz has been quoted for MM-OCT of mammary tumours in a rat model [113]. Consequently, A-line acquisition rates must are dictated by the Nyquist criteria previously set out in equation 5.6, whilst magnetomotive lateral resolution can be adjusted by changing the OCT beam's sweep speed. The interplay between all of these factors must be considered when applying equation 5.8 to a practical situation.

As a demonstration, amplitude of actuation and lateral resolution is calculated for a 50 Hz magnetomotive signal f_m (in Hz, where $\omega = 2\pi f_m$) sampled with an A-line rate of 10 kHz at a spacing of 1 μm. The A-line spacing and sample rate both reflect attainable performance of MDL's Vivosight OCT system.

For a magnetomotive signal, resolution of an OCT B-scan can be described as the imaged wavelength $\lambda_m = v_s/f_m$ (in m, where $v_s = f_s l_x$). Using the values quoted in the previous paragraph gives a lateral resolution of 0.2 mm.

Calculating actuation amplitude A (m) for a maximum shift between adjacent A-lines of 80 nm can be derived from equation 5.8:

$$\begin{aligned}
\frac{d}{dt}Z\left(x(t)\right) &= \omega Acos\left(\omega t\right) \\
\frac{d}{dl_x}Z\left(x(t)\right) &= \frac{\omega Acos\left(\omega t\right)}{f_s} = \Delta z \qquad (5.9) \\
\Delta z_{max} &= \frac{\omega A}{f_s} \\
A &= \frac{\Delta z_{max} f_s}{\omega} \qquad (5.10)
\end{aligned}$$

where Δz_{max} is maximum displacement (m) between adjacent A-lines. For a Δz_{max} of 80 nm, A is calculated to be 2.55 μm. This is below the axial pixel size for a MDL OCT system. For an easily observable magnetic actuation, an amplitude of a few pixels is required. This would entail an amplitude $\approx$ 12 μm, with an associated $\Delta z_{max} = 377$ nm.

5.4.3 Magnetic Actuation

Assuming the MNPs are bound tightly to their surroundings and magnetic actuation occurs at a frequency low enough to treat the medium as a linear elastic solid, displacement $d(z)$ of a given volume V can be expressed as an interpretation of Hooke's law [125]:

$$\Delta l = d(z) = \frac{F}{Ea}l = \frac{\rho F_p V^{\frac{2}{3}}}{E} \qquad (5.11)$$

where, l is axial length through V and a is cross-sectional area, ρ is the number of MNPs per m^3 within V and E the medium's Young's modulus.

Rearranging equation 5.11, force F_p can be calculated for the previously described scenario where $A = d(z) = 2.55$ μm. However, this requires an estimation of MNP number density (ρ) based on the average size and mass of an individual nanoparticle. Assuming iron oxide-based nanoparticles will have a mass density of 5 g/cm^3, close to both magnetite and maghemite,, the force on a single particle in a 1 mm^3 tissue volume of $E = 100$ kPa is illustrated below in figure 5.10 for a range of MNP sizes and concentrations. Dynamic phase measurements are capable of tracking displacements

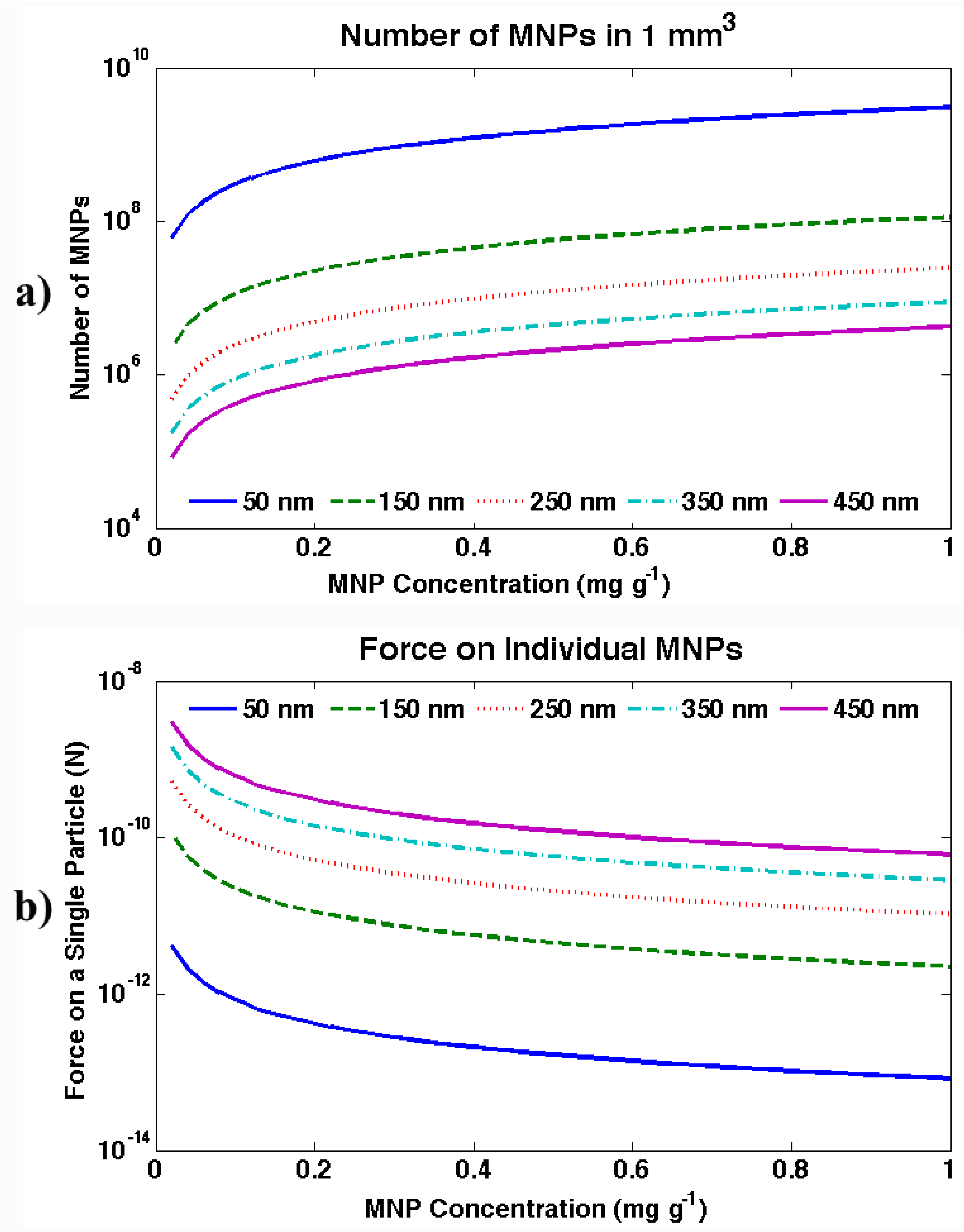

Figure 5.10: The number of MNPs within a 1 mm^3 volume is depicted for a range of concentrations and particle volumes in a). The required force on a single particle to generate a combined actuation of 2.5 μm is shown in b).

along the beam axis. In terms of magnetic actuation, this requires the application of an axial field gradient to generate a force in line with the OCT beam. For a magnetic dipole aligned along the beam axis (m_z):

$$F = (m_z \cdot \nabla)\, B \tag{5.12}$$

Combined with a field gradient, B_z, that varies only along the beam axis, an expression for force on a single magnetic nanoparticle F_p within a medium can be derived as [129, 125]:

$$F_p = \frac{V\,(\chi_p - \chi_{med})\,\nabla|B_z|^2}{2\mu_0} \tag{5.13}$$

where χ_p and χ_{med} are the volumetric susceptibilities of the particle and medium respectively, V is the particle volume and μ_0 the permeability of free space (under the assumption that medium permeability $\mu_{med} \approx \mu_0$). To achieve the kinds of forces indicated in figure 5.10, χ_p must be large enough to facilitate the use of a practical magnetic actuator. Oldenburg et al. have previously described a water-cooled, air core solenoid with a power supply of 250 W. It was capable of generating an 0.08 T axial field strength and gradient of 15 Tm^{-1} within the OCT imaging volume [125, 101]. The MNPs used were quoted as having susceptibilities χ between 2.1 and 4.5.

5.4.4 Discussion

From an extensive literature review, it has been observed that the use of an MDL system for MM-OCT is conditional upon the specification of the MNPs and magnetic actuator employed. Imaging sensitivity of the OCT system regarding MM-OCT has been described. In particular, lateral resolution can be reduced to the lateral imaging PSF by acquiring either a densely-sampled B-scan or by using a sequential M-mode configuration. Providing a sufficient axial displacement is generated by the MNPs, axial resolution should be on a par with other phase sensitive imaging techniques discussed in this chapter (demonstrating a sensitivity of roughly 50 nm). For dynamic MM-OCT, an overall actuation amplitude > 2.55 μm would be required.

Actuation is affected by the MNP's magnetic properties, the tissue's mechanical response and the magnet's field strength (and gradient). Rheological effects on MM-OCT have been studied [102], but in general little has been published yet about the interplay between these key features. Significantly, the force approximations described above are better suited to a linear system under static conditions. This negates any effect from visco-elasticity or from imperfect mechanical linkage between the MNPs and surrounding tissue. A further assumption is that all particles are evenly distributed within a volume experiencing a relatively uniform axial field gradient. Additionally, all MNPs have been treated as superparamagnetic, meaning they have an instantaneous response to any changes in field, which may not be true in other instances.

MM-OCT has been demonstrated successfully in animal models and a range of tissues [113, 125, 130, 101]. In order to progress still further, future studies will have to demonstrate useful contrast generation from MNP concentrations within the prescribed safety limits for humans. Analyses of signal response in relation to variations in tissue mechanical properties, as well as the effects of MNP deposition, binding and tissue selectivity will also have to be conducted. Some of these factors have been addressed in literature concerning the use of MNPs in MRI, magnetic drug delivery and hyperthermia applications [129, 131], but the operating parameters for each discipline are sufficiently different to merit further research into potential MM-OCT agents.

5.5 Discussion & Conclusions

Elastography can be conducted using phase data from MDL systems. This provides an order of magnitude increase in axial displacement sensitivity at the expense of not tracking lateral displacements. Phase measurements can only measure displacements smaller than the system coherence length, making the method prone to decorrelation when imaging living subjects. Measurements between adjacent A-lines rather than B-scans was proposed as a way of increasing sampling rates and thus limiting this decorrelation.

Instability in the OCT phase profile was noted and traced back to source triggering and acquisition. If this effect can be mitigated, the associated improvement to phase displacement maps would enable sampling of axial shear strains in addition to axial normal strain. This would provide extra elastographic detail of the imaged sample.

Optical distortion of the phase profile across the beam's lateral sweep was also recorded, however it appears to have little effect when imaging tissue. Phase measurements require dense A-line spacing, the current MDL hardware is limited to an A-line spacing of 1 μ and an associated B-scan width of 2 mm (8 mm at 4 μm spacing).

Two actuation methods have been explored in this chapter, surface indentation and magnetic actuation of nanoparticles. Surface indentation is simple to implement, but challenges in applying a controlled and pre-defined amplitude were experienced. Similarly, in MM-OCT it is difficult to control the distribution and bonding of magnetic nanoparticles within target tissue. These challenges currently undermine the repeatability of elastographic measurements, but can conceivably be overcome. An indenter calibrated to OCT imaging probe position and future characterisation studies of MNP behaviour in tissue undergoing MM-OCT are potential next steps.

Chapter 6

Summary

A non-invasive imaging technique such as OCE is commercially desirable because it could potentially increase the speed and efficiency with which a tumour is diagnosed and its margin identified. Conversely, current procedures such as Mohs micrographic surgery require an excision biopsy to locate the margin. Repeated biopsies have to be taken in cases where the clinician's previous excision did not incorporate the tumour margin. Patient discomfort and anxiety could be reduced if OCE was able to replace these biopsies, which are, frozen, sectioned and stained before imaging. The speed of diagnosis and treatment would also increase as a result, improving value. The OCE techniques developed over the course of the PhD were envisioned to probe some of the requirements of a future OCE application in skin cancer diagnostics. The current performance of MDL's OCT system was investigated, along with factors affecting displacement tracking and strain estimation sensitivity. This enabled further development of techniques capable of generating mechanical contrast in tissue using both remote actuation and non-invasive sampling methods.

Chapter 2 was a characterisation study of the MDL system, resulting in a measured lateral resolution of 8.5 μm and axial resolution of 12.5 μm at the centre of focus. Both resolution and sensitivity varied across the imaging region. This has potential repercussions for diagnostic imaging with the MDL system. Performance is optimal within a 5 mm region close to the focus, thus any region of interest should be positioned accordingly. Such a precaution was followed in the elastography experiments. Further research into system contrast sensitivity would quantitatively establish the MDL system's response to varying tissue structure. This could potentially lead to better comparisons between standard OCT, OCE and scanning attenuation microscopy [56].

Chapter 3 was a characterisation study of the normalised cross-correlation tracking method. The elastography phantom's optical properties were optimised based upon observations of its speckle pattern and PDF. The tracking method itself was optimised and a lower bound on tracking kernel size established. Displacement data from a range of OCT signals was recorded and compared, enabling the NCC method to be customised to the OCT system. Finally, artefact reduction methods were developed, including single channel image tracking and incremental techniques. These improved tracking sensitivity over small displacements and reduced decorrelation rates. Both techniques enhanced elastographic contrast in the final OCE experiment by mitigating imaging artefatcs.

In Chapter 4, the feasibility of correlation-based OCE to detect a millimetre-sized inclusion with a Young's modulus ratio of 7 is demonstrated, even when the standard image contrast between inclusion and surrounding material is low, providing an indication of the method's potential as a diagnostic aid. Further experiments in Chapter 4 establish the possibility of using OCE in tissue with similar imaging properties to human skin.

Finally, Chapter 5 was an exposition of phase measurements as a possible alternative to the normalised cross-correlation method. The advantage of such a technique was an order of magnitude increase in strain sensitivity along the axial plane. However, such an improvement required the sacrifice of lateral displacement sensitivity. Increased decorrelation rates were also observed, although this was complemented by higher sampling rates, which mitigated the impact of this.

The implant actuation technique detailed in this thesis may not be commercially appealing for standard skin cancer diagnosis, because the placement of an implant increases patient discomfort and the time required for each procedure compared to standard OCT. However, it could prove useful when precise, quantitative and consistently repeatable tissue measurements are required. This may arise where tissue response over the course of a therapeutic treatment such as photoablation therapy is being characterised over many days or weeks. It may also prove useful as a calibration technique when tracking a suspect lesion's properties over time. Surgical precedence for the positioning of millimetre-sized implants as a contrast tool already exists. In some breast cancer patients, millimetre-sized surgical clips are introduced to the primary tumour site using a 17g, 1.473 mm diameter needle, limiting scarring (UltraClip, C. R. Bard Inc., USA). These clips act as a guide for radiologists during subsequent imaging procedures.

Freehand skin surface compression is used in commercial ultrasound elastography and a similar method could be coupled with OCT. Such a technique reduces procedural complexity compared to the implant method or other experimental contrast techniques such as MM-OCT. Freehand elastography requires image tracking and elastography processing techniques fast enough to allow online imaging. The tracker must also be robust against decorrelation from subject/probe motion, something which is a greater problem in OCT where any small movement translates into sizeable motion within the image. The increased risk of decorrelation can be reduced by measuring displacements between A-lines rather than B-scans. This is described in Chapter 5. Such a technique also allows for an increase in axial displacement sensitivity through the sampling of phase data rather than image intensities. Actuation under such an imaging regime must be capable of generating a consistent elastographic measurement across an entire B-scan. This could be achieved via the use of piezo-electrics coupled to the skin via the OCT probe [111]. The optimal actuation profile and potential need for system synchronisation would need to be explored further for such a method. Any actuation technique should produce a sizeable axial stress, as axial displacement measurements can only sample this component.

In conclusion, this thesis sets out a firm basis for informing future development of OCE, especially when characterising discrete changes to mechanical properties within tissue using OCT systems similar to those produced by MDL. A number of key points have been raised, such as the need for exerting a repeatable, controlled and non-invasive actuation on the micron scale, regardless of patient motion. Furthermore the strengths and limitations faced by correlation-based and phase sensitive displacement tracking techniques have been highlighted. In particular, experimental results have identified the upper and lower bounds of each method's displacement sensitivity. This is crucial for identifying the nature of future actuators, whilst underlining the competing effects of image acquisition speeds versus the relative motion of actuation apparatus, imaging probe and patient. The remote, correlation-based OCE technique described in this thesis produced useful elastographic information not present in standard OCT images using a controlled and repeatable actuation at the cost of speed, sensitivity and invasiveness. The phase sensitive approach resulted in greater displacement sensitivity and higher acquisition speeds, whilst reducing invasiveness at the cost of higher decorrelation rates. A future commercial OCE system would have to combine the strengths of both approaches whilst mitigating their short-comings. Finally, based on the results in Chapter 4 it is conceivable that changes in skin pathology could be measured using OCE and that enhancements to sensitivity as described in Chapter 5 may in future lead to OCE proving useful as a diagnostic aid in the detection of skin cancer.

Future work to extend the research contained within this thesis should concentrate on a few specific points. Whilst it has been demonstrated in Chapter 5 that phase shifts can be detected where the OCT signal intensity is homogenous (i.e. in a sample with uniform structure), questions still remain over whether MM-OCT produces a useful phase contrast signal independent of the imaged tissue structure in a cancer model. This could be demonstrated by investigating the processes by which MNPs are transported to, deposited in and mechanically linked with the target tissue. The light scattering properties of this target tissue and a better understanding of the dynamics of magnetomotion in-vivo would contribute to understanding the efficacy of the method. Detection of a phase signal from applied vibration also raises questions which require investigation; fundamentally, how tissue response varies with tissue type, frequency and amplitude. Furthermore, the potential of time reversal elastography could be explored, as could crawling wave elastography where two indenters are used to generate an interference pattern, as already demonstrated in ultrasound [132, 121]. There is also scope to develop the fundamental correlation-based approach outlined in Chapter 4. Technologically, questions still remain over how best to deploy a source of shear stress and there is broad scope to improve upon the speed and effectiveness of the 2D NCC image tracking methods used, other techniques already exist which may provide enhanced speed and sensitivity [133, 134].

Bibliography

[1] F. Bazant-Hegemark, N. Stone, G. McKenzie, and J. Holmes, “Optical coherence tomography aids cancer detection,” *Biophotonics International* , November 2007.

[2] G. J. Tearney, S. Waxman, M. Shishkov, B. J. Vakoc, M. J. Suter, M. I. Freilich, A. E. Desjardins, W. Y. Oh, L. A. Bartlett, M. Rosenberg, and B. E. Bouma, “Three-Dimensional Coronary Artery Microscopy by Intracoronary Optical Frequency Domain Imaging,” *J Am Coll Cardiol Img* **1**(6), pp. 752–761, 2008.

[3] J. M. Olmedo, K. E. Warschaw, J. M. Schmitt, and D. L. Swanson, “Correlation of thickness of basal cell carcinoma by optical coherence tomography in vivo and routine histologic findings: A pilot study,” *Dermatol. Surg.* **33**, pp. 421–426, 2007.

[4] M. Ohmi, M. Ohnishi, D. Takeda, and M. Haruna, “Dynamic analysis of laser ablation of biological tissue using real-time optical coherence tomography,” *Meas. Sci. Technol.* **21**, 2010.

[5] M. H. Zulfakar, A. Alex, B. Povazay, W. Drexler, C. P. Thomas, R. M. Porter, and C. M. Heard, “In vivo response of GsdmA3Dfl mice to topically applied anti psoriatic agents: effects on epidermal thickness, as determined by optical coherence tomography and H & E staining,” *Experimental Dermatology* **21**, pp. 269–272, 2011.

[6] F. G. Bechara, T. Gambichler, M. Stucker, A. Orlikov, S. Rotterdam, P. Altmeyer, and K. Hoffmann, “Histomorphologic correlation with routine histology and optical coherence tomography,” *Skin Res. and Technol.* **10**, pp. 169–273, 2004.

[7] R. G. Pomerantz, D. Zell, G. McKenzie, and D. Siegel, “Optical coherence tomography as a tool to delineate basal cell carcinoma prior to Mohs micrographic surgery.” J. Am. Acad. of Dermatol.

[8] D. Cunha, T. Richardson, N. Sheth, G. Orchard, and A. C. nd R. Mallipeddi, “Comparison of ex vivo optical coherence tomography with conventional frozen- section histology for visualizing basal cell carcinoma during Mohs micrographic surgery,” *Brit. J. Dermatol.* **163**, pp. 101–117, 2010.

[9] M. Mogensen, T. M. Jorgensen, L. Thrane, B. M. Numberg, and G. B. E. Jemec, “Improved quality of optical coherence tomography imaging of basal cell carcinomas using speckle reduction,” *Exp. Derm.* **19**, pp. 293–295, 2009.

[10] C. K. Hitzenberger, E. Gotzinger, M. Sticker, M. Pircher, and A. F. Fercher, “Measurement and imaging of birefringence and optic axis orientation by phase resolved polarization sensitive optical coherence tomography,” *Optics Express* **9**, pp. 780–790, 2001.

[11] M. C. Pierce, J. Strasswimmer, B. H. Park, B. Cense, and J. F. de Boer, “Advances in optical coherence tomography imaging for dermatology,” *J. Invest. Dermatol.* **123**, pp. 458–463, 2004.

[12] A. Dubois, K. Grieve, G. Moneron, R. Lecaque, L. Vabre, and C. Boccara, “Ultrahigh-resolution full-field optical coherence tomography,” *Appl. Opt.* **43**, pp. 2874–2883, 2004.

[13] J. Holmes, S. Hattersley, N. Stone, F. Bazant-Hegemark, and H. Barr, “Multichannel fourier domain oct system with superior lateral resolution for biomedical applications,” *Proc. SPIE* **6847**, 2008.

[14] K. J. Parker, M. M. Doyley, and D. J. Rubens, “Imaging the elastic properties of tissue: the 20 year perspective,” *Phys. Med. Biol.* **56**, pp. 513–543, 2011.

[15] S. G. Proskurin and I. V. Meglinski, “Optical coherence tomography imaging depth enhancement by superficial skin optical clearing,” *Las. Phys. Lett.* **4**, 2007.

[16] A. M. Gobin, M. H. Lee, N. J. Halas, W. D. James, R. A. Drezek, and J. L. West, “Near-infrared resonant nanoshells for combined optical imaging and photothermal cancer therapy,” *Nano Letters* **7**, 2007.

[17] J. F. deBoer, T. E. Milner, M. Gemert, and J. S. Nelson, “Two-dimensional birefringence imaging in biological tissue by polarization-sensitive optical coherence tomography,” *Optics Letters* **2**, 1997.

[18] M. Nakajima, “Elastographic and color doppler diagnosis of skin tumors,” *Proc. Rad. Soc. North Am. Scientific Assembly* , 2007.

[19] D. Mehregan, “A study of ultrasonography with elastography in skin neoplasms,” *ClinicalTrials.gov Identifier: NCT01259037.* , December 2010.

[20] “Fact sheet 297,” Geneva, 2008. Published by the World Health Organization.

[21] Office for National Statistics, Newport, *Cancer Statistics, Registrations of cancer diagnosed in 2005, England*, series mb1 no 36 ed., 2008.

[22] “The global burden of disease 2004 update,” 2004. Published by the World Health Organization.

[23] J. G. Fujimoto, “Optical coherence tomography for ultrahigh resolution in vivo imaging,” *nature* **21**, pp. 1361–1367, 2003.

[24] Z. Yuan and et. al., “High-resolution imaging diagnosis and staging of bladder cancer: comparison between optical coherence tomography and high frequency ultrasound,” *J. Biomed. Opt* **13(5)**, p. 054007, 2008.

[25] A. F. Fercher, W. Drexler, C. K. Hitzenberger, and T. Lasser, “Optical coherence tomography - principles and applications,” *Rep. Prog. Phys* **66**, pp. 239–303, 2003.

[26] J. B. Little, “Radiation carcinogenesis,” *Carcinogenesis* **21**(3), pp. 397–404, 2000.

[27] M. Marmot, T. Atinmo, T. Byers, J. Chen, T. Hirohata, A. Jackson, W. James, L. Kolonel, S. Kumanyika, C. Leitzmann, J. Mann, H. Powers, K. Reddy, E. Riboli, J. Rivera, A. Schatzkin, J. Seidell, D. Shuker, R. Uauy, W. Willett, and S. Zeisel, “Food, nutrition, physical activity, and the prevention of cancer: a global perspective,” research report, American Institute for Cancer Research, Washington, USA, November 2001.

[28] I. Weinstein, “Disorders in cell circuitry during multistage carcinogenesis: the role of homeostasis,” *Carcinogenesis* **21**(5), pp. 857–864, 2000.

[29] P. Mettesheim, D. J. Fitzgerald, H. Kitamura, C. L. Walker, T. M. Gilmer, J. C. Barrett, and T. E. Gray, “In vitro analysis of multistage carcinogenesis,” *Environmental Health Perspect.* **75**, pp. 71–79, 1987.

[30] I. R. Hart and I. J. Fidler, “Cancer invasion and metastasis,” *The Quarterly Review of Biology* **55**(2), pp. 121–142, 1980.

[31] R. C. Bast, D. W. Kufe, R. E. Pollock, R. R. Weichselbaum, J. F. Holland, E. Frei, and T. S. Gansler, *Cancer Medicine 6th Edition*, BC Decker, Canada, 2000.

[32] N. C. Institute, “Staging: Questions and answers, sheet 5.32,” Canada, 2004.

[33] I. D. Fleming, J. S. Cooper, D. E. Henson, R. V. P. Hutter, B. J. Kennedy, G. P. Murphy, B. O’Sullivan, L. H. Sobin, and J. W. Yarbro, *AJCC Cancer Staging Manual.* New York, fifth ed., 1997.

[34] C. O’Neal and J. E. Cleary, “Pancreatic cancer,” *The American Journal of Nursing* **100**(4), pp. 23–26, 2000.

[35] C. Engelking, “The language of staging,” *The American Journal of Nursing* **87**(11), pp. 1434–1437, 1987.

[36] D. S. Rigel, *Cancer of the Skin*, Elsevier, 2005.

[37] R. S. Stern, “Prevalence of a history of skin cancer in 2007,” *Arch. Dermatol.* **146**, 2007.

[38] S. Rajpar and J. Marsden, *ABC of Skin Cancer*, Blackwell Publishing, 2008.

[39] R. M. Mackie, *Skin Cancer*, Martin Dunitz, 1996.

[40] S. H. Yun, G. J. Tearney, J. F. deBoer, N. Iftimia, and B. E. Bouma, “High-speed optical frequency-domain imaging,” *Optics Express* **11**, pp. 2953–2963, 2003.

[41] 2011. Figure obtained from Wikipedia, URL: http://en.wikipedia.org/wiki/File:Ss-oct.PNG.

[42] M. Wojtkowski, A. Kowalczyk, R. Leitgeb, and A. F. Fercher, “Full range complex spectral optical coherence tomography technique in eye imaging,” *Optics Letters* **27**, pp. 1415–1417, 2002.

[43] S. Yun, G. Tearney, J. deBoer, N. Iftimia, and B. Bouma, "High-speed optical frequency-domain imaging," *Optics Express* **11**, pp. 2953–2963, 2003.

[44] M. A. Choma, M. V. Sarunic, C. Yang, and J. A. Izatt, "Sensitivity advantage of swept source and fourier domain optical coherence tomography," *Optics Express* **11**(18), pp. 2183–2189, 2003.

[45] M. Vogt, A. Knuttel, K. Hoffmann, P. Altmeyer, and H. Ermert, "Comparison of high frequency ultrasound and optical coherence tomography as modalities for high resolution and non invasive skin imaging," *Biomed. Technik.* **48**, pp. 116–121, 2003.

[46] H. F. Zhang, K. Maslov, G. Stoica, and L. V. Wang, "Functional photoacoustic microscopy for high-resolution and noninvasive in vivo imaging," *Nature Biotech.* **24**, pp. 848–851, 2003.

[47] J. Ophir, B. Garra, F. Kallel, E. Konofagou, T. Krouskop, R. Righetti, and T. Varghese, "Elastographic imaging," *Ultrasound in Med & Biol.* **26**, pp. s23–s29, 2000.

[48] J. Ophir, I. Cespedes, H. Ponnekanti, Y. Yazdi, and X. Li, "Elastography: A quantitative method for imaging the elasticity of biological tissues," *Ultrason. Imaging* **13**, pp. 111–134, 1991.

[49] M. Bilgen and M. F. Insana, "Deformation models and correlation analysis in elastography," *J. Acoust. Soc. Amer.* **99**, pp. 3212–3224, 1996.

[50] D. Melodelima, J. C. Bamber, F. A. Duck, J. A. Shipley, and L. J. Xu, "Elastography for breast cancer diagnosis using radiation force: System development and performance evaluation," *Ultrasound. Med. Biol.* **32**, pp. 387–396, 2006.

[51] H. Ko, W. Tan, R. Stack, and S. A. Boppart, "Optical coherence elastography of engineered and developing tissue," *Tissue Engineering* **12**, pp. 63–73, 2006.

[52] Y. Liu, Y. Liang, G. Mu, and X. Zhu, "Deconvolution methods for image deblurring in optical coherence tomography," *JOSA A* **26**(1), pp. 72–77, 2009.

[53] I.-C. Jan, C.-H. Chiu, E.-K. Tien, and G.-J. Jan, "Study on deconvolution algorithms for optical coherent tomography," *J. Med. Biol. Eng.* **23**, pp. 73–78, 2003.

[54] T. G. van Leeuwen, D. J. Faber, and M. C. Aalders, "Measurement of the axial point spread function in scattering media using single-mode fiber-based optical coherence tomography," *IEEE J. Sel. Top. Quantum Electronics* **9**, pp. 227–233, 2003.

[55] P. D. Woolliams, R. A. Ferguson, C. Hart, A. Grimwood, and P. H. Tomlins, "Spatially deconvolved optical coherence tomography," *Applied Optics* **49**(11), pp. 2014–2021, 2010.

[56] P. H. Tomlins, O. Adegun, E. Hagi-Pavli, K. Piper, and D. Bader, "Scattering attenuation microscopy of oral epithelial dysplasia," *J. Biomed. Opt.* **15**, pp. 66003–66011, 2010.

[57] A. Agrawal, T. Pfefer, N. Gilani, and R. Drezek, "Three-dimensional characterization of optical coherence tomography point spread functions with a nanoparticle-embedded phantom," *Opt. Lett.* **35**, pp. 2269–2271, 2010.

[58] L. Zhifang, L. Hui, H. Youwu, C. Shoudong, and X. Shusen, "A model of speckle contrast in optical coherence tomography for characterizing the scattering coefficient of homogenous tissues," *Phys. Med. Biol* **53**, pp. 5859–5866, 2008.

[59] I. V. Turchin, E. A. Sergeeva, L. S. Dolin, V. A. Kamensky, N. M. Shakhova, and R. Richards-Kortum, "Novel algorithm of processing optical coherence tomography images for differentiation of biological tissue pathologies," *Journal of Biomedical Optics* **10**(6), 2005.

[60] J. M. Schmitt, "Optical coherence tomography (oct): a review," *IEEE Journal of Selected Topics in Quantum Electronics* **5**(4), pp. 1205–1215, 1999.

[61] Y. Feng, R. K. Wang, and J. B. Elder, "Theoretical model of optical coherence tomography for system optimization and characterization," *J. Opt. Soc. Am. A* **20**(9), pp. 1792–1803, 2003.

[62] V. V. Tuchin, *Tissue optics: light scattering methods and instruments for medical diagnosis*, SPIE, Washington, USA, second ed., 2007.

[63] P. Rolfe, F. Scopesi, and G. Serra, "Advances in fibre-optic sensing in medicine and biology," *Meas. Sci. Technol* **18**, pp. 1683–1688, 2007.

[64] S. L. Jacques, C. A. Alter, and S. A. Prahl, “Angular dependence of hene laser light scattering by human dermis,” *Lasers in the Life Sciences* **1**(4), pp. 309–334, 1987.

[65] A. Ishimaru, “Wave propogation and scattering in random media,” *Single Scattering and Transport Theory* **1**, 1978.

[66] M. S. Twardowski, E. Boss, J. B. Macdonald, W. S. Pegau, A. H. Bernard, and J. R. V. Zaneveld, “A model for estimating bulk refractive index from the optical backscattering ratio and the implications for understanding particle composition in case i and case ii waters,” *J. Geophys. Res.* **106**, pp. 129–142, 2001.

[67] P. H. Tomlins, R. A. Ferguson, C. Hart, and P. D. Woolliams, “Point-spread function phantoms for optical coherence tomography,” research report, National Physical Laboratory, Teddington, UK, 2009.

[68] M. Born and E. Wolf, *Principles of Optics: Electromagnetic Theory of Propagation, Interference and Diffraction of Light*, Cambridge University Press, Cambridge, UK, 6th ed., 1999.

[69] C. Bisaillon, G. Lamouche, R. Maciejko, M. Dufour, and J. Monchalin, “Deformable and durable phantoms with conrtolled density of scatterers,” *Phys. Med. Biol.* **53**, pp. N237–N247, 2008.

[70] R. K. Wang, “Resolution improved optical coherence-gated tomography for imaging through biological tissues,” *Journal of Modern Optics* **46**(13), pp. 1905–1912, 1999.

[71] J. M. Schmitt, “Restoration of optical coherence images of living tissue using the clean algorithm,” *J. Biomed. Opt* **3**(66), pp. 66–75, 1998.

[72] P. H. Tomlins and R. K. Wang, “Matrix approach to quantitative refractive index analysis by fourier domain optical coherence tomography,” *JOSA A* **23**(8), pp. 1897–1907, 2006.

[73] R. C. Gonzalez and R. E. Woods, *Digital Image Processing*, Prentice Hall, 3rd ed., 2008.

[74] J. M. Schmitt, “Oct elastography: imaging microscopic deformation and strain of tissue,” *Optics Express* **3**, pp. 199–211, 1998.

[75] J. Rogowska, N. A. Patel, J. G. Fujimoto, and M. E. Brezinski, "Optical coherence tomographic elastography technique for measuring deformation and strain of atherosclerotic tissues," *Heart* **90**, pp. 556–562, 2004.

[76] R. C. Chan, A. H. Chau, W. C. Karl, S. Nadkarni, A. S. Khalil, N. Iftimia, M. Shishkov, G. J. Tearney, M. R. Kaazempur-Mofrad, and B. E. Bouma, "Oct-based arterial elastography: robust estimation exploiting tissue biomechanics," *Optics Express* **12**, pp. 4558–4572, 2004.

[77] A. Grimwood, L. Garcia, J. C. Bamber, P. Tomlins, J. Holmes, and Q. A. Pankhurst, "Elastographic contrast generation in optical coherence tomography from a localized shear stress," *Phys. Med. Biol.* **55**, pp. 5515–5528, 2010.

[78] F. Kallel and J. Ophir, "A least squares strain estimator for elastography," *Ultrasonic Imaging* **19**, pp. 195–208, 1997.

[79] R. J. Dickinson and C. R. Hill, "Measurement of soft tissue motions using correlation between a-scans," *Ultrasound. Med. Biol.* **8**, pp. 263–271, 1982.

[80] P. G. M. DeJong, T. Arts, A. P. G. Hoeks, and R. S. Reneman, "Determination of tissue motion velocity by correlation interpolation of pulsed ultrasonic echo signals," *Ultrason. Imaging* **12**, pp. 84–98, 1990.

[81] A. Hein and W. D. O'Brien, "Current time-domain methods for assessing tissue motion by analysis from reflected ultrasound echoes - a review," *IEEE Trans. Ultrason. Ferroel. Freq. Control* **40**, pp. 84–102, 1993.

[82] J. P. Lewis, "Fast template matching," *Vision Interface* , pp. 120–123, 1995.

[83] J. Westerweel, "Fundamentals of digital particle image velocimetry," *opt. Commun.* **8**, pp. 1379–1392, 1997.

[84] B. S. Ramamurthy and G. E. Trahey, "Potential and limitations of angle-independent flow detection algorithms using radio-frequency and detected echo signals," *Ultrasonic Imaging* **13**, pp. 252–268, 1991.

[85] M. Brezinski, *Optical coherence tomography*, Elsevier, 2006.

[86] J. W. Goodman, "Statistical properties of laser speckle patterns," *Topics in Applied Physics* **9**, pp. 9–75, 1975.

[87] R. F. Wagner, S. W. Smith, J. M. Sandrik, and H. Lopez, "Statistics of speckle in ultrasound b-scans," *IEEE Trans. Sonics and Ultrasonics* **30**, pp. 156–163, 1983.

[88] S. J. Kirkpatrick, "Tissue analysis using optical coherence elastography," January 2008. SPIE Photonics West course notes.

[89] R. F. Wagner, M. F. Insana, and D. G. Brown, "Statistical properties of radio-frequency and envelope-detected signals with applications to medical ultrasound," *J. Opt. Soc. Am. A* **4**, pp. 910–922, 1987.

[90] S. J. Kirkpatrick, "Simspeck: Numerical simulation & analysis tools for laser speckle."

[91] L. N. Bohs and G. E. Trahey, "A novel method for angle independent ultrasonic imaging of blood flow and tissue motion," *IEEE Trans. Biomedical Eng.* **38**, pp. 280–286, 1991.

[92] S. Hecht, "The visual discrimintation of intensity and the weber-fechner law," *Journal of General Physiology* **7**, pp. 235–267, 1924.

[93] M. Brezinski, *Optical coherence tomography*, Elsevier, 2006.

[94] M. Bilgen and M. F. Insana, "Deformation models and correlation analysis in elastography," *J. Acoust. Soc. Am.* **99**, pp. 3212–3224, 1991.

[95] E. J. Chen, W. K. Jenkins, and W. D. O. Jr, "The accuracy and precision of estimating tissue displacements from ultrasonic images," 1992. IEEE Ultrasonics Symposium, pp 1069-1072.

[96] S. J. Kirkpatrick and R. K. W. ad D. D. Duncan, "Oct-based elastography for large and small deformations," *Optics Express* **14**(24), pp. 11585–11597, 2006.

[97] R. Gaspari, D. Blehar, M. Mendoza, A. Montoya, C. Moon, and D. Polan, "Use of ultrasound elastography for skin and subcutaneous abscesses," *J. Ultrasound Med.* **28**, pp. 855–860, 2009.

[98] Y. Zhang, R. T. Brodell, E. N. Mostow, C. J. Vinyard, and H. Marie, "In vivo skin elastography with high-definition optical videos," *Skin Res. and Technol.* **15**, pp. 271–282, 2009.

[99] M. Nakajima, M. Shimizu, O. Kishino, R. Igarashi, K. Takeuchi, Y. Kiyohara, and K. Nanri, “Elastographic diagnosis of skin tumors,” *Proc. XIXthe Congress of European Federation of Societies for Ultrasound in Medicine and Biology* , 2006.

[100] S. J. Kirkpatrick, R. K. Wang, D. D. Duncan, M. Kulesz-Martin, and K. Lee, “Imaging the mechanical stiffness of skin lesions by in-vivo acousto-optical elastography,” *Optics Express* **14**, pp. 9770–79, 2006.

[101] A. L. Oldenburg, V. Crecea, S. A. Rinne, and S. A. Boppart, “Phase-resolved magnetomotive oct for imaging nanomolar concentrations of magnetic nanoparticles in tissues,” *Optics Express* **16**, pp. 11525–39, 2008.

[102] V. Crecea, A. L. Oldenburg, L. Xing, T. S. Ralston, and S. A. Boppart, “Magnetomotive nanoparticle transducers for optical rheology of viscoelastic materials,” *Optics Express* **17**, pp. 23114–22, 2009.

[103] C. Bisaillon, G. Lamouche, R. Maciejko, M. Dufour, and J. Monchalin, “Deformable and durable phantoms with controlled density of scatterers,” *Phys. Med. Biol* **53**, pp. 237–47, 2008.

[104] D. P. Popescu, M. D. Hewko, and M. G. Sowa, “Speckle noise attenuatio in optical coherence tomography by compounding images acquired at different positions of the sample,” *opt. Commun.* **269**, pp. 247–51, 2007.

[105] F. Khatyr, C. Imberdis, P. Vescovo, D. Varchon, and J. Lagarde, “Model of the viscoelastic behaviour of skin in vivo and study of anisotropy,” *Skin. Res. Technol.* **10**, pp. 96–103, 2004.

[106] A. L. Oldenburg and S. A. Boppart, “Resonant acoustic spectroscopy of soft tissues using embedded magnetomotive nanotransducers and optical coherence tomography,” *Phys. Med. Biol.* **55**, p. 1189, 2010.

[107] D. Melodelima, J. C. Bamber, F. A. Duck, and J. A. Shipley, “Transient elastography using impulsive ultrasound radiation force: a preliminary comparison with surface palpation elastography,” *Ultrasound Med. Biol.* **33**, pp. 959–969, 2007.

[108] Z. H. Hamdoon, W. Jerjes, T. Upile, and C. Hopper, “Optical coherence tomography-guided photodynamic therapy for skin cancer: Case study,” *Photodiag. and Photo. Therapy* **8**, 2011.

[109] B. Dasgen and E. Siegel, “Elastographic ultrasound quantitative analysis combined with high frequency imaging for characterisation of benign and malignant skin lesions,” *Radiological Society of North America Scientific Assembly* , December 2009.

[110] P. Wendling, “Ultrasound elastography helps id skin cancer,” *Family Practice News* , January 2010.

[111] B. F. Kennedy, X. Liang, S. G. Adie, D. K. Gerstmann, B. C. Quirk, S. Boppart, and D. D. Sampson, “In vivo three-dimensional optical coherence elastography,” *Optics Express* **19**, 2011.

[112] X. Liang, A. Oldenburg, V. Crecea, E. Chaney, and S. Boppart, “Optical micro-scale mapping of dynamic biomechanical tissue properties,” *Optics Express* **16**(15), pp. 11052–11065, 2008.

[113] R. John, R. Rezaeipoor, S. G. Adie, E. J. Chaney, A. L. Oldenburg, M. Marjanovic, J. P. Haldar, B. P. Sutton, and S. A. Boppart, “In vivo magnetomotive optical molecular imaging using targeted magnetic nanoprobes,” *PNAS* **107**, pp. 8085–8090, 2010.

[114] Y. Zhao, Z. Chen, C. Saxer, S. Xiang, J. F. DeBoer, and J. S. Nelson, “Phase-resolved optical coherence tomography and optical doppler tomography for imaging blood flow in human skin with fast scanning speed and high velocity sensitivity,” *Opt. Lett.* **25**, pp. 114–116, 2000.

[115] R. K. Wang, Z. Me, and S. J. Kirkpatrick, “Tissue doppler optical coherence elastography for real time strain rate and strain mapping of soft tissue,” *Appl. Phys. Lett.* **89**, 2006.

[116] B. W. Graf, S. G. Adie, and S. A. Boppart, “Correction of coherence gate curvature in high numerical aperture optical coherence imaging,” *Opt. Lett.* **35**, pp. 3120–3122, 2010.

[117] J. Fingler, D. Schwartz, C. Yang, and S. E. Fraser, “Mobility and transverse flow visualization using phase variance contrast with spectral domain optical coherence tomography,” *Optics Express* **15**, pp. 12636–12653, 2007.

[118] R. K. Wang, S. J. Kirkpatrick, and M. Hinds, “Phase-sensitive optical coherence elastography for mapping tissue microstrains in real time,” *Appl. Phys. Lett.* **90**, p. 164105, 2007.

[119] S. G. Adie, X. Liang, B. F. Kennedy, R. John, D. D. Sampson, and S. A. Boppart, “Spectroscopic optical coherence elastography,” *Optics Express* **18**, pp. 25519–25534, 2010.

[120] March 2011. Private communication, Jon Holmes, CEO MDL.

[121] K. Hoyt, J. Parker, and D. J. Rubens, “Sonoelastographic shear velocity imaging: Experiments on tissue phantom and prostate,” *Proc. IEEE Ultrason. Symp.* , pp. 1686–1689, 2006.

[122] F. Bazant-Hegemark, D. Woods, S. Hattersley, and J. Holmes, “Multi-beam resolution video-rate swept-source optical coherence tomography (oct) provides endogenous contrast for in vivo blood flow independent of flow direction,” *Proc. SPIE* **7554**, p. 75542, 2010.

[123] K. Nightingale, S. McAleavey, and G. Trachey, “Shear-wave generation using acoustic radiation force: in vivo and ex vivo results,” *Ultrasound Med. Biol.* **29**, pp. 1715–1723, 2003.

[124] J. Gennisson, T. Baldeweck, M. Tanter, S. Catheline, M. Fink, L. Sandrin, C. Cornillon, and B. Querleux, “Assessment of elastic parameters of human skin using dynamic elastography,” *IEEE Trans. Ultrason., Ferroelectr., Freq. Control* **15**, pp. 980–989, 2004.

[125] A. L. Oldenburg, F. Toublan, K. Suslick, A. Wei, and S. Boppart, “Magnetomotive contrast for in vivo optical coherence tomography,” *Optics Express* **13**, pp. 6597–6614, August 2005.

[126] Y. J. Wang, S. M. Hussain, and G. P. Krestin, “Superparamagnetic iron oxide contrast agents: physiochemical characteristics and applications in mr imaging,” *Eur. Radiol.* **11**, pp. 2319–2331, 2001.

[127] A. Nacev, C. Beni, O. Bruno, and B. Shapiro, “The behaviors of ferromagnetic nano-particles in and around blood vessels under applied magnetic fields,” *J. Magn. Magn. Mater.* **323**, pp. 651–668, 2011.

[128] S. Nishijima, F. Mishima, T. Terada, and S. Takeda, “A study on magnetically targeted drug delivery system using superconducting magnet,” *Physica C* **463-465**, pp. 1311–1314, 2007.

[129] Q. A. Pankhurst, J. Connolly, S. K. Jones, and J. Dobson, “Applications of magnetic nanoparticles in biomedicine,” *J. Phys. D: Appl. Phys* **36**, pp. R167–R181, 2003.

[130] J. Oh, M. Feldman, J. Kim, H. Kang, P. Sanghi, and T. Milner, “Magnetomotive detection of tissue-based macrophages by differential phase optical coherence tomography,” *Lasers in Medicine* **39**, pp. 266–272, 2007.

[131] S. Mornet, S. Vasseur, Grasset, P. Veverka, G. Goglio, A. Demourgues, J. Portier, E. Pollert, and E. Duguet, “Magnetic nanoparticle design for medical applications,” *J.Prog. Solid St. Chem.* **34**, pp. 237–247, 2006.

[132] R. K. Ing and N. Quieffin, “In solid localization of finger impacts using acoustic time-reversal process,” *Appl. Phys. Lett.* **87**, 2005.

[133] A. Kapoor, A. Kapoor, G. Mahajan, and B. S. Sidhu, “Real-time elastography in the detection of prostate cancer in patients with raised PSA level,” *Ultrasound Med. Biol.* **37**, pp. 1375–1381, 2011.

[134] J. Bojunga, E. Hermann, G. Meyer, S. Weber, S. Zeuzem, and M. Friedrich-Rust, “Real-time elastography for the differentiation of benign and malignant thyroid nodules: A meta-analysis,” *Thyroid* **20**, pp. 1145–1150, 2010.

List of Figures

Appendices

Appendix A

OCT Company Systems and Performance Data

The tables below are a summary of active OCT manufacturers, their target applications and system performances as described on their respective websites and brochures. All information was collected in May 2008.

COMPANY	SPECIALISATION	SPECIFICATIONS:					ADDITIONAL NOTES
		RESOLUTION	SCAN RATES	LIGHT SOURCE	FDA APPROVED	PROBE TYPE	
GLUCOLIGHT US	DIABETES	-	-	-	FDA study commencing this year	Skin patch probe	Equipment is self-calibrating Non-imaging device Remote oximetry sensing using OCT Patent granted NOT COMMERCIALLY AVAILABLE YET (still in trials phase)
LIGHTLAB US	CARDIOLOGY /ENDOSCOPY	15µm	Whole image acquisition at 1mm/s	-	-	Catheter	Optical core is 0.006" diameter Patents for balloon catheter, and probe
LANTIS US	DENTISTRY	-	-	-	-	Side-scanning	FD-OCT Imaging system to be launched late 2008 Target retail price of $20,000 Real-time acquisiation Rates and resolutions not explicitly stated
OPTOVUE US	OPTHALMOLOGY	5 µm axial 15 µm lateral	26,000 A-scans/second 256 - 4096 A-scans/frame	810nm +/- 10nm	-	No probe	FD-OCT Power of 750 uW Speckle reduction 2 - 2.3mm imaging depth 2 - 12mm frame width

HEIDELBERG **Germany/US**	**OPTHALMOLOGY** **/ANGIOGRAPHY**	**-**	**40,000 A-scans/second**	**-**	**FDA approved**	**No probe**	**SD-OCT** **Real-time calibration mechanisms** **Multiple Commercial Products** **OCT with autofluorescence, fluorescein angiography, ICG angiography**
BIOPTIGEN **US**	**OPTHALMOLOGY** **/R&D**	**~10 μm**	**-**	**840nm** **or 1310nm**	**FDA cleared**	**No probe**	**SD-OCT** **Small animal studies performed on tadpoles & rodents**
CARL ZEISS **US**	**OPTHALMOLOGY**	**5 μm axial** **15 μm lateral**	**27,000 A-scans/second**	**840nm SLD**	**FDA approved**	**No probe**	**HD-OCT (SD-OCT)** **Scan depth of 2mm**
OPTOPOL **Poland**	**OPTHALMOLOGY**	**3 μm axial** **7 μm lateral**	**25000 A-scan/second**	**840nm SLD**	**-**	**No Probe**	**SD OCT** **1024 A-scan points** **10600 A-scans per B-scan** **Doppler available**
		3 μm axial **12-18 μm lateral**	**55000 A-scans/second**	**840nm SLD**	**-**	**No Probe**	
ISIS OPTRONICS **Germany**	**DERMATOLOGY**	**3 μm lateral** **5 μm axial**	**-**	**1300nm**	**-**	**Armature-mounted**	**-**
TOMOPHASE **US**	**PULMINOLOGY** **/ONCOLOGY**	**Stated as μm**	**-**	**-**	**-**	**Endoscope** **forward & sideward looking**	**Claims to image 2-3mm below tissue surface** **"circumvents the conventional optical interferometer"** **Spectral absorbance mapping & phase contrast**

SANTEC **Japan**	**R&D**	**12 µm axial** **17 µm lateral**	**75 fps** **(260 lines/frame)**	**1310**	**-**	**Microscope stage** **Probe optional**	**SS-OCT** **3mm imaging depth** **15mm imaging width** **20,000 lines/second**
IMALUX **US**	**ENDOSCOPY** **/R&D**	**10-20 µm**	**1.5 seconds/frame (for 200 pixel widths)**	**SLD (NIR)**	**FDA Cleared** **ISO & CE Marked**	**Reuseable** **fibreoptic**	**Compact Design**
THORLABS **UK/international**	**R&D**	**15 µm lateral** **9 µm axial**	**16kHz** **25fps**	**1325nm** **(100nm bandwidth)**	**-**	**Microscope** **& Probe**	**SS-OCT** **10mW Power** **Detailed Specs on Website** **£37,800**
		4.5 µm axial	**8 fps**	**900nm** **(10nm FWHM)**	**-**	**Microscope** **& Probe**	**Spectral Radar OCT** **3 Variants: Standard, High-Res (described), Deep Imaging** **1.5mW** **1.1mm imaging depth** **£19,650**
MICHELSON **DIAGNOSTICS** **UK**	**ONCOLOGY**	**<10 µm axial** **<7.5 µm lateral**	**Refresh rate 1Hz** **10kHz A-Line rate** **1.9 fps for 5mm width**	**1310nm** **(15nm FWHM)** **150nm sweep**		**Microscope**	**SS-OCT** **5.3 µm pixel size** **7mm image width** **2mm imaging depth** **15mW laser power**

Appendix B

Turchin's RTE for a Layered Medium

The mathematical model described here approximates OCT signal decay through stratified media [59]. Comparison between simulated and experimental data appear favourable when tested under a bi-layer regime. Such a model provides a closer mathematical approximation of the observed OCT signal profiles obtained when imaging the bi-layer phantoms described in Chapter 2.

Turchin describes a model in line with Mie theory, a standard assumption for the behaviour of an OCT source through tissue. The model addresses multiple small-angle scattering at shallow depths, as well as diffusion processes deeper into tissue. It produces an OCT signal profie $I(z)$ based on three variables: the layer's scattering coefficient μ_s, its probability of backscatter p_b, and $\langle\lambda^2\rangle$ the angular variance of scattering phase function.

It is assumed that the scattering phase function $x(z,\lambda)$ is based on the approximation that only single backscatter events take place, owing to the low probability of high angle scatters. This produces a phase function that is the sum of a backscatter probability coefficient p_b and a first-approximation of the phase term $x_1(z,\lambda)$ which tends to zero for $\lambda > \pi/2$:

$$x(z,\lambda) = (1-2p_b(z))\,x_1(z,\lambda) + 2p_b(z) \tag{B.1}$$

where,

$$\frac{1}{2}\int_0^\infty x_1(z,\lambda)\lambda d\lambda = 1$$

The angular spectrum $\tilde{x_1}(z,p)$ for the first-approximation phase function is given by the integral of the phase function zero-order Bessel product (J_0):

$$\tilde{x_1}(z,p) = \frac{1}{2}\int_0^{\infty} x_1(z,\lambda)J_0(p\lambda)\lambda d\lambda \tag{B.2}$$

Using this information, a term for the OCT signal $I(z)$ can be derived from the convolution of an intensity distribution for a point source over the transverse plane $U(z,x)$. The intensity distribution incorporates a term characterising diffusion components of the beam scatter. Additionally, the term B relates an arbitrary coefficient unique to each OCT system, which appears to represent a scalar quantity of the system's source – although this is not stated by Turchin.

$$I(z) = 2p_b(z)\mu_s(z)B\int_{-\infty}^{\infty}\left[2U^2(z,x) - U_0^2(z,x)\right]dx \tag{B.3}$$

The above term does not take account of the OCT's optics. These are modelled on Gaussian approximations suitable for the single-mode fibres and lens configuration used in the hardware. The intensity of the beam is thus represented by a Gaussian distribution with a source power P_s, and focused spot size a_0 located at a depth f

$$A(z,x) = \frac{P_s \exp\left[-x^2/a^2(z)\right]}{\pi a^2(z)} \tag{B.4}$$

where,

$$a^2(z) = a_0^2 + \left[\frac{(z-f)\lambda}{2\pi n a_0}\right]^2$$

Finally, this leads to a normalised expression for the OCT image signal $I(z)$ (where in practical terms, the coefficient of absorption μ_a may be disregarded):

$$\begin{aligned} I(z) &= Bp_b(z)\mu_s(z)\exp\left\{-2\int_0^z\left[\mu_s(z') + \mu_a(z')\right]dz'\right\} \qquad \text{(B.5)} \\ &\times\left(\int_0^{\infty}\exp\left\{-\frac{a^2(z)h^2}{2} + 2\int_0^z \mu_s(z')\left[1 - 2p_b(z')\right]\tilde{x_1}\left[z', h(z-z')\right]dz'\right\}hdh - \frac{1}{2a^2(z)}\right) \end{aligned}$$

Turchin defines the small angle scatter function $x_1(z,\lambda)$ as a Gaussian, incorporating the phase variance $\langle\lambda^2\rangle$. By applying this model to the general scattering phase funciton, he derives terms for p_b and $\langle\lambda^2\rangle$ based on Mie calculations:

$$p_b = \frac{x_{Mie}(\pi)}{2} \qquad , \tag{B.6}$$

$$\left\langle \lambda^2 \right\rangle = \frac{1}{2(1-2p_b)} \int_0^\infty \lambda^3 \left[x_{Mie}(\lambda) - 2p_b\right] d_\lambda \tag{B.7}$$

Equation B.5 has the potential to more accurately reflect the observed OCT signal recorded from the bilayer phantoms described in Chapter 2. Specifically, the step change in signal intensity at the layer boundary is better addressed by the RTE model. It takes account of light interactions, such as scattering phase function and probability of backscatter, which vary at the layer boundary and are not present in the simple exponential attenuation model set out in Chapter 3.

Appendix C

Correlation Function Peak Interpolation in NCC Tracking – Jitter Formation

Experimental results from Chapters 3 and 4 indicate the presence of imaging artefacts in displacement and strain maps. This appendix is a summary of work carried out to locate experimentally the formation of these artefacts. For normalised cross-correlation (NCC), displacement is estimated by measuring the position of the correlation functions peak value. In autocorrelation, the peak position – its lag – is always zero. However, the correlation function's shape changes according to the OCT image data covered by the reference window, so that it may not necessarily be symmetric either side of the peak (figure C.1). The artefact, known as jitter, arises in this instance when interpolation of the correlation function's peak leads to its position being recorded as non-zero. The lag dictates the displacement value recorded for that reference window and asymmetry in the interpolated peak can lead to deviations in the final displacement estimate from its actual value. For an autocorrelated image, the interpolated peak's asymmetry will lead to variations in displacement estimates around zero.

The interpolation process consists of isolating the correlation function's maximum and the two values either side of this peak. These are then interpolated using a second order polynomial (which was found adequate, whilst being computationally more efficient than applying a Gaussian or spline fitting function). Once interpolated, the new maximum is located and its position recorded. This new position is the lag, which is used as an estimation of displacement. For the autocorrelation example illustrated in figure C.1 the interpolated peak lag displays jitter, moving between values on either side of the zero lag point. This can be seen in figure C.2. In an attempt to reduce the jitter artefact, a moving average filter was applied either to the OCT image data or to the correlation function before interpolation (figure C.3). This smoothing was intended to produce a smaller offset in the correlation function's peak lag. However, filtering exacerbated the artefact, especially when applied to the correlation function. As a result, no image processing is used prior to or during NCC to remove jitter.

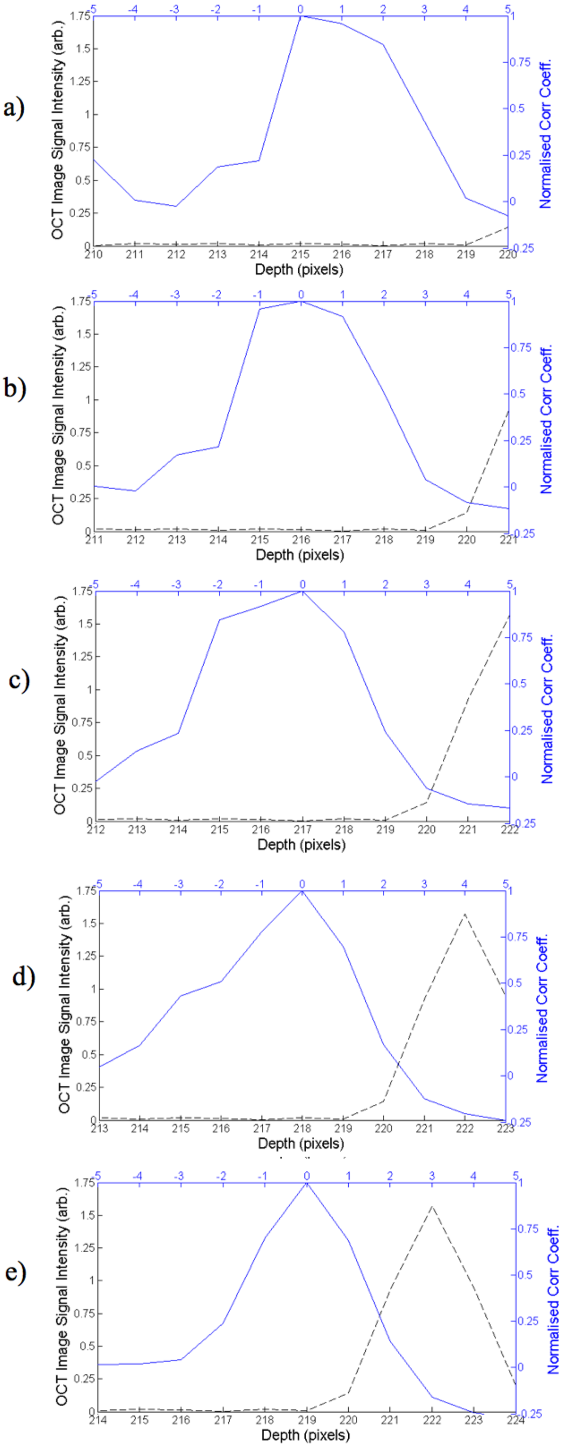

Figure C.1: Data within a reference window as it sweeps a) to e) over a peak in the OCT A-line signal (dotted line), and the corresponding autocorrelation function (blue line with lag indicated along upper x-axis). Despite the function's asymmetry, its peak lag is always zero.

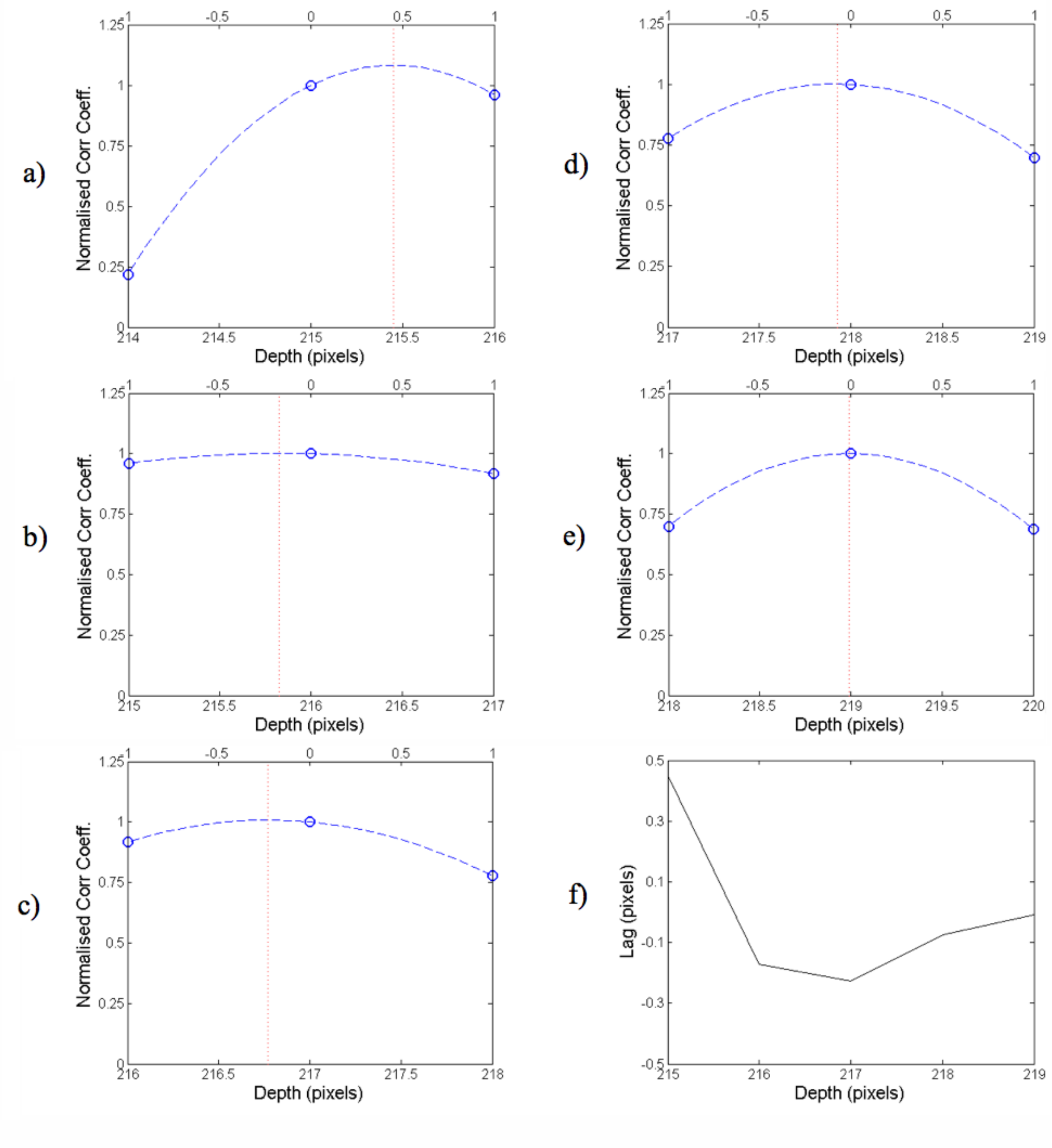

Figure C.2: a)-e) Peaks of the correlation functions from figure C.1a)-e) interpolated via 2nd order polynomial. The upper x-axis is lag. Peak lags from a)-e) are plotted against reference window position in f).

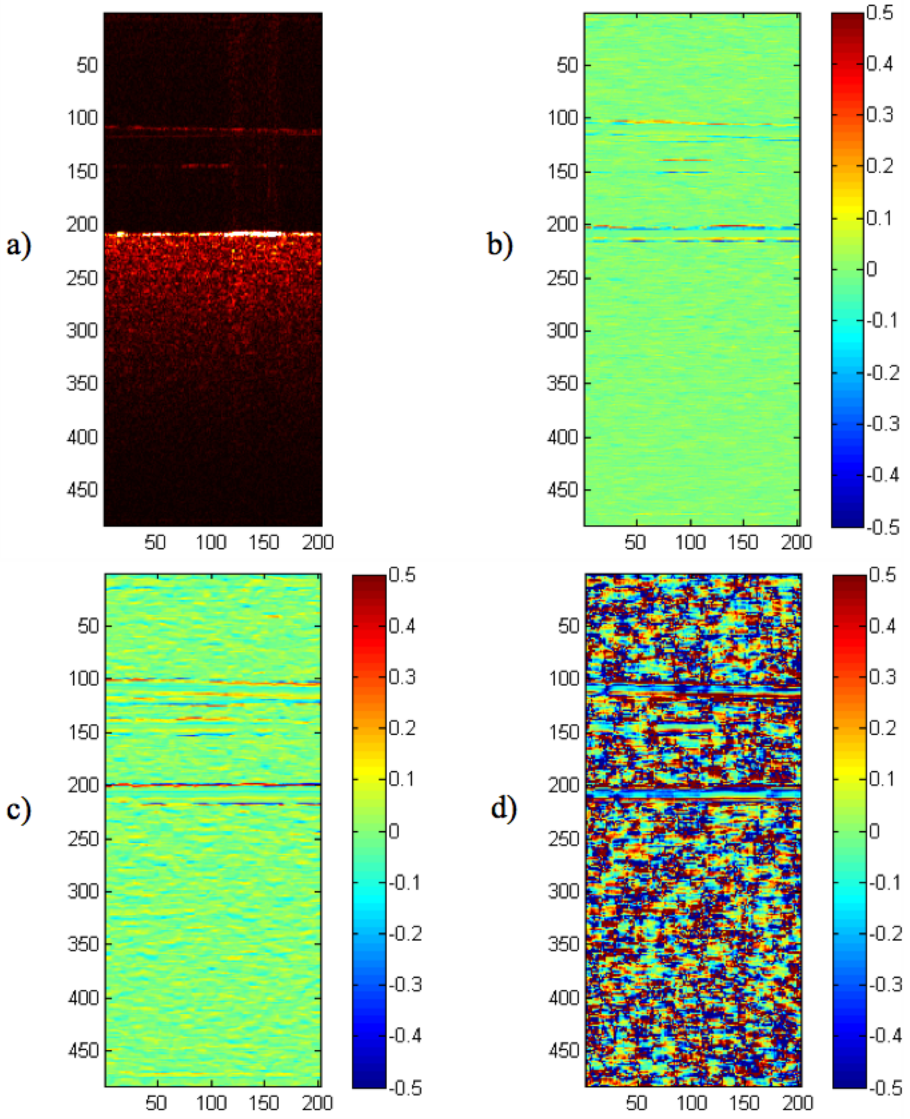

Figure C.3: A standard OCT image a) and its autocorrelated displacement map b). A smoothing filter applied to the OCT data produces more pronounced artefacts c). Applying the filter to the correlation function generates even greater distortions d). Colour scale is in pixels.

Appendix D

Incremental and Multi-Resolution Tracking in Tissue

Methods to reduce the high rates of decorrelation associated with performing NCC tracking on tissue were investigated and adopted. Two basic techniques were combined, these techniques were incremental tracking and multi-resolution tracking (both previously described in Chapter 3.). Incremental tracking had previously been avoided because it amplified jitter artefacts in the final data. However, the approach combines estimations taken over smaller displacements and is thus useful for reducing decorrelation. As such, it was adopted. The multi-resolution tracking technique is performed to mitigate artefacts in noisy data, hence its adoption here. This technique is a quality-guided approach because it relies on the calculation of a weighted mean between a pixel's displacement value and its correlation coefficient. So the final data is influence more by displacement values with strong correlation. However, for a region where correlation coefficients are generally low, or where there is a high but incorrect correlation, the weighted average will be of little use. Figure D.1 is an illustration of the processing steps involved. It is immediately obvious that this combined technique relies on multiple correlations where only a single correlation would be performed in standard NCC. As such, it is computationally expensive by comparison. For example, the incremental process tracked displacement between 15 pairs of images compared where a standard image tracking run would use only one pair. Additionally for each of these 15 pairs, three correlations were calculated to perform the multi-resolution estimates. Each of these three cycles had different tracking parameters, two of them being non-exhaustive and thus relatively fast to execute. However, in terms of numbers of correlations; for every single correlation performed by standard NCC tracking, the combined technique performs 45. Displacement maps are also displayed to illustrate the gradual improvements imparted to the displacement data (figures D.2 & D.3). Finally, the strain estimates derived from combined method is shown in figure D.4, demonstrating a greater influence on the overall strain field from the axial normal strain component. It cannot be verified if this is an indication of the tissue's internal structure or the result of correlation artefacts.

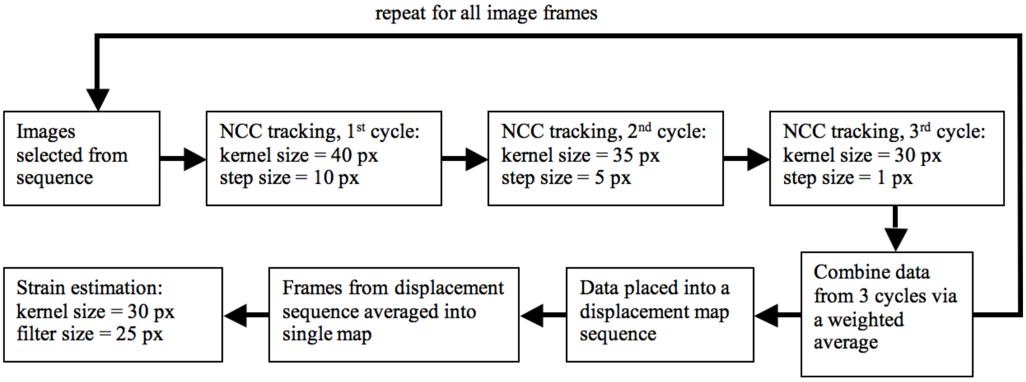

Figure D.1: Procedural schematic outlining processing steps in the combined image tracking technique used in Chapter 4.

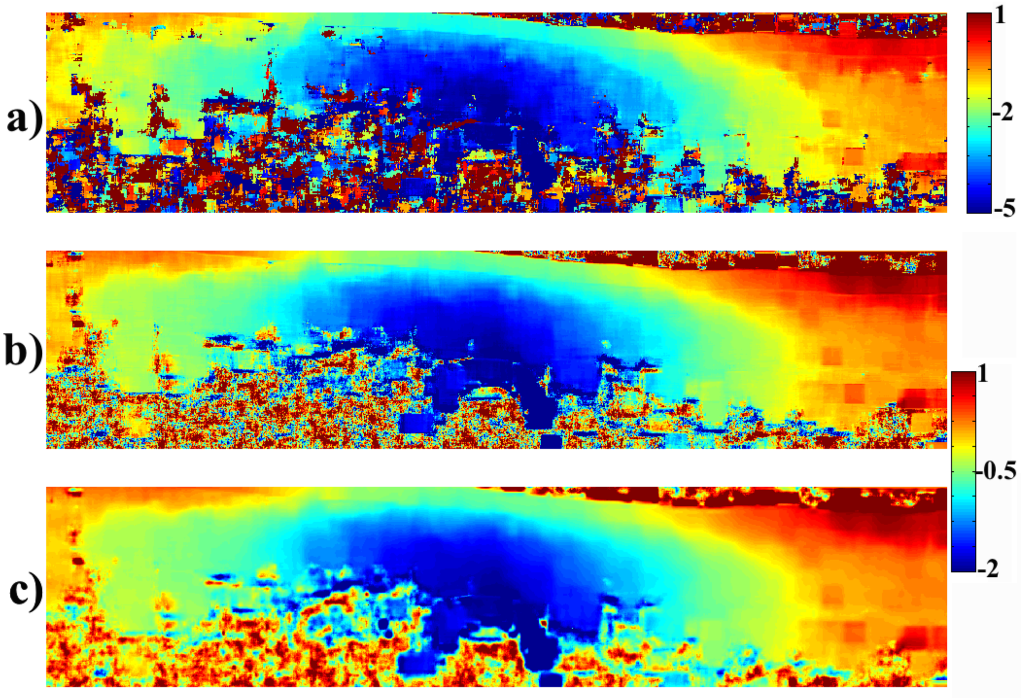

Figure D.2: Axial displacement estimates based on a) a standard NCC between frames 1 and 49 in the chicken breast image sequence (Chapter 4). b) averaged displacement map constructed from incremental approach, where images 15 frames apart are correlated. c) combined approach incorporating multi-resolution and incremental techniques to produce a single displacement map. All scales are in pixels.

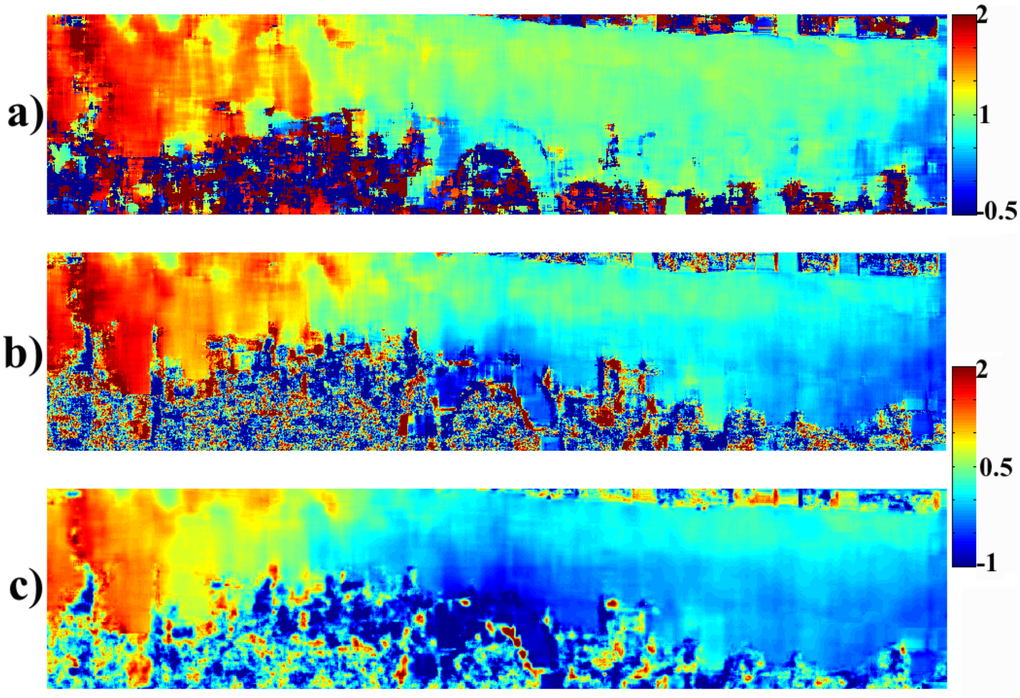

Figure D.3: Lateral displacement estimates based on the same images used to produce axial displacement maps in figure D.2. a) standard NCC between frames 1 and 49. b) incremental approach and c) combined approach. All scales are in pixels.

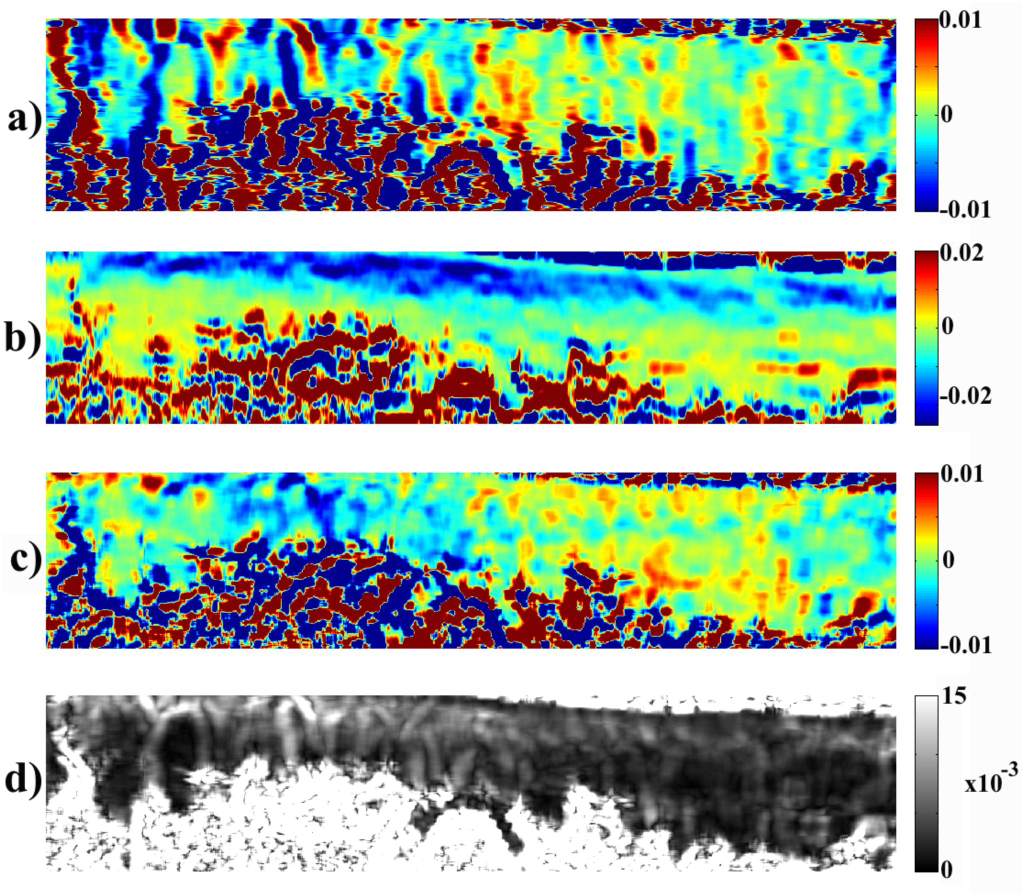

Figure D.4: Strain maps constructed using the combined process. a) lateral normal strain, b) axial normal strain, c) total shear strain. The magnitude of all strain components is shown in d). The scales denote absolute strain.